Surface Deformation in a Liquid Environment Resulting from Single Particle Collisions

Thesis by

Angel Ruiz-Angulo

In Partial Fulfillment of the Requirements
for the Degree of
Doctor of Philosophy

California Institute of Technology
Pasadena, California

2008
(Submitted May 22, 2008)

to my Grandfather, Angel Sagar . . .

Acknowledgements

The opportunity of joining Caltech as a graduate student was unique and I feel really fortunate that I was able to be part of this great institution. As it should be, great institutions have great people and all those wonderful people that directly or indirectly contributed to this work, I would like to thank them.

My appreciation goes to my academic advisor, Prof Melany Hunt whom I thank for her unconditional support and understanding during my stay at Caltech. Under her guidance I had the wonderful chance to participate in multiple projects that enriched my formation. Thanks to her I discovered the amazing singing dunes in the California desert. I totally enjoyed every single field trip to the dunes. I would also like to thank Prof Christopher E. Brennen not only for his guidance but also for encouraging me to enjoy the wonderful outdoor opportunities in California, thanks a lot for the Eaton Canyon rappel experience.

I am also grateful to the members of my committee: Professor Guruswami Ravichandran, who always had a smile to share with me and will always cheer me up to finish my studies, Professor Chiara Daraio, who provided me with some extra energy at the end of my experimental work, if it was not for her I would have not been able to finish that last experiment, and Professor Tim Colonius, from whom I learned that CFD is a very fascinating but complicated world. To all of them, thanks for reviewing my Ph.D. dissertation.

I am thankful to the California Institute of Technology, the National Science Foundation, and the Petroleum Research Fund for their support during my graduate studies.

This work would have not been possible with the help of many other graduate students and Professors that allowed me to use their facilities. On the MEMS division, thanks to Professor Yu-Chong Tai for letting me use the optical profilometer located in the clean room, thanks as well to Quoc (Brandon) Quach, who provided me with the necessary training to use this facility. In the Materials Science department, I would like to acknowledge Professor Robert Dale Conner and the members of his group Joseph Schramm and Mary Laura Lind,

all those shinny surfaces came from their facilities. Slightly far from Caltech, México, but never to far from me, I would like to thank my former advisor Dr. Roberto Zenit Camacho, his friendship and guidance have been always very much appreciated, gracias Roberto.

During the years I spent in the granular flows group I interacted with graduate, undergraduate, visiting, and high school students, to all of them, thanks for the great opportunity of learning something from you. Specially, I would like to thank Gustavo Joseph for teaching me the basics in the laboratory, Fu-Ling Yang, who shared post cards and papers with me, and Erin Koos for listening to all my complains and helping me with my terrible English. Among all the wonderful people at Caltech, I found a great group of friends; they were dinner partners, drinking buddies, teammates, and, in some sense, family. Thank you Alan, Guillaume, Hannes, Javier, Lisa, Stephane. Thanks as well to my lunch buddies, Chris and Lydia. Also, thanks to Vala for her enormous support and for always being there. I would also like to thank all my biking buddies, all that stress relieved going up, up, up! Thanks to Iván, Daniel, Manuel, Raviv, and Waheb for coming along on those crazy bike rides.

In México, I would also like to thank all my friends that supported me during this period of my life; thanks to Nacho, Carlos, Daniel, Fabiola, Lina, and Paty, I really enjoyed having you around me all the times I visited home. I would like to thank as well my friends from my undergraduate days at UNAM, they were always there to hear how hard Caltech was, thanks to Carlos, Diego, Hazel, Joel, and Víctor. Believe me that all of you made this path a lot smoother than what it appeared, mil gracias!

At last, but never the least, I would like to thank my family, María del Pilar, Alfonso, Pili, and Andrea, your love and support provided me with the strength necessary to always do a little more than what I thought I could do. I am really fortunate for having all of you, gracias bellísima familia.

Abstract

Multiphase flows are fairly complex and they are usually studied as a bulk. In this thesis, these flows are approached by looking at single particle interactions (particle-particle and particle-wall). This work presents experimental measurements of the approach and rebound of a particle colliding with a "deformable" surface in a viscous liquid. The complex interaction between the fluid and the solid phases is coupled through the dynamics of the flow as well as the deformation process. A simple pendulum experiment was used to produced single controlled collisions; steel particles were used to impact different aluminum alloy samples ($Al - 6061$, $Al - 2024$, and $Al - 7075$) using different aqueous mixtures of glycerol and water as a viscous fluid. The velocity of the particle before and after the collision was estimated by post-processing the particle position recorded with a high speed camera. For the combination of materials proposed, the elastic limit is reached at relatively low velocities. The deformations produced by the collision were analyzed using an optical profilometer. The measurements showed that the size of the indentations is independent of the fluid media. It was found that the size of the indentations was the same for collisions in air than for the rest of the collisions using various viscous fluids. The results show that the plastic deformation is only a function of the impact velocity and the material properties. The normal coefficient of restitution and deformation parameters account for losses due to lubrication effect and inelasticity, identifying then, the dominant energy loss mechanism during the collision process.

According to the strain imposed in the samples due to the collision, the deformations were either elastic or elastic-plastic. The equivalent load due to the impact velocities used in this work did not reach the fully-plastic regime. For the collisions in air, different models were used to compare the experimental results showing that the elastic-plastic regime is not well characterized by only the material properties and the impact velocity. The time-resolved contact force was measured during the process of the indentation for the dry collision experiments using a quartz load transducer.

The experiments clearly show four different regimes depending on the impact Stokes number: lubrication effect and elastic deformation, lubrication effect and elastic-plastic deformation, elastic deformation with no hydrodynamic effects, and elastic-plastic deformation with negligible lubrication effect. An analysis of the erosion of ductile materials during immersed collisions is presented. The size of the crater formed by the impact of a single particle against a ductile target can be estimated from theory, and these estimates agree well with experimental measurements.

Contents

List of Figures

List of Tables

Chapter 1

Introduction

1.1 Motivation

Multiphase flow is defined as any fluid flow consisting of more than one phase. For this thesis, the varied spectrum composed of many possible applications has been limited to liquid-solid systems. Moreover, only systems where the solid phase is suspended in the liquid will be considered.

The interest in fluid-particle flows, a subset of multi-phase flow, arises from many industrial applications and natural processes, such as: coal slurry pipelines, fluidized beds, mining, fossil-oil extraction, pneumatic transportation, filtering (Crowe et al. (1998), Eames and Dalziel (2000), Ruff and Bayer (1993)), abrasive jet machining, polishing, and surface abrasions. In many cases, the dynamics of these processes is affected by the collisions between particles and the particle-wall interactions. Those interactions, specifically particle-wall interactions, may carry enough energy to cause deformation or erosion of the solid surfaces. Erosion processes are not just limited to industrial applications; in nature, debris flows, landslides, and sediment transportation are common examples of flows carrying a substantial amount of solids (Iverson (1997)).

In past years, many efforts have been made to study erosion by researchers such as Finnie (1960), Goldsmith (1960) and Bitter (1963). They developed analytical models to predict the rate of wear as a function of the material properties and the velocity of the idealized particles. However, those studies neglected the fluid phase.

The transport of solid-liquid slurries via pipelines can cause considerable damage to the pipe-walls and pump components (Zhong and Minemura (1996), Edwards et al. (2001), Kadambi et al. (2004)). Wear and corrosion in the pumps make them the most vulnerable component of the slurry pipeline system, reducing the reliability and operation life of the equipment.

Laboratory investigation of slurry erosion, where the surrounding fluid is considerable, has been completed by Clark (1991). Typically, slurry erosion experiments concentrate only on the bulk wear rates for different flow conditions and particle sizes. The erosion rate is then estimated based on the kinetic energy of the particles. However, despite extensive studies, the conditions and mechanisms of material loss in slurry erosion remain undefined (Ruff and Bayer (1993)). Modeling slurry erosion requires a better understanding of this complex problem, which couples the mechanics of the flow with the deformation process.

1.2 Particle-wall interaction

Particle-wall interactions can be divided into two categories depending on whether the surrounding fluid affects the particle motion or not. When the particle inertia is large enough, such that the hydrodynamic relaxation time is small compared to the collision duration, the surrounding fluid may be neglected. Otherwise, those forces will affect the particle motion and, in an extreme case, might prevent the particle from real contact with the wall. Particle-wall collisions can be characterized by the Stokes number, which is the ratio of the particle inertia to particle viscous drag, given by

$$St = \frac{2mU}{3\mu\pi d_p^2} = \frac{\rho_p U d_p}{9\mu}, \tag{1.1}$$

where m is the mass of the particle, d_p is the particle diameter, μ is the dynamic fluid viscosity, U is the particle velocity, and ρ_p is the density of the particle.

The elastic bouncing of a solid particle with a thick wall can be characterized by the coefficient of restitution e, which is defined as the ratio of the rebound velocity, U_r, to the impact velocity, U_i, just after and before the collision. The expression for e is given by

$$e = -\frac{U_r}{U_i} \quad . \tag{1.2}$$

During the collision, the initial kinetic energy is transformed into elastic strain energy stored in the bodies and then restored back into kinetic energy. Under conditions of negligible fluid resistance, $e \approx 1$, only a small amount of energy is being absorbed as elastic waves (see Section 1.4). The coefficient of restitution characterizes the energy losses during collision in the most general point of view. Several experiments exploring the parameters affecting the coefficient of restitution have been done. Raman (1920), Zener (1941), Hutchings (1979), and Reed (1985) studied the intrinsic inelasticity of particles colliding with plates of different thickness. They found that the energy lost by the sphere during the impact was equal to the energy absorbed by the plate, resulting on a decrease on the coefficient of restitution. Later studies, Sondergaard et al. (1990), showed that not only the energy absorbed as elastic waves result on energy losses. During the collision, the reflections of those waves from the end of the plate produce surface vibrations, which might contribute significantly to the reduction on the coefficient of restitution.

If the impact velocity exceeds the elastic limits, plastic deformation occurs, consuming some energy and causing permanent indentation, Johnson (1985). Hutchings (1981), Kharaz and Gorham (2000), and Yang and Komvopoulos (2005), carried out experiments of normal collisions involving plastic deformation. The coefficient of restitution decreased due to the energy dissipated in plastic deformation. However, the coefficient of restitution may also decrease if the energy is dissipated by other means. All of the above studies assume that the interstitial fluid was negligible. When the dynamics of the fluid has significant effect, before, during, and after the collision, the coefficient of restitution is affected. For a perfectly rigid sphere moving into a viscous fluid, the kinetic energy prior to impact is dissipated by viscous forces as it approaches the wall. Those collisions in a stationary liquid were first studied by McLaughlin (1968), finding that the recovery of momentum or effective coefficient of restitution, is a function of the particle impact Reynolds number. Later studies, Zenit and Hunt (1999), Joseph et al. (2001), and Gondret et al. (2002) confirmed the previous results obtained by McLaughlin (1968), showing the dependence of the effective coefficient of restitution on the particle Stokes number. Expanding the horizons of liquid-solid impacts resulted in “elastohydrodynamics” theory, Davis et al. (1986), Barnocky and Davis (1988), Lian et al. (1995). In those studies the deformations are assumed to be elastic, the particles deform elastically due to the increase in the hydrodynamic pressure in the lubricating fluid between the particles. The results show that the particle deformation and particle rebound depend on the Stokes number and the elasticity parameter (See Section 1.5.2). In the literature there are no references of immersed single particle collisions beyond the elastic limit. Most analyses of slurry or suspension flows involve the extension of the deformation equations from dry collisions to a liquid environment (Shook and Rocco (1991), Clark (1991, 1995) and, Zhong and Minemura (1996)). The results from those studies are often used to determine the overall correlation between wear rates and flow conditions.

1.3 Dry collisions

When the surrounding fluid is neglected, the collisions can be sorted, according to the severity of the impact, in three main groups: elastic, elastic-plastic, and plastic collisions. The following section provides a detailed analysis on the elastic and elastic-plastic regime.

1.3.1 Elastic collisions

Elastic collisions have been extensively studied. Hertz developed the widely accepted theory of elastic collisions, which assumes quasi-static behavior. The deformation is fully determined by the instantaneous stress distribution. The elastic oscillations (elastic wave motion in the bodies) are neglected (see Section 1.4).

Figure 1.1 shows two smooth, frictionless, non-conforming elastic spheres brought into contact. As the compressed force in the normal direction P increases, the region of contact spreads to radius r_e. The expressions for the elastic contact of a sphere with a half-space are found by taking the limit as one of the radii becomes very large. Therefore, the contact radius for the elastic contact for a sphere with a half-space is:

$$r_e = \left(\frac{3RP}{4E^*} \right)^{1/3}, \tag{1.3}$$

where P is the total load compressing the solids, R is the particle radius, and E^* is the reduced elastic modulus given by

$$E^* = \left[\frac{1-\nu_1^2}{E_1} + \frac{1-\nu_2^2}{E_2} \right]^{-1}, \tag{1.4}$$

where E_1, E_2 are the elastic Young's moduli of the two solids in contact and ν_1, ν_2 are the corresponding Poisson's ratios. Similarly, the displacement on the normal direction, δ_e, due

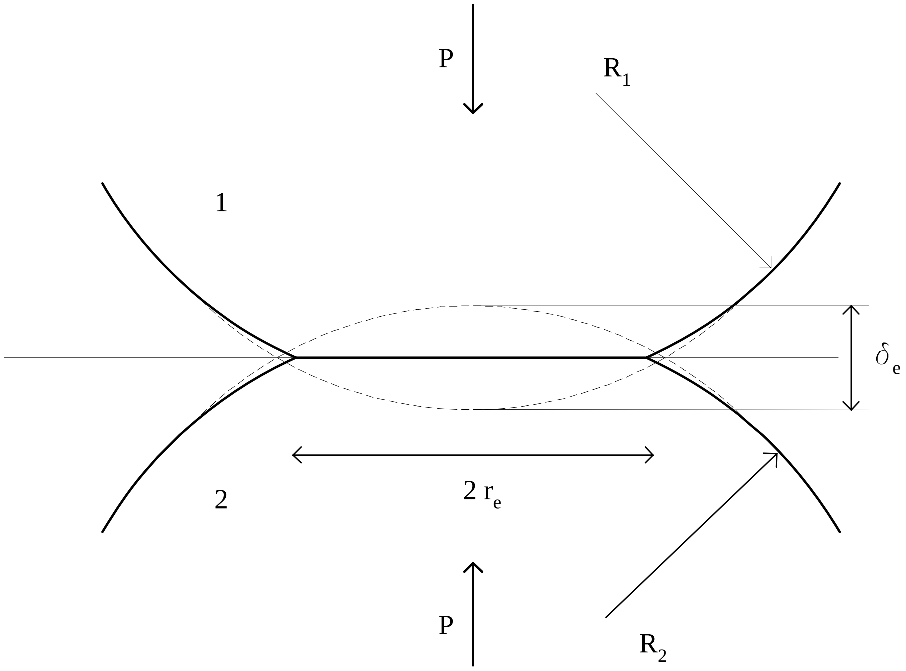

Figure 1.1: Schematic representation of the Hertzian contact

to the compressing load is given by

$$\delta_e = \left(\frac{9P^2}{16RE^{*2}} \right)^{1/3}. \tag{1.5}$$

The contact pressure, resulting from the compressing load, P, acting over the contact area, generates local elastic deformations and surface displacements that cause the initially nonconforming surfaces to conform within the contact area (see Figure 3.9). Within the contact area, the pressure distribution proposed by Hertz is:

$$p(r) = p_0 \left(1 - \frac{r^2}{r_e^2} \right)^{1/2}, \qquad r \leq r_e \tag{1.6}$$

where r is the radial coordinate at the contact point and $p_0 = p(r = 0)$ denotes the pressure at the center of the contact area. Integrating the pressure distribution over the contact area yields the compression load

$$P = \int_0^{r_e} p(r) 2\pi r dr = \frac{2\pi}{3}\, p_0\, r_e^2. \tag{1.7}$$

During the impact, the elastic deformation produces a displacement normal to the contact surfaces denoted as δ_z. In order to include the dynamics required for real collisions, let the total mass of the particle move with the velocity of its center of mass, U. The particle impact velocity is given as $d\delta_z/dt \approx U_i$. Hence, the instantaneous force between the bodies is $P(t) = m\, dU_i/dt = m\, d^2\delta_z/dt^2$, where m is the mass of the impacting particle. Combining this expression with Equation 1.5 results in

$$P = m\frac{d^2\delta_z}{dt^2} = \left(\frac{16RE^*\delta_z^3}{9} \right)^{1/2}. \tag{1.8}$$

The equivalent load resulting from an elastic particle-wall collision with impact velocity U_i and final elastic displacement δ_e, can be estimated by integrating Equation 1.8 with respect to δ_z. Using $U(t = 0) = U_i$ as the initial condition of the impact, and at the maximum compression, when the particle finally comes to rest, $d\delta_z/dt = 0$. Finally, rewriting the equation in terms of the particle density, ρ_p, and combining with Equation 1.5

results in the elastic compressive force acting between the bodies during impact:

$$P = \frac{4}{3}\left(\frac{5\pi}{4}\right)^{3/5} R^2 E^* \left(\frac{\rho_p U_i^2}{E^*}\right)^{3/5} . \tag{1.9}$$

The period of a elastic collision under these conditions is given by (Johnson (1985)):

$$\tau_e = 2.87 \left(\frac{16\pi^2}{9} \frac{\rho_p^2 R^5}{E^{*2} U_i}\right)^{1/5} . \tag{1.10}$$

With the aid of Equation 1.9, Equations 1.3 and 1.5 can be now expressed in terms of the impact velocity. This convenient substitution is used in the following sections.

1.3.2 Elastic-plastic collisions

The previous section (section 1.3.1) discussed the elastic theory proposed by Hertz. This section provides the combination of elastic Hertzian theory with small plastic deformations. This combination of effects is known as elastic-plastic contact. Consider a rigid particle that only deforms plastically impinging on a flat softer body that can undergo plastic deformation. Yield begins directly below the contact surface, and the material with the lowest yield strength, Y (in this case the wall) deforms first. The yield point of most ductile materials is described by two different criteria: the von Mises shear-strain energy criterion and Tresca's maximum shear stress criterion. In both cases, the maximum shear stress occurs beneath the surface on the axis of symmetry. Along this axis σ_z, σ_r, and σ_θ are principal stresses, and due to axi-symmetry $\sigma_r = \sigma_\theta$. For the materials presented in this thesis (see Table 2.1), the maximum value of $|\sigma_z - \sigma_r|$, for $\nu = 0.33$, is $0.61 p_0$ at $z/R = 0.49$, where z is the coordinate normal to the contact surfaces. The value of p_0 is given by the von Mises criterion as

$$p_0 = 2.86k = 1.65Y, \quad \text{where} \;\; k = \frac{Y}{\sqrt{3}}.$$

Correspondingly, by Tresca's criterion, p_0 becomes

$$p_0 = 3.30k = 1.65Y, \quad \text{where} \;\; k = \frac{Y}{2}.$$

The load required to initiate yield, P^*_{el}, can be related to the maximum contact pressure through a combination of Equations 1.3 and 1.7 with the previous value of p_0 for yield

$$P^*_{el} = \frac{\pi^3 R^2}{6E^{*2}}(1.65Y)^3. \tag{1.11}$$

Substituting the critical of P^*_{el} in Equation 1.9 gives an expression for the *elastic velocity*, U_{el}, the velocity necessary for yield to commence. The elastic velocity is

$$U_{el} = \frac{\pi^2}{2E^{*2}\sqrt{10\ \rho_p}}\sigma_{el}^{5/2}, \tag{1.12}$$

where $\sigma_{el} = 1.65Y$ is the stress at the limit of elasticity.

The elastic velocities for the materials used in this thesis are tabulated in Table 5.1. The velocity at which the particle (stainless steel) reaches the maximum limit of elasticity is much larger than the maximum particle impact velocity used during the experiments. Therefore, the assumption of a rigid particle impacting on a elastic-plastic half-space remains valid throughout the rest of the calculations. Following the analysis carried out by Bitter (1963), where a spherical particle impacts a half-space, the colliding sphere deforms only elastically and the flat body deforms both elastically and plastically. For any given normal collision, elastic deformation continues until δ_e reaches its maximum (when $U_i = U_{el}$), during which the Hertzian equations can be used. Combining Equations 1.5 and 1.9, the maximum elastic penetration, δ^*_e, becomes

$$\frac{\delta^*_e}{R} = \left(\frac{5\pi}{4}\ \frac{\rho_p U^2_{el}}{E^*}\right)^{2/5}. \tag{1.13}$$

Similarly, combining Equations 1.3 and 1.9 the maximum elastic radius, r^*_e, is given by

$$\frac{r^*_e}{R} = \left(\frac{5\pi}{4}\ \frac{\rho_p U^2_{el}}{E^*}\right)^{1/5}. \tag{1.14}$$

After U_{el} is reached, plastic deformation begins and increases as a function of the impact velocity. Bitter (1963) assumed that the total contact area is given by the superposition of the maximum elastic contact area and the area of plastic deformation. Additionally, both areas have the same radius of curvature, R, given by the radius of the sphere. The remaining indentation in the flat body after collision has the same radius of curvature as well. Moreover, by assuming that $\delta_{total} < R$, the total contact radius can be simplified to

$r_{total}^2 \approx 2R\ \delta_{total}$. Hence, the total contact area normal to the surface becomes

$$A_{total} = \pi r_{total}^2 = 2\pi R\ \delta_{total} = 2\pi R\left(\delta_e^* + \delta_p\right). \tag{1.15}$$

The area loaded only elastically is:

$$A_e = \pi r_{total}^2 - \pi r_p^2 = 2\pi R\left(\delta_e^* + \delta_p\right) - 2\pi R\ \delta_p = 2\pi R \delta_e^* = \pi r_e^{*2}. \tag{1.16}$$

For the elastic-plastic impact, the size of the contact area deformed elastically is independent of the size of the indentation formed. The energy absorbed during the elastic deformation, Q_e, is given by

$$Q_e = \frac{1}{2} m U_{el}^2 = \frac{2\pi}{3} R^3 \rho_p U_{el}^2. \tag{1.17}$$

The potential energy of the elastic deformation[1] in the area subjected to a elastic-plastic load, Q_{pe} is given by

$$Q_{pe} = \frac{1}{2} \delta_e^* \sigma_{el} \pi r_p^2. \tag{1.18}$$

The total elastic energy stored in the particle and the deformed wall is

$$Q_e + Q_{pe} = \frac{2\pi}{3} R^3 \rho_p U_{el}^2 + \frac{1}{2} \delta_e^* \sigma_{el} \pi r_p^2. \tag{1.19}$$

The formation of the permanent indentation requires an amount of energy equal to:

$$Q_p = \int_0^H \pi r_p^2 \sigma_{el} dH' \approx \pi R H^2 \sigma_e l, \tag{1.20}$$

where H is the depth of the indentation after collision.

The energy balance for an elastic particle approaching an elastic-plastic wall with a velocity U_i can be obtained by balancing the initial kinetic energy of the particle with Equations 1.17, 1.18, and 1.20

$$\frac{1}{2} m U_i^2 = \frac{2\pi}{3} R^3 \rho_p U_i^2 = Q_e + Q_{pe} + Q_p = Q. \tag{1.21}$$

---

[1] By definition, the potential energy of deformation of a body, which is in equilibrium under a given load, is equal to half of the work done by the external forces acting through the displacements from the unstressed state to the state of equilibrium.

Since the radius of curvature of the deformation is conformal with the particle radius and $H << R$, $r_{pmax} = 2R\ H$, therefore

$$Q_{pe} = \frac{1}{2}\delta_e^*\sigma_{el}\pi r_p^2 \approx \delta_e^*\sigma_{el}\pi RH = \sqrt{\pi\sigma_{el}R\ \delta_e^2}\sqrt{\pi\sigma_{el}\ RH^2} = \sqrt{\frac{15}{4}Q_e\ Q_{pe}}. \tag{1.22}$$

Combining Equations 1.22 and 1.21 results in

$$Q = Q_e + \sqrt{\frac{15}{4}Q_e\ Q_{pe}} + Q_p = \left(\sqrt{Q_e} + \sqrt{Q_p}\ \right)^2 + A\sqrt{Q_e\ Q_p}, \tag{1.23}$$

where the constant $A = (\sqrt{15} - 4)/2$. The exact solution for the final indentation depth, H, as a function of the impact velocity, U_i, is given by

$$H = \frac{1}{2}\left(\sqrt{\delta_e^{*2} + \frac{8R^2}{3}\frac{\rho_p(U_i^2 - U_{el}^2)}{\sigma_{el}}} - \delta_e^*\right). \tag{1.24}$$

In general, Q_e is smaller than Q_p; therefore, the term $A\sqrt{Q_e\ Q_p}$ in Equation 1.23 can be neglected:

$$Q_p = \left(\sqrt{Q} - \sqrt{Q_e}\right)^2 = \frac{2\pi}{3}R^3\rho_p\ \ (U_i - U_{el})^2 = \pi RH^2\sigma_e l. \tag{1.25}$$

Solving for the indentation depth, H, results in

$$H = \underbrace{\sqrt{\frac{2\rho_p R^2}{3\sigma_{el}}}}_{\tau_B}(U_i - U_{el}), \qquad U_i > U_{el}. \tag{1.26}$$

Equation 1.26 suggests that the permanent indentation depth is proportional to the total characteristic time for an elastic-plastic collision, τ_B, and the particle impact velocity relative to the elastic velocity. Note that for $U_i < U_{el}$, $H = 0$. The analysis carried out by Bitter can be compared with the one proposed by Johnson, where the total time of an elastic-plastic collision consists of: the time of elastic contact, τ_e, given by Equation 1.10, and the plastic deformation period, τ_p. The plastic deformation time is estimated by assuming that the plastic deformation occurs under constant dynamic pressure, p_d, which is in fact, proportional to the yield strength. The expression obtained is independent of the particle impact velocity and it is given by

$$\tau_p = \left(\frac{\pi^2 R^2 \rho_p}{6 p_d} \right)^{1/2}. \tag{1.27}$$

1.4 Wave Propagation

As a result of a sudden load, such as an impact, a material is stressed. The deformations and stresses are transmitted to the remote portions of the body via wave propagation. The impact response can be roughly divided into three regimes, depending on the severity of the load and the dynamic response of the materials. The three wave regimes are: elastic (E), elastic-plastic (EP), and fully plastic or shock (S). This section covers a brief review on the impact response of homogeneous materials only in the elastic regime, and the validation of using a Hopkinson-Kolsky-type bar.

1.4.1 Elastic wave propagation

The compression load resulting from the impact of a spherical particle on a long rod produces a pressure pulse that propagates along the rod. This pressure pulse can be described by the $1D$ stress wave propagation theory in a thin, long rod. The fundamental assumptions of this theory are that the bar is homogeneous and isotropic, uniform in cross section over the entire length of the bar, and for elastic waves to propagate, the stress in the pulse must be below the elastic limit of the bar material (linear-elastic state of stress). Thus, the one dimensional wave equation is described by

$$\frac{\partial^2 u(x,t)}{\partial t^2} = c_0^2 \frac{\partial^2 u(x,t)}{\partial x^2}, \tag{1.28}$$

where u is the longitudinal displacement and c_0 represents the wave speed through the material. Since the material remains in a linear-elastic state of stress, the elastic wave speed is given by

$$c_0 = \sqrt{\frac{E}{\rho}}. \tag{1.29}$$

The stress in the bar, σ_B, produced by the impact of a striker, according to the $1D$ wave propagation theory, is given by (Gama et al. (2004))

$$\sigma_B = \rho_B \; c_0 \; (U_i/2), \tag{1.30}$$

where ρ_B is the density of the bar and U_i is the impact velocity.

1.4.2 Split-Hopkinson-Kolsky-type bar

The experimental work in this thesis uses a Split-Hopkinson-Kolsky type of bar. The following section shows the validation of the bar and the comparison of rigid and deformable materials. As described in the review done by Gama et al., pressure bars are commonly used for measuring the pressure produced by an explosive, following the wave propagating in the bar, and determining the dynamic compression stress-strain behavior of different materials. Typically, a Split-Hopkinson-Kolsky-type bar consists of three elements: the striker bar, the incident bar, and the transmission bar. Figure 1.2 shows a simple representation of the typical experimental setup. The striker bar, often propelled by a gas gun, strikes the incident bar sending a compressive wave into the incident bar. The specimens are placed between the incident and transmission bar. Strain gages are mounted on the incident bar, specimen and transmission bar. Assuming that wave propagation is nondispersive, the force and contact between the bars and specimen can be estimated.

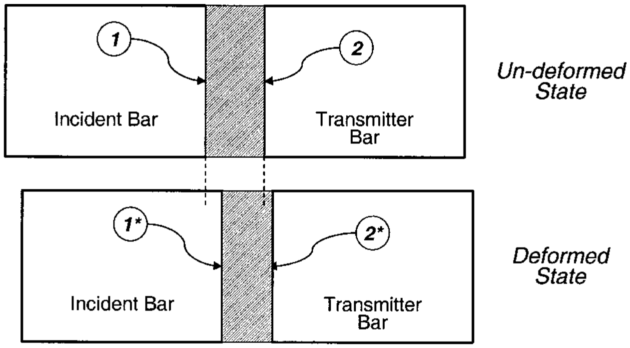

Figure 1.2: Representation of a typical Split-Hopkinson-Kolsky pressure bar; the specimen diameter is equal to that of the incident and transmission bars. The figure was obtained from Gama et al. (2004)

.

The conditions of displacements and stress continuity at these interfaces are assumed to be under perfect contact. The wave reflection at the interface is neglected, and compressive wave propagates through the specimen into the transmission bar as if the system was a single solid bar. Most of those bars have been used for ballistic applications or high-speed impacts (Gama et al. (2004)).

1.5 Fluid pressure and minimum distance of approach

For particle-wall collisions where the viscous effects cannot be neglected, the fluid enclosed between the particle and the wall increases in pressure, p, as the distance between them, δ, decreases. As the pressure in the thin layer increases, not only do the kinematics of the interacting bodies change, the shapes of the bodies may show elastic deformations; the pressure could reach the yield limit, Y, resulting in plastic deformation. This section describes the different regimes that fully immersed particle-wall collisions undergo. The kinematics of the collision are described, followed by the elastohydrodynamic approach, and finally the process including plastic deformation.

1.5.1 Undeformed surfaces, only kinematics

Single collision experiments (Zenit et al. (1997), Zenit and Hunt (1999), Joseph et al. (2001)) have previously reported a variation on the coefficient of restitution due to fluid effects decreasing considerably for Stokes numbers less than 100. A critical Stokes number where no rebound occurs, $St \sim 10$, was found. For Stokes numbers above $St \sim 2000$, the effect of the lubricant layer appeared to be negligible. The experiments were carried out with a brittle wall which did not show any plastic deformation. As shown in Figure 1.3, a fully immersed collision described by a smooth spherical particle with diameter d_p and mass m_p approaches a wall with a velocity $U(t)$, immersed in a Newtonian, viscous, and incompressible fluid with density ρ_f and viscosity μ. Using Newton's second law and assuming that the hydrodynamic forces are dominated by the lubrication forces results in: $F = -3\pi\mu U d_p^2 \ / \ 2\delta = m_p dU \ / \ dt$. The trajectory of the undeformed particle approaching the wall could be written as: $U(t) = -d\delta \ / \ dt$. The combination of the previous equations could be expressed as follows:

$$\frac{d}{d\delta}U = \frac{9\rho_p\mu}{d_p}\frac{1}{\delta}. \tag{1.31}$$

The initial distance at which the particle deceleration begins is defined as δ_{i0}, with a corresponding velocity U_{i0}. Therefore, the solution to Eq. 1.31 becomes:

$$\frac{U}{U_{i0}} = 1 - \frac{ln\left(\frac{\delta_{i0}}{\delta}\right)}{St_{i0}} \tag{1.32}$$

where St_{i0} is the Stokes number based on U_{i0}.

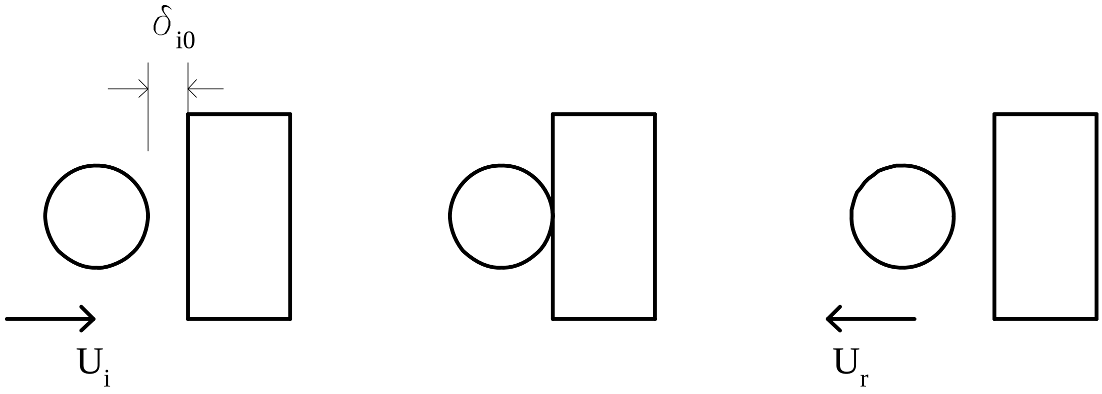

Figure 1.3: Schematic representation of a particle-wall collision, where only deceleration is experienced on the particle, at δ_{i0}, as it approaches the wall. The sequence is followed from left to right.

The critical distance, δ_{i0}, at which the particle decelerates has been topic of discussion by different authors and typically is assumed to be in the order of the surface roughness.

1.5.2 Elastohydrodynamic collisions

The previous section introduced the minimum distance of approach, δ_{i0}, at which the particle decelerates due to the presence of another particle or a plane surface. If the solids are very rigid, only the viscous forces are responsible for the deceleration of the particle as it approaches another object. However, if the solids are less rigid, the hydrodynamic forces upon the nearly touching surfaces can cause the bodies to deform elastically. Davis et al. studied the coupling between the equations of solid mechanics and fluid dynamics. They introduced a dimensionless elastohydrodynamic parameter, ϵ

$$\epsilon = \frac{4\pi\mu U_{i0} R^{3/2}}{E^* \delta_{i0}^{5/2}}; \tag{1.33}$$

this parameter provides a measure of the tendency of the solids to deform elastically. In addition to the elastohydrodynamic parameter, the *minimum approach* distance for a collision involving significant surface deformation was also derived:

$$\delta_m \approx \frac{1}{3}\delta_{i0}\epsilon^{2/5}. \tag{1.34}$$

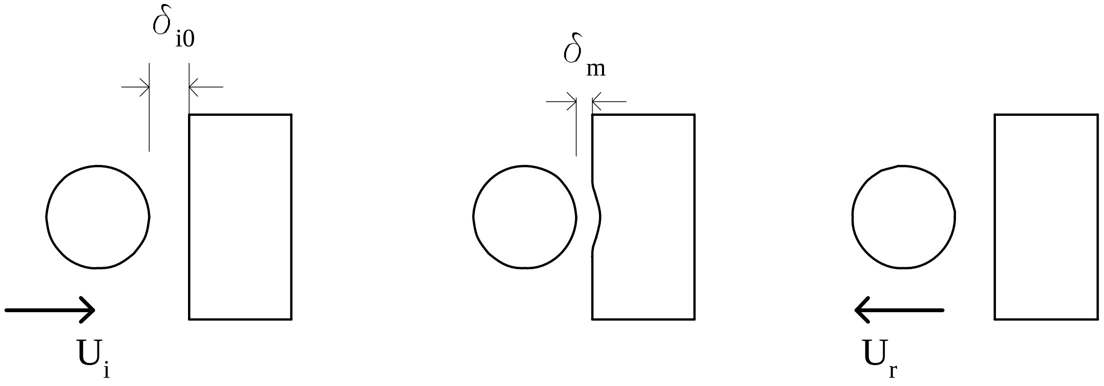

Figure 1.4: Schematic representation for a particle-wall collision with elastohydrodynamic effects. The sequence is followed from left to right.

Davis et al. proposed an asymptotical solution for the critical distance of approach involving significant surface deformation (δ_m). The results of these simulation for various values of ϵ are represented in Figure 1.5, showing the asymptotic value of 1/3 for $St > 10$.

The solution given above is limited in applicability since the minimum approach distance is constant, which is valid for a small range of Stokes numbers.

1.5.3 Elastic-plastic hydrodynamic collisions

As mentioned in the previous section, the hydrodynamic effects can be coupled with the elastic deformation of the interacting bodies. However, if the elastic limit of one of them is exceeded, plastic deformation might occur. Previous work done by Zenit et al. regarding the particle phase pressure resulting from particle-wall collisions, concluded that the pressure

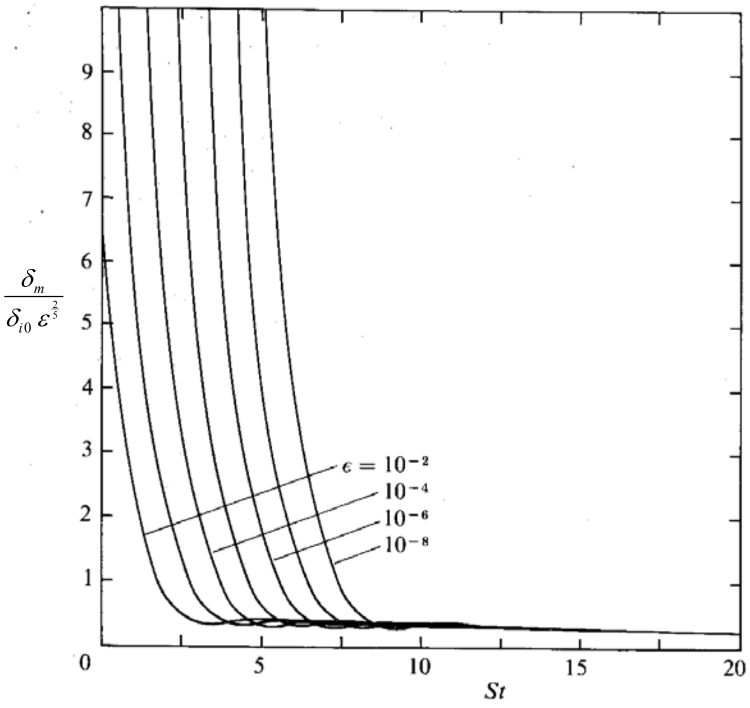

Figure 1.5: Minimum approach distance for a deformed sphere, δ_m, as a function of the particle Stokes number, St, for different values of the elastohydrodynamic parameter. (Figure 13 of Davis et al. (1986))

of the fluid between the particle and the wall has a significant influence on the coefficient of restitution. Similar studies looking for the particle trajectories before collision were conducted by Clark (1992), who also reported the ”squeeze films” influence on erosion. This phenomenon is known as the *cushioning effect*, where a thin layer of liquid resists the close approach of solid surfaces.

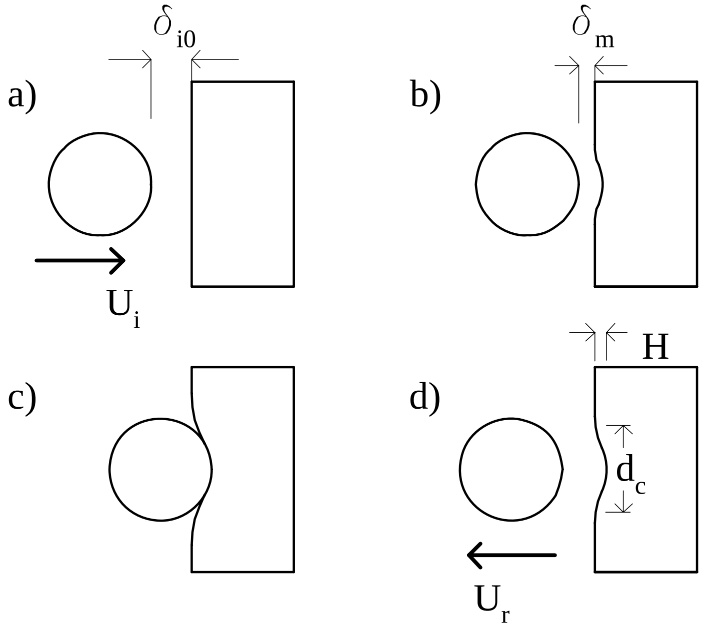

Figure 1.6: Schematic representation of the elastic-plastic hydrodynamic collision. The incoming particle may slow down at a distance δ_{i0} (a). Soon after that, the soft surface experiences significant elastic deformation (b) at δ_m. Finally, contact occurs and the soft material undergoes plastic deformation (c). If the elastic stored energy in the bodies is large enough, the particle bounces off the wall (d) with a velocity U_r.

Significant erosion can be produced by repeated collisions of particles with an eroding body. Hutchings concluded that more than 90% of the initial kinetic energy of a sphere impacting on a soft copper target is consumed in plastic deformation, forming a crater on the surface. Experiments using a slurry pot tester (Figure 1.7) were carried out by Clark (1991, 1995) using suspensions of glass particles with diameters $75-90$, $212-250$, $500-600$ and 750 μm. Several mixtures of water-glycerol were used as test liquids, varying the viscosities from $(0.6-60)\times10^{-3}\ Pa\cdot s$. The nominal rotation speeds of the erosion specimens were 9.35 and 18.7 m/s. The particle impact velocities were calculated based on the nominal rotation speeds.

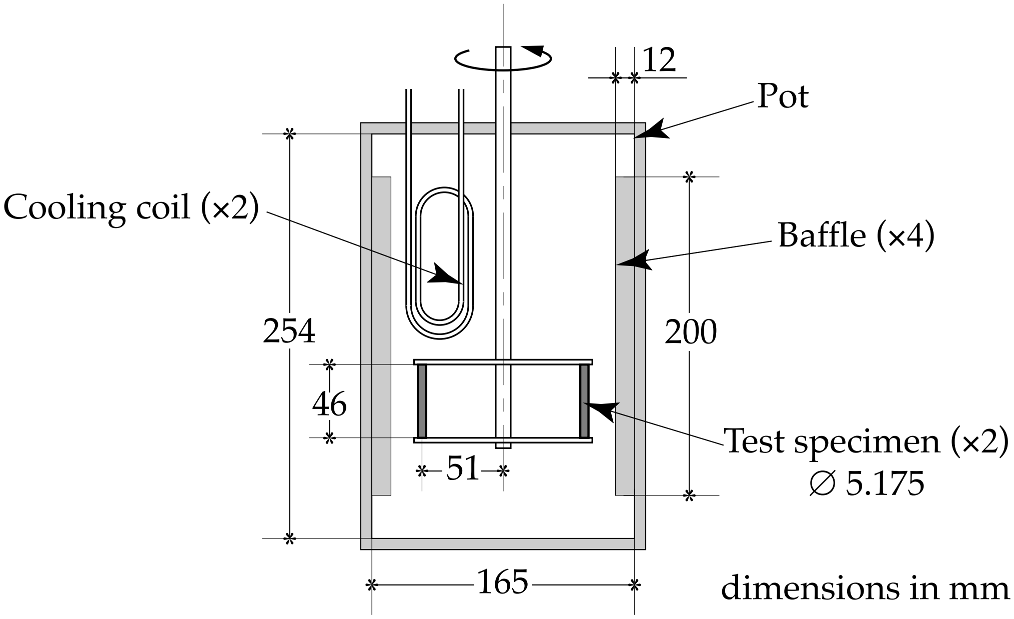

Figure 1.7: Schematic diagram of the slurry pot tester used by Clark (1991)

Previously, Bowden and Tabor (1986) explored the influence of thin layers of viscous liquids (oils) on the formation of permanent indentations resulting from striking particles onto flat surfaces. Bowden and Tabor reported a reduction of the crater size for the impact of a steel sphere on copper when the sphere penetrated a layer of liquid previously placed on the flat surface.The impact velocities used were fairly large ($\sim 9\ m/s$), far from the lubrication regime $St > 2000$. The crater size relative to the particle diameter suggests that the resulting deformations were in the fully plastic regime.

1.6 Thesis outline

This thesis expands on the studies previously completed by Zenit (1997), Joseph (2003) and Yang (2006) on particle-wall interactions. This current work examines the fundamental behavior of collisions of solid particles immersed in various fluids impinging onto surfaces with different elastic properties. In particular, this work focuses on the effects of the surrounding liquid coupled with the plastic deformations of the surfaces due to the impact of the rigid particles. This present chapter presents a literature review and an overview of the possible mechanisms of energy dissipation that could be presented during a single particle-wall collision.

The work presented in this thesis is mainly experimental; Chapter 2 presents the detailed information of the experimental setup used. The experimental techniques required to obtain and process the experimental data are described in Chapter 3.

Chapter 4 analyzes the coefficient of restitution in the elastic-plastic regime, compares the experimental results with three different models, and finally discusses the influence of the surrounding fluids on the coefficient of restitution over the elastic and elastic-plastic regime. The deformation parameters are analyzed in Chapter 5, including a discussion on the influence of the surrounding fluid on the measured parameters. The results are compared with one of the models discussed in Chapter 1.

Chapter 6 discusses the energy of deformation, suggesting that the elastic energy can be decoupled from the plastic energy of deformation. The measurements of the force sensor are reported in Chapter 7.

Lastly, the summary of the experimental results, together with some future directions, are presented in Chapter 8.

Chapter 2

Experimental setup

This section gives a detailed description of the experiment and the data measurement techniques. To measure the consequences of particle-wall collisions under liquid environments, ductile surfaces were struck by rigid particles suspended from a pendulum-like configuration. Different velocities were achieved by varying the release angle of the particles. The experiments were performed in various viscous fluids. The collision process was recorded with a high-speed camera so that, by post-processing the images, the impact and rebound velocities could be estimated. After the collision, the resulting deformed surfaces were measured using an optical profilometer. A new impact surface was used for each experiment.

2.1 Description of the apparatus

As shown in Figure 2.1, the experiment was placed in a clear tank where a rigid structure supported the different components. On the upper part of the frame a fixed bar supports the pendulum-like system. Starting from rest, a single particle was released from the holding mechanism by removing the voltage induced in the electromagnet (discussed in Section 2.1.1). The particle followed a pendular trajectory without rotation. Depending on the releasing angle, ϕ_i, the particle accelerated towards the target reaching different impact velocities. The trajectory of the particles during the complete impact cycle was recorded on a **S-VHS** tape with a high speed camera [1].

Polished samples of different alloys (Table 2.2) were coupled to long rods and placed on a “V”-shape block, as shown in Figure 2.2. The block was fixed to the frame and the rod was finely adjusted for each experiment since small variations on the sample size caused ϕ

---

[1] Redlake *MotionScope* 8000S

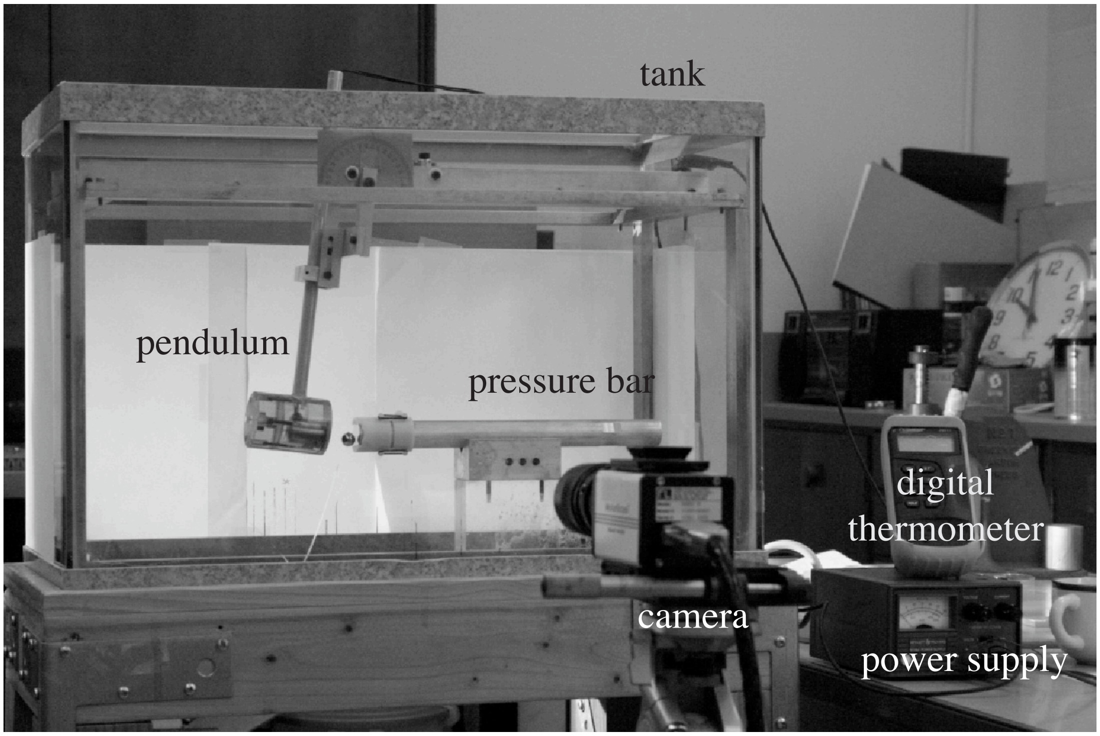

Figure 2.1: Picture of the experimental setup

to deviate from zero. The experiments required normal collisions; therefore, the collision itself corresponds to $\phi = 0$, where ϕ is the angle between the vertical and the string holding the particle.

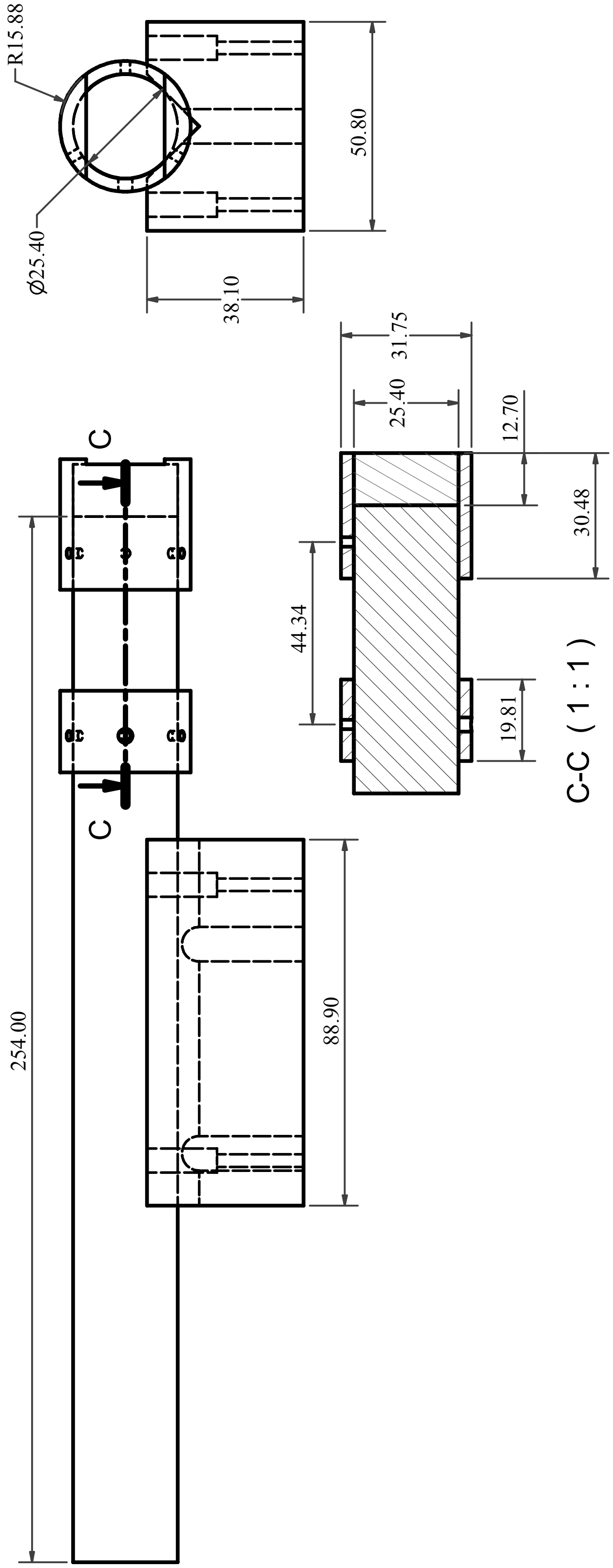

Figure 2.2: Detailed representation of the pressure bar components

2.1.1 Pendulum

A detailed representation of the pendulum release mechanism is shown in Figure 2.3. A fine string was attached to the particle and held by two extremes, forming a "V" configuration, to minimize the rotation of the particle. As mentioned before, the initial release angle ϕ_i changed to achieve different impact velocities. A DC power supply fed the insulated electromagnet that held the particle from a single point. Small magnetic hysteresis on the electromagnet seemed to affect the collision dynamics for small releasing angles, $\phi_i \approx 0$. For releasing angles $\phi_i > 3^o$ no magnetic contributions were noticed.

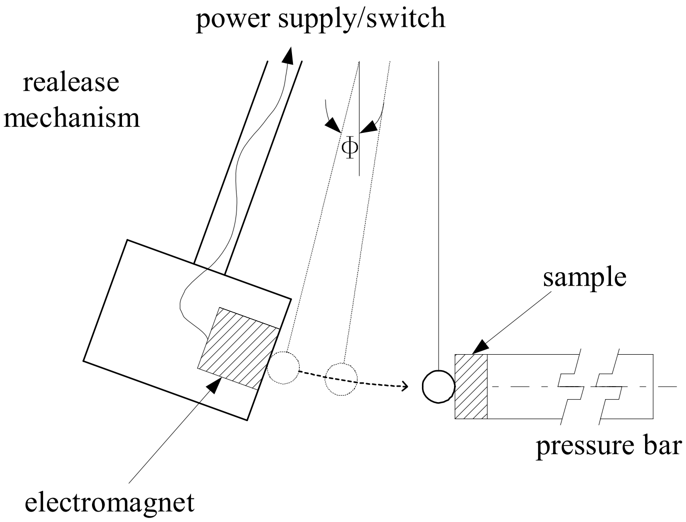

Figure 2.3: Schematic representation of the release mechanism

2.1.2 Particles and impacting surfaces

The physical and mechanical properties of the particles, such as diameter, d_p, sphericity, ϵ, density, ρ_p, Young's modulus, E, and Poisson's ratio, ν, are listed in Table 2.1. Statistical quantities associated with surface roughness, such as root-mean-square surface height [2], σ_s, and the correlation distance, λ_p, are also found in the table.

The impacting bar used was a Split-Hopkinson-Kolsky-type bar, a more detailed explanation can be found in Section 1.4. The dimensions of the bar are 25.4 mm in diameter and 254.0 mm long. The length of the rod, L, was chosen so that the ratio L/d_p was $>> 1$

---

[2] Usually referred to as *roughness*

Table 2.1: Properties of the particles used in the experiments

Material	d$_p$	ϵ	ρ_p	E	ν	Y	σ_s
	(mm)		(kg m^{-3})	(GPa)		(Mpa)	(μm)
Stainless steel	12.7	0.0024	7780	190	0.27	1896	0.0236

(Sondergaard et al. (1990), Hu and Eberhard (2004), Reed (1985)), therefore, the energy losses due to elastic wave reflections were neglected. The samples were 25.4 mm in diameter and 12.7 ± 1 mm thick. For each experiment, the sample and the impacting bar were of the same material to preserve the impedance of the propagating wave constant. The samples were attached to the bar using a plastic holding device (See Figure 2.4). A plastic belt was fixed to the impacting bar. The holding cap housing the "samples" was pulled against the impacting bar by stretching three rubber rings axially distributed connected to the belt. The existing discontinuity between the bar and the sample was neglected and the elastic wave generated from the impact was assumed to travel continuously through the two bodies. As described by Kolsky (Gama et al. (2004)), using a lubricant between the interfaces reduces the friction. For the experiments carried out in this thesis, glycerol-based lubricants were used between the specimen and the transmission bar.

Table 2.2: Properties of the impacting surfaces

Material	Alloy	Temper	ρ_s	E	ν	Y
			(kg m^{-3})	(GPa)		(MPa)
Aluminum	6061	T5	2700	68.95	0.33	275.00
Aluminum	2024	T5	2768	73.08	0.33	324.05
Aluminum	7075	T5	2796	71.70	0.33	503.31

The samples were polished close to mirror finish. The polishing process was performed by using ECOMET 3, BUEHLER grinding and polishing table for metallographic sample preparation.

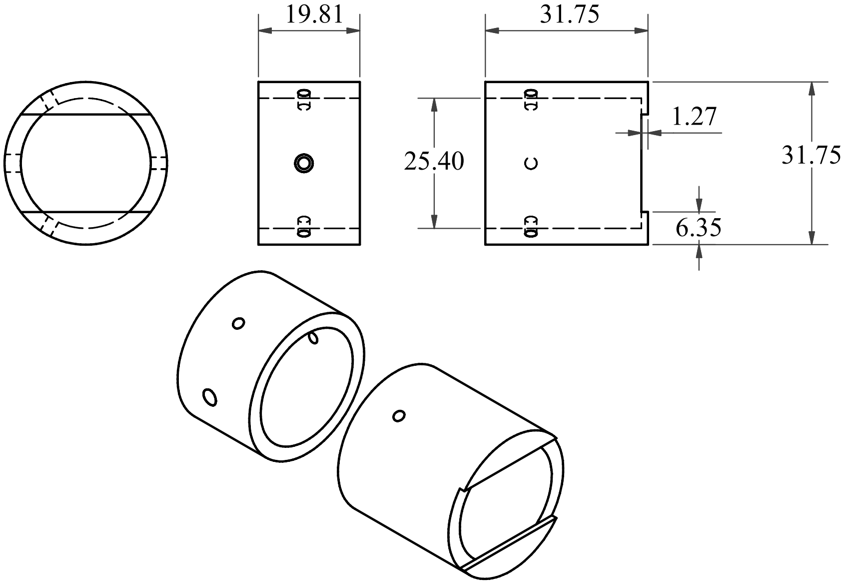

Figure 2.4: Sample holding device

2.1.3 Pressure bar

A variation of the typical Split-Hopkinson-Kosky pressure bar setup is proposed for this thesis. Instead of the incident bar, a spherical particle strikes the specimen, firmly attached to the transmission bar. The length of the transmission bar is long enough so that the contact time of the particle with the end of the bar, including the plastic deformation time if it exists, is less than the time required for an elastic wave to travel the total length, L, and its reflection to return to the point of impact. It is also assumed that the plane compression pulse propagates without distortion through the sample and the bar, and both of them have the same acoustic impedance, Z_0, so that the phase and the bar velocity are equal (see Table 2.3). Additionally, if the striker, in this case the particle, mass is small compared to mass of the transmission bar, the rod behaves like a half-space.

Figure 2.5 shows the variations on coefficient of restitution, e, with the impact velocity, U_i. Three different sets of "dry" experiments were performed using a steel particle of 12.7 mm in diameter as a striker. The first set corresponds to a rigid surface, the Zerodur[3] block. The other two sets of experiments were done using a "softer" material (Al 6061), a 25.4 mm diameter by 254.0 mm long solid bar, and the same bar with a specimen attached

---

[3] Glass-ceramic composite often used to build optical components for telescopes

to the end of it (Figure 2.1). The decreasing tendency on the coefficient of restitution of the bars is attributed to the plastic deformation of the impacts; however, the experiments for the plain solid bar and the bar with the specimen seemed to be be self-consistent with each other.

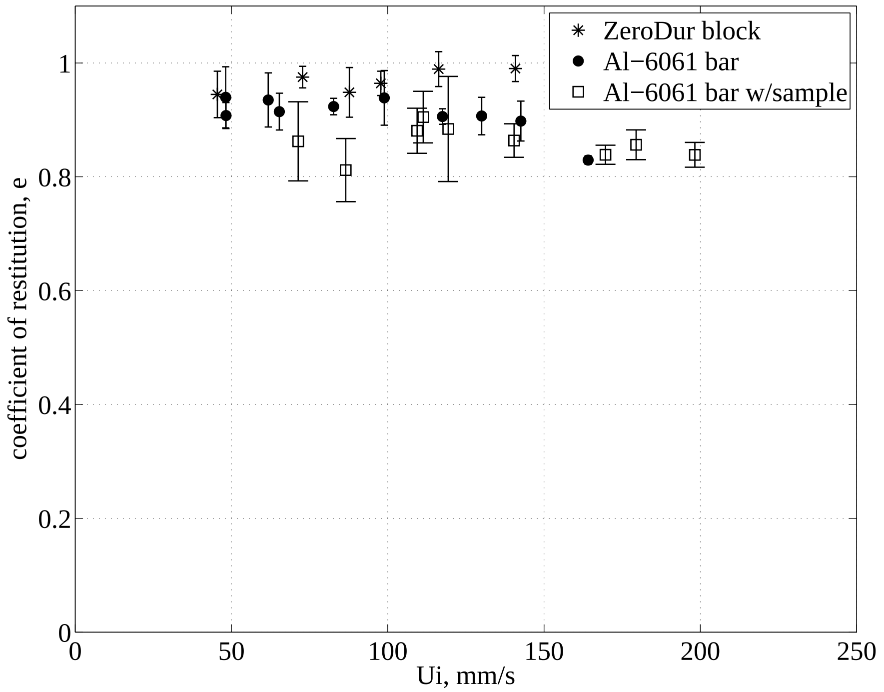

Figure 2.5: Steel particle impinging on three different surfaces: Zerodur block (rigid), Al 6061 25.4 mm diameter with a length of 254.0 mm, and the same bar with a sample attached to one of the ends

The stress pulse produced by the collision generated waves that remained in the elastic regime. As shown in Table 2.3, for the three different alloys, the stress in the pulse produced by the maximum impact speed ($\sim 0.5\ m/s$) is smaller than the yield strength. Therefore, no elastic-plastic waves were produced for any of the experiments. The tabulated values were estimated using Equation 1.30.

Table 2.3: Acoustic properties

Material	Alloy	Acoustic speed, c_0 (m s^{-1})	Impedance, Z_0 (MPa s m^{-1})	Wave stress, σ_B/Y
Aluminum	6061	5053	13.64	0.012
Aluminum	2024	5138	14.23	0.011
Aluminum	7075	5064	14.16	0.007
Ultra-Hard Wear-Resistant Stainless Steel	440C	5107	39.83	- -

2.1.4 Force sensor

The impact force due to the collisions was measured with a quartz crystal used as a force sensor. The proposed Split-Hopkinson-Kosky Pressure Bar (SHPB) was modified by adding a piezoelectric transducer crystal. A single crystal was embedded between the pressure bar and an extra piece of rod as shown in Figure 2.6. In order to hold the crystal between the rods, a commercial conductive epoxy was used to glue the pieces together.

Quartz transducers are excellent choice for dynamic load measurements due to the high natural frequency, on the order of ~ 10 MHz (Lu et al. (2003)), which fulfills the sampling requirements for this experiment. The crystals used for the experiments were obtained from Boston Piezo-Optics Inc. The detailed characteristic of the crystals are shown in Table 2.4.

Table 2.4: Piezoelectric quartz crystal description

Surface:	fine lapped finish
Diameter:	25.4 ± 0.025 mm
Thickness:	0.254 ± 0.025 mm
Piezoelectric constant, normal direction	$d_{11} = -2.3$ pC/N

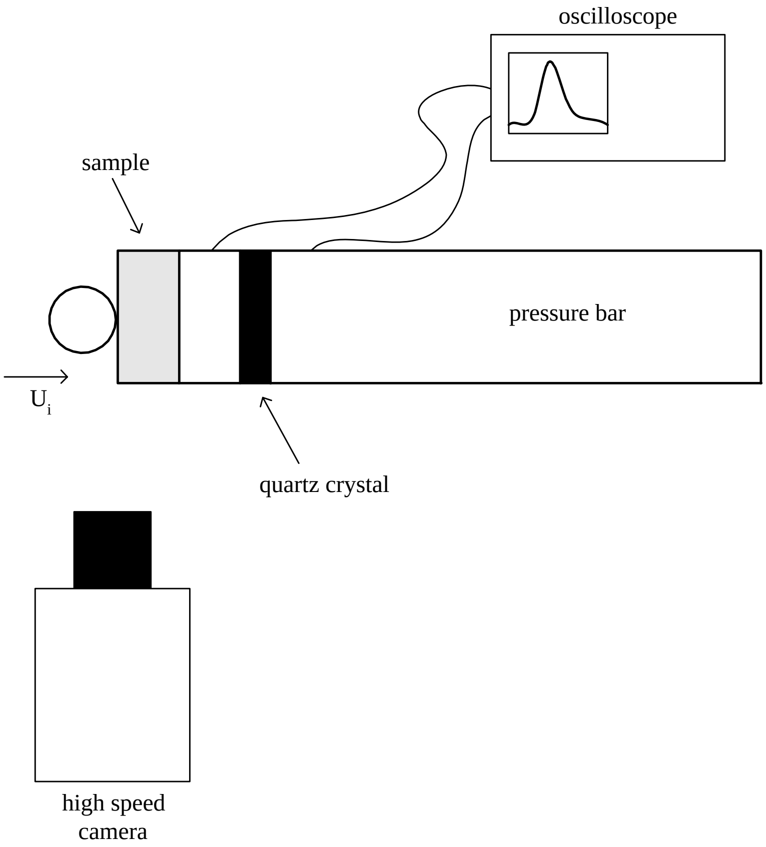

Figure 2.6: Schematic representation of the force sensor setup

2.1.4.1 Calibration

The quartz crystal transducers have an excellent linearity throughout their operational range. Hence, $F(t) = \alpha V(t)$, where F is the force due to the impact, α is the calibration constant and V is output voltage, obtained from the digital oscilloscope. A typical crystal response to a given impact is shown in Figure 2.7. The total contact period is separated into a period of compression, t_c, and a restitution period, t_r. The compression period ends at the maximum value of the impulse. The calibration of the sensor was done only during the compression period, by simply using the equation of motion $F = m\ddot{\delta}$, where δ is the total relative displacement between the two bodies due to compression. At the beginning of the contact $\dot{\delta}(t = 0) = U_i$, and that the particle comes to rest at the end of the compression period, $\dot{\delta}(t = t_c) = 0$. Combining those initial conditions with the linear relation between the force and the output voltage, the calibration constant is given by

$$\alpha = \frac{4}{3}\pi R^3 \rho_p U_i \frac{1}{\displaystyle\int_0^{t_c} V(t)dt} \tag{2.1}$$

In Figure 2.7,the first pulse is attributed to the collision; the second set of pulses are the reflections of the first impulse transmitted throughout the bar. Note that, the collision time is less than arrival time of the the first reflection, which is consistent with the assumptions made when choosing this experimental setup, neglecting the effects of the number of reflections on the coefficient of restitution (Sondergaard et al. (1990)).

The bar was calibrated for collisions spanning the impact velocities used during the experiments. The resulting calibration constants were: $\alpha_{ns} = 323 \pm 8$ N/V for the bar without a sample attached to it, and $\alpha_{ns} = 294 \pm 11$ N/V for the bar with a sample attached to it. Figure 2.8 shows the maximum measured force as a function of the impact velocity, U_i. The data points corresponding to the measurements including the sample, modify slightly the response of the sensor.

Most of the experiments presented in this thesis were beyond the elastic limit. The time required to produce the maximum elastic deformation τ_e given by Equation 1.10 , is estimated using the elastic velocity, U_{el}. This time is greater than the collision time involving plastic deformation since the impact velocity is larger than the elastic velocity ($U_i > U_{el}$). In Figure 2.9 the contact time nondimensionalized by the maximum elastic

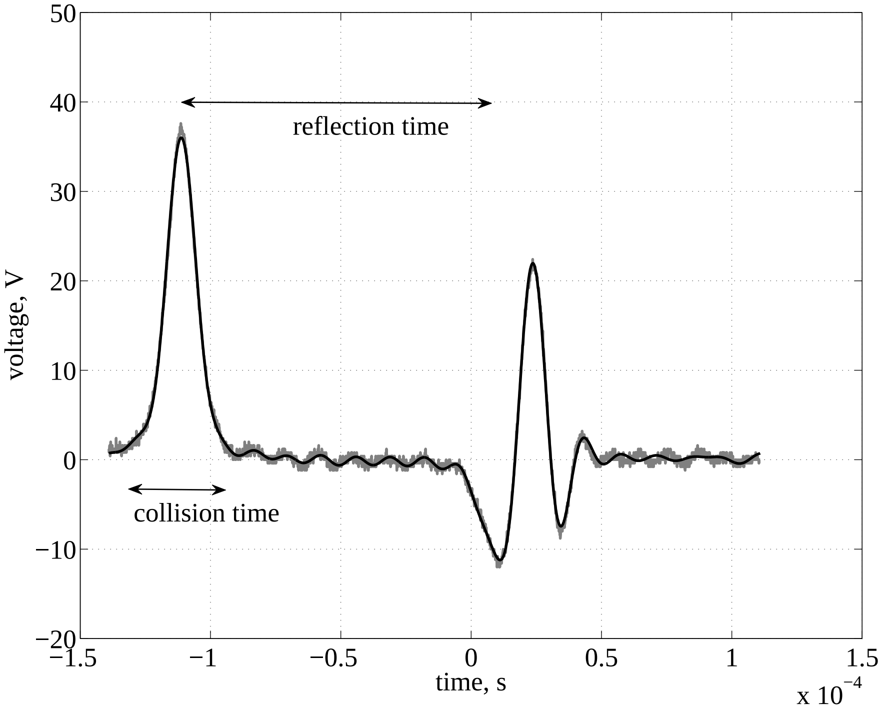

Figure 2.7: Typical signal obtained from the embedded quartz crystal in the SHPB.

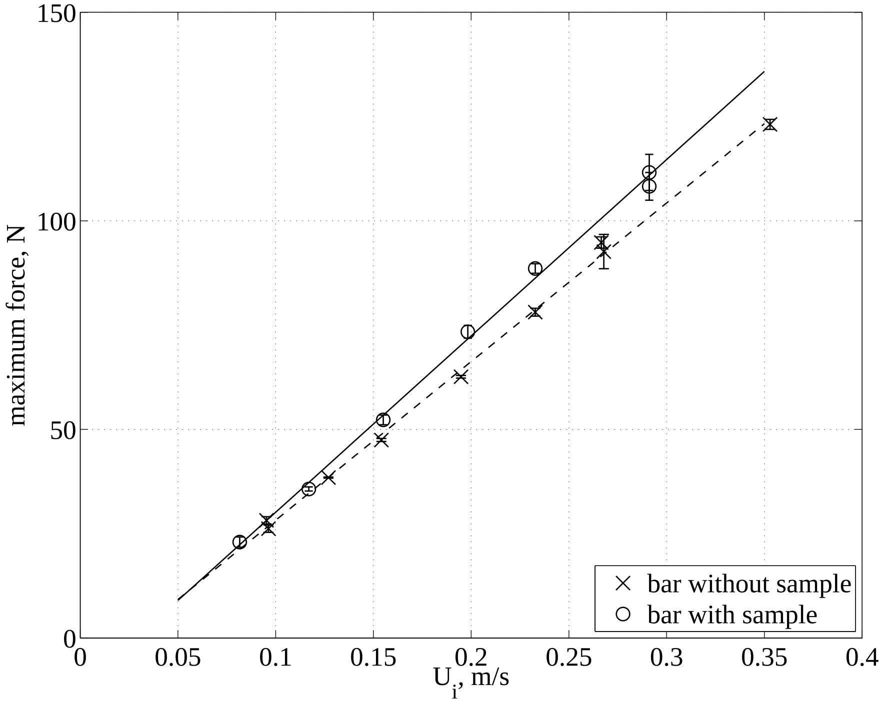

Figure 2.8: Contact force plotted as a function of the impact velocity U_i, comparing the results of using only the pressure bar, with the results of the pressure bar with the attached sample.

time is plotted versus the normalized impact velocity. For all the collisions, the contact time decreases as the impact velocity increases. The collision time is divided in elastic and elastic plastic. The elastic deformation time is a function of the impact velocity, meaning that for larger impact velocities the elastic deformation happens faster. The rest of the collision time corresponds to the plastic period, τ_p, given by Equations 1.10 and 1.27. The plastic period is "independent" of the impact velocity, it is only a function of the dynamic pressure, p_d, and it monotonically decays as $\sim O(1/\sqrt{p_d})$. The discussion in Section 4 suggested that in the elastic-plastic regime, p_d can vary between $1.1 < p_d/Y < 2.8$. As the impact velocity increases, the equivalent load does as well increasing the strain applied on the materials, resulting on increasing the dynamic pressure. As seen in Figure 2.9, the compression time nondimensionalized by the maximum elastic collision time, τ_e^*, decreases as the impact velocity increases.

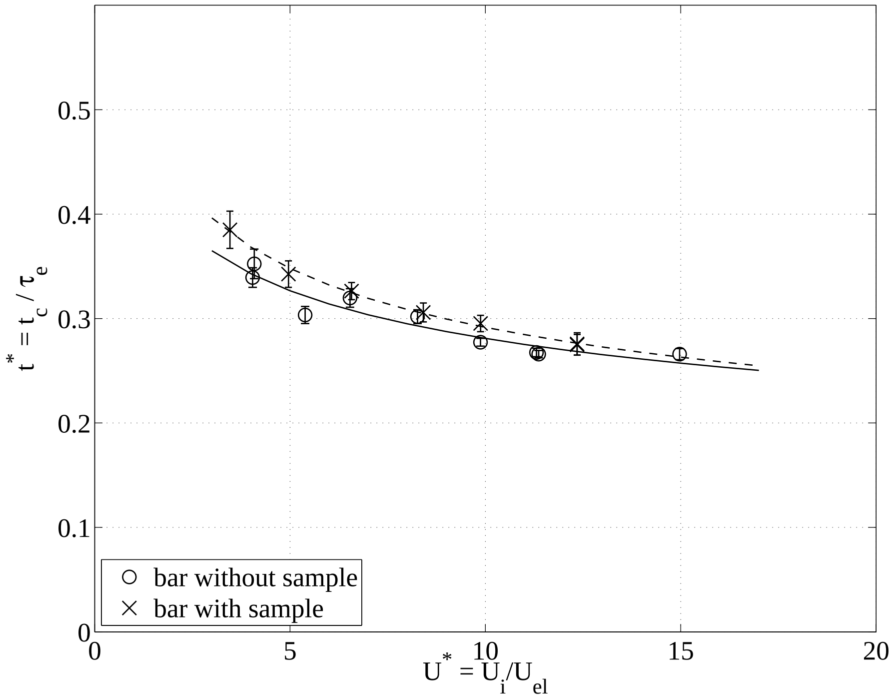

Figure 2.9: Contact time nondimensionalized by the maximum elastic time plotted as a function of U^*.

2.1.5 Glycerol-water mixtures

Glycerol-water mixtures (0 – 80% weight, $1 - 50 \times 10^{-3}$ Pa s) were used as the viscous fluid. To estimate the viscosity two parameters were needed, the specific gravity of the mixture and its temperature. A *hydrometer* calibrated from 1.000 to 1.225 SpGr, was used to read the specific gravity. The temperature of the fluid was constantly monitored with a digital thermometer [4] immersed in the tank. The resulting viscosity was estimated by interpolating tabulated values (Lide (2001)).

Table 2.5: Different fluid viscosities and densities

Fluid	Glycerol (% weight)	Temperature, T (^oC)	Viscosity, μ $(Pa \cdot s)\times 10^{-3}$	Density, ρ_f (kg m^{-3})
Air	0	25	0.0019	1.205
Water	0	25	0.9028	997.1
Glycerol-water	24	25	1.8070	1055.4
Glycerol-water	54	25	6.6610	1134.7
Glycerol-water	62	25	10.4070	1156.6
Glycerol-water	75	25	28.3500	1191.9
Glycerol-water	78	25	39.5400	1200.0
Glycerol-water	82	25	61.6000	1210.7

Figure 2.10 shows the changes in viscosity as a function of the temperature for different concentrations. The viscosity is sensitive to the temperature; throughout the experiments, the variations were kept within 2–4 ^{o} C.

---

[4] OMEGA HH11

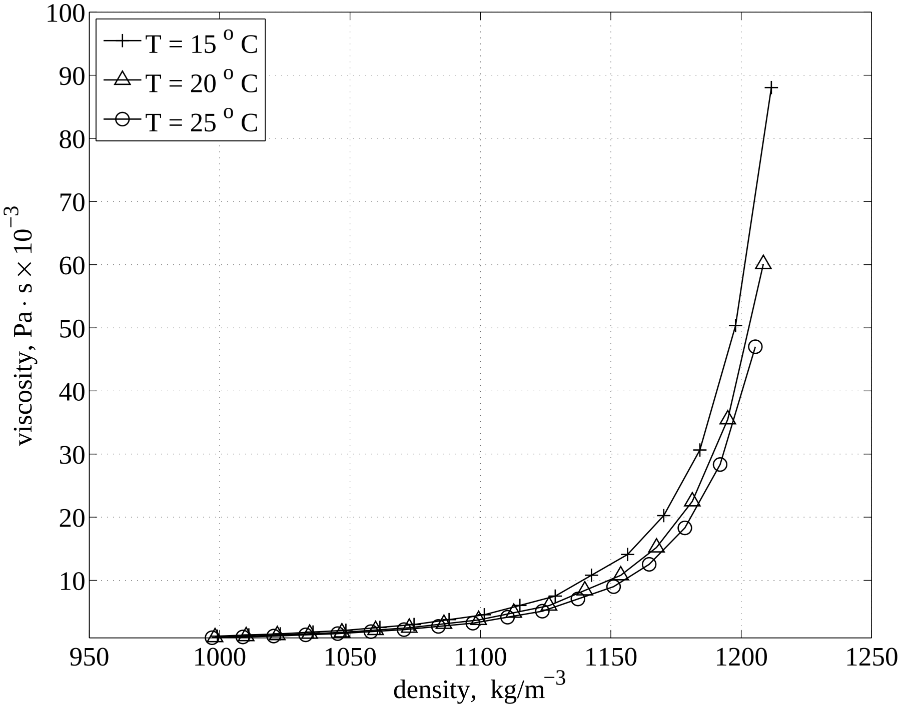

Figure 2.10: Variations in viscosity due to temperature for glycerol-water mixtures between 0–82 % wt. The selected range was representative for the experiments presented in this thesis.

Chapter 3

Experimental techniques

This section describes the various techniques used during this experimental work. Although the experimental setup is simple, preparing and post-processing each individual experiment turned out not to be trivial. The sequence of steps used during the experiments can be summarized as follows: sample surface preparation, image processing, and characterization of the indentation parameters (measuring and processing). Each of those steps are described in detail, and applied to one experiment. The experiment event number is: 1207, corresponding to a stainless steel particle colliding with an alloy 6061. The surrounding liquid was a mixture of 82% glycerol dilute in water.

3.1 Sample surface preparation

The impacting samples were cylindrical discs (see Figure 2.1) made out of aluminum rods. The properties of the different alloys are summarized in Table 2.2. Each sample was machined individually by either: cutting and facing them on both sides using a lathe, or by cutting them on a bench saw and then lapping both sides, ensuring that the surfaces were flat. The sample surfaces were polished after being machined. Since the smallest indentations created after the impact were on the order of the semi-raw surface roughness, it was impossible to observe them on the samples without surface treatment. The average surface roughness after machining was about $0.38 < \sigma_s < 0.64$ μm (see Figure 3.1). The ECOMET 3 BUEHLER, which is a semi-automatic grinder and polisher, was used to smooth down all the the sample surfaces up to $\sigma_s \sim 0.029$ μm. To obtain the final surface roughness, six simultaneous samples were placed on a circular holder that was coupled to the ECOMET 3; this circular holder was pressed up against a plate, where different grits were placed, and rotated differentially. The surfaces were gradually polished from the more coarse grits to the smooth polishing cloths. The grit sizes were 180, 320, and 600 (see Figure 3.2). After the grits, the samples were polished with adequate polishing cloths and different water-based suspensions of polycrystalline diamond, [1] 9 μm and 3 μm (see Figure 3.3).

Table 3.1: Different sample processes and their respective root mean square R_q and surface roughness, σ_s. Note that after the 9 μm solution the variations on σ_s are small.

Sample preparation process	R_q (μm)	σ_s (μm)
Lathe	0.465	0.376
Lap	0.925	0.638
320 grit	0.419	0.336
600 grit	0.184	0.144
9 μm solution	0.028	0.020
3 μm solution	0.140	0.097
2 μm solution	0.049	0.038

Table 3.2: Different sample processes and their respective root mean square R_q and surface roughness, σ_s. Note that after the 9 μm solution the variations on σ_s are small

Different values for measured surface roughness, σ_s, and root mean square, R_q, are shown in table 3.2. The variations on σ_s are small for the diamond solutions; therefore, most of the samples' final surface roughness was a result of the 9 μm suspension. On top of that, the surface roughness influences the accuracy of measurements in contact dynamics (Joseph et al. (2001)).

Figures 3.1, 3.2, 3.3, and 3.4 show the typical surface roughness for each of those steps. The images were taken with the optical profilometer, WYKO (see Section 3.3).

---

[1] The cloth works as a matrix for the abrasives, which are the diamond particles.

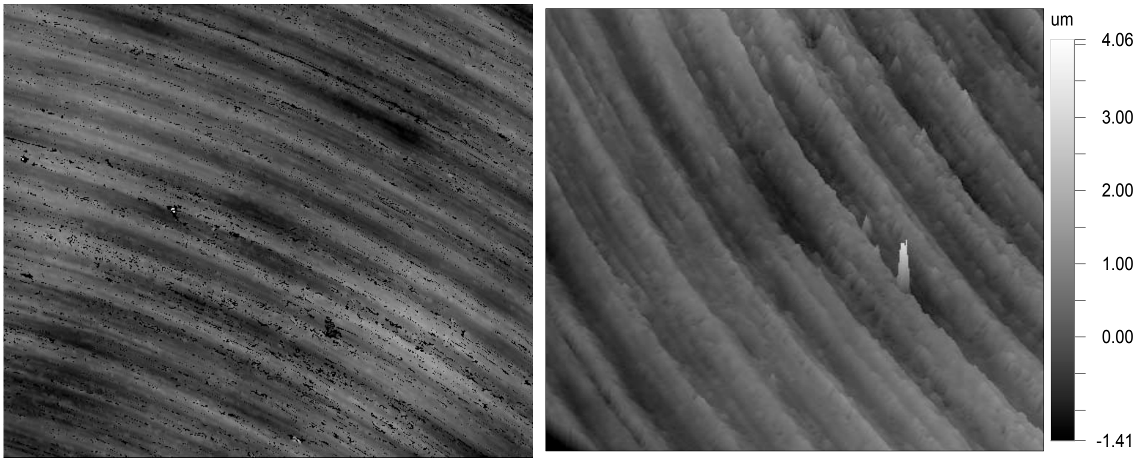

(a) Lathe machining, 2-D (b) Lathe machining, 3-D

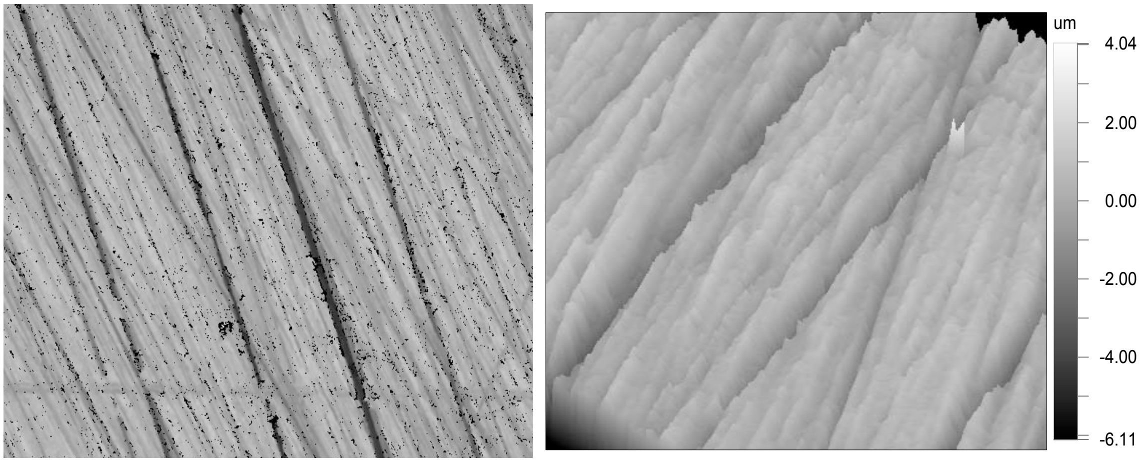

(c) Lapping and grinding, 2-D (d) Lapping and grinding, 3-D

Figure 3.1: Typical WYKO 2-D and 3-D pictures of the surfaces of the samples after being machined with the lathe (a, b). The lower panel (c, d) shows the typical surfaces of the samples after being lapped and pre-ground.

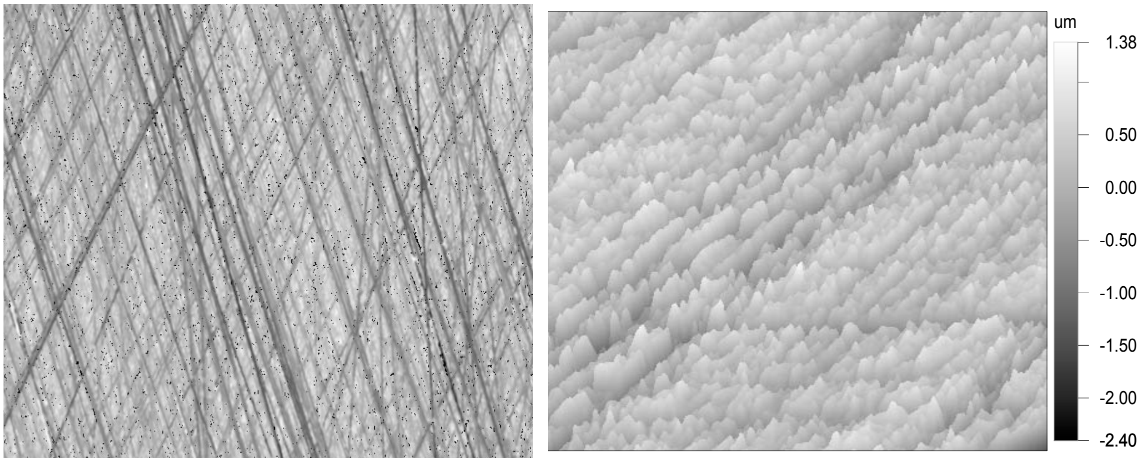

(a) Grit 320, 2-D

(b) Grit 320, 3-D

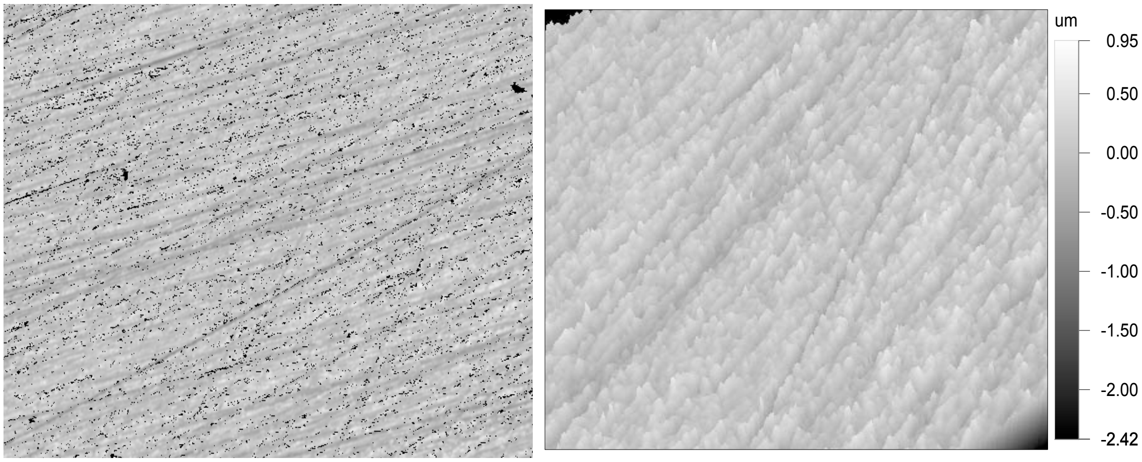

(c) Grit 600, 2-D

(d) Grit 600, 3-D

Figure 3.2: Typical WYKO 2-D and 3-D pictures of the surfaces of the samples after being ground down with the 320 grit (a, b) and the 600 grit (c, d)

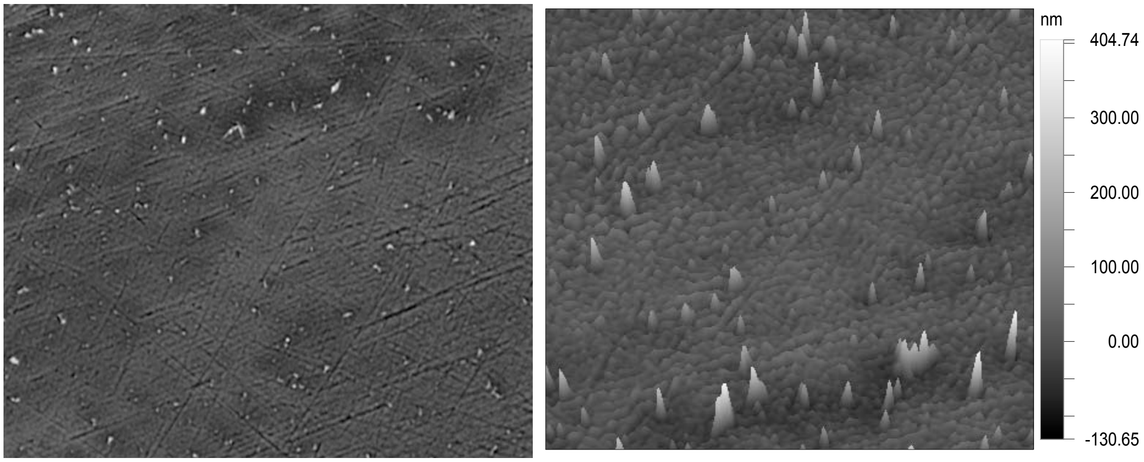

(a) 9μ m diamond solution, 2-D (b) 9μ m diamond solution, 3-D

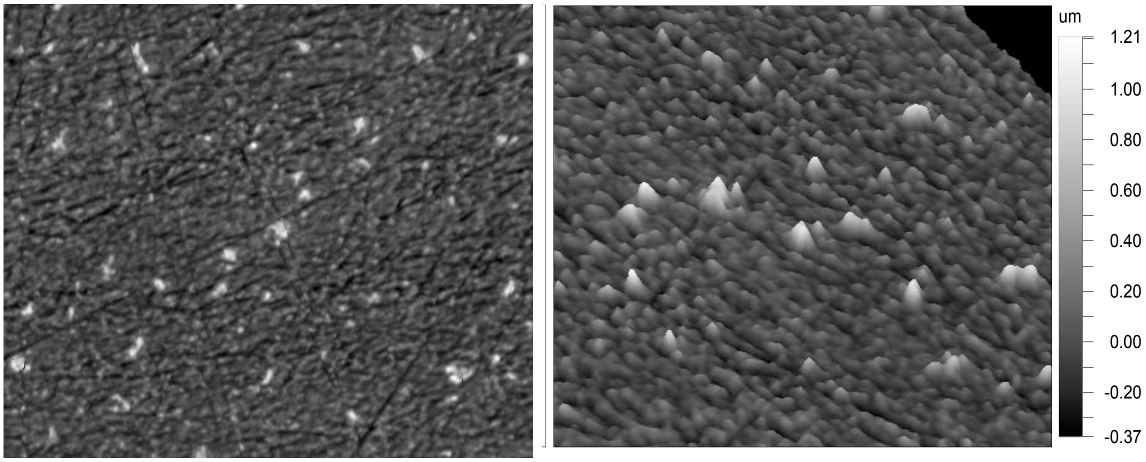

(c) 3μ m diamond solution, 2-D (d) 3μ m diamond solution, 3-D

Figure 3.3: Typical WYKO 2-D and 3-D pictures of the surfaces of the samples after being polished with two different diamond solutions: 9μ m (a, b) and 3μ m (c, d)

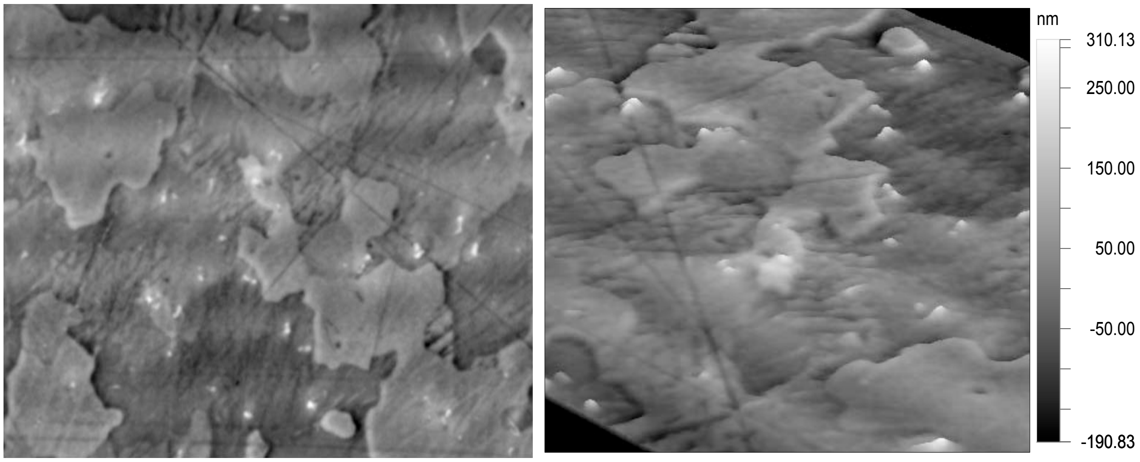

Figure 3.4: Typical WYKO 2-D and 3-D pictures of the surfaces of the samples after being polished with the micro-cloth and 0.5 μm diamond solution

3.2 Image processing

The motion of the sphere was recorded with a Redlake MotionScope 8000 high-speed camera with a recording frame rate ranging from 60 to 8000. The maximum resolution of the camera, 480 × 420 pixels, corresponded to 60 fps. Since the camera has a fixed amount of storage memory, increasing the frame rate corresponded to decreasing the resolution of the images. Most of the experiments were recorded at 1000 fps. The experiment was illuminated with two sources of light placed opposite to the camera. To avoid reflections from the particles, the background light was moderately diffused by wrapping translucent white paper on the back and sides of tank. A typical raw image obtained from the high speed camera is shown in Figure 3.5.

After recording each experiment, the resulting images were analyzed by using *ImageJ* [2]. Sequenced frames were extracted from the recorded movies and transformed into black and white images based on the threshold of each frame: as shown in Figure 3.5 values below the threshold were transformed into white pixels; likewise, values above the calculated threshold corresponded to black pixels.

The position of the centroid of the particle was tracked for each frame. The resolution of the images was 352 × 240 pixels, and the centroid was tracked without modifying the aspect ratio of the images. On average, the major and minor axis of the fitted ellipse were 160 by 150 pixels. Assuming an effective diameter for the ellipse and comparing it with

---

[2] `http://rsb.info.nih.gov/ij/`

the actual particle diameter in mm, the data was scaled. Figure 3.5 shows typical images resulting from the particle tracking process.

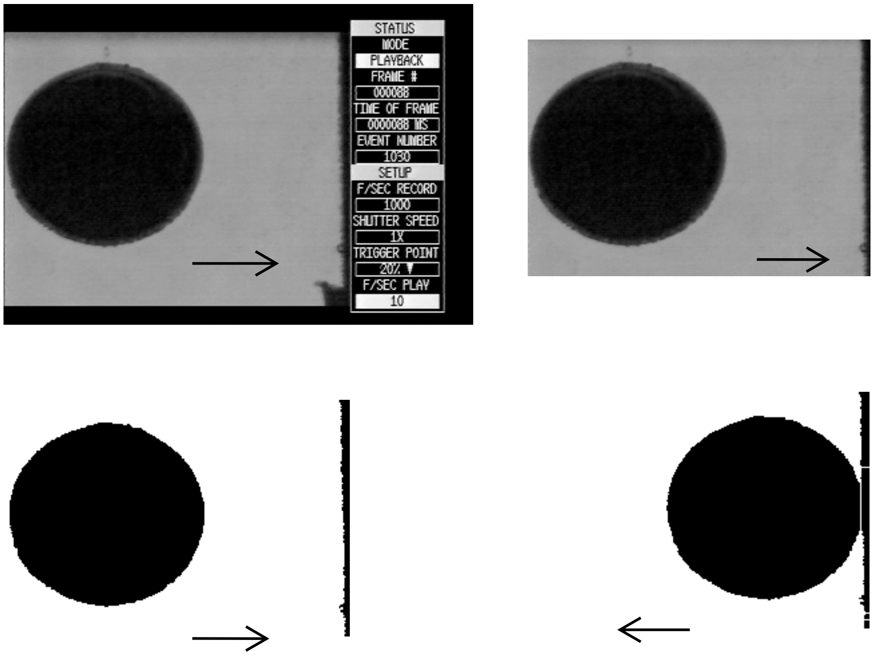

Figure 3.5: The captured images cropped and converted into black and white images based on the threshold. The center of the b&w image was tracked. The images in the lower row are separated by 100 frames; the lower-right image shows the contact between the particle and the wall.

The particle impact and rebound velocities, U_i and U_r, were calculated by linearly fitting the data before and after the collision. From the resulting velocities, the coefficient of restitution is defined as:

$$e = -\frac{U_r}{U_i}. \tag{3.1}$$

The number of data points used to fit the lines was selected based on the expected velocity. Relatively slower collisions required more data points than faster collisions. The scatter in the data was more pronounced for slow collisions, experiments where the velocity approached zero rather slowly were more sensitive to the small variations on the effective diameter, i.e., the variations on the number of pixels corresponding to the particle diameter were on the order of the particle displacement between frames. For example, three different collisions are shown in Figure 3.6; as mentioned before, the number of recorded points within the same window of time is a lot smaller for relatively fast collisions than it is for the slower ones. For the largest velocity presented ($\circ$), few points were necessary to describe the impact velocity. On the other hand, for the slowest experiment ($+$), the number of points required was larger.

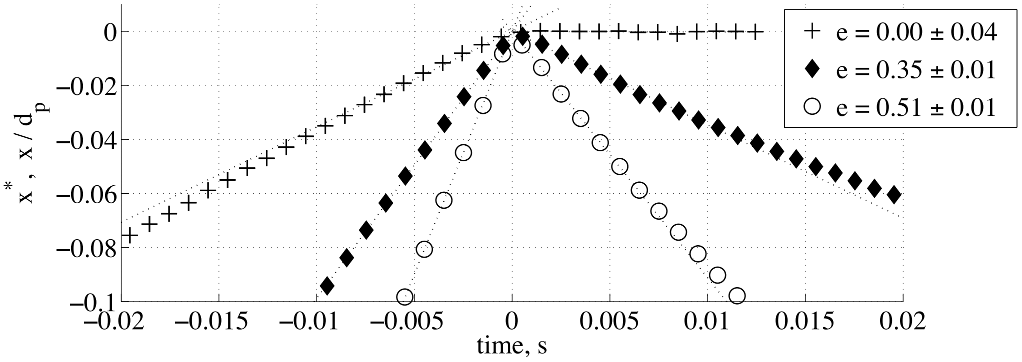

Figure 3.6: Trajectories of a steel particle impinging on Al 2024 alloys. Three different scenarios are shown: ($+$) $St = 16$ and $Re = 22$, (♦) $St = 44$ and $Re = 61$, and ($\circ$) $St = 80$ and Re $= 111$.

For convenience, $(x, t) = 0$ was defined as the intersection point of the lines describing the impact and rebound velocities. Figure 3.7 shows, on the upper panel, the corresponding data points describing the trajectory of a steel particle impacting an aluminum alloy 2024 sample; the surrounding liquid was a 70% by weight glycerol-water mixture. The impact and rebound velocities resulting from the slopes of the fitted lines were: $U_i = 193\ mms^{-1}$ and $U_r = 96$ mm s^{-1}, with a coefficient of restitution, $e = 0.50 \pm 0.01$. The plot in the lower panel corresponds to the instantaneous particle velocity which was calculated using fourth-order central differences scheme. The corresponding errors on the coefficient of restitution were calculated based on the uncertainty in calculating U_i and U_r.

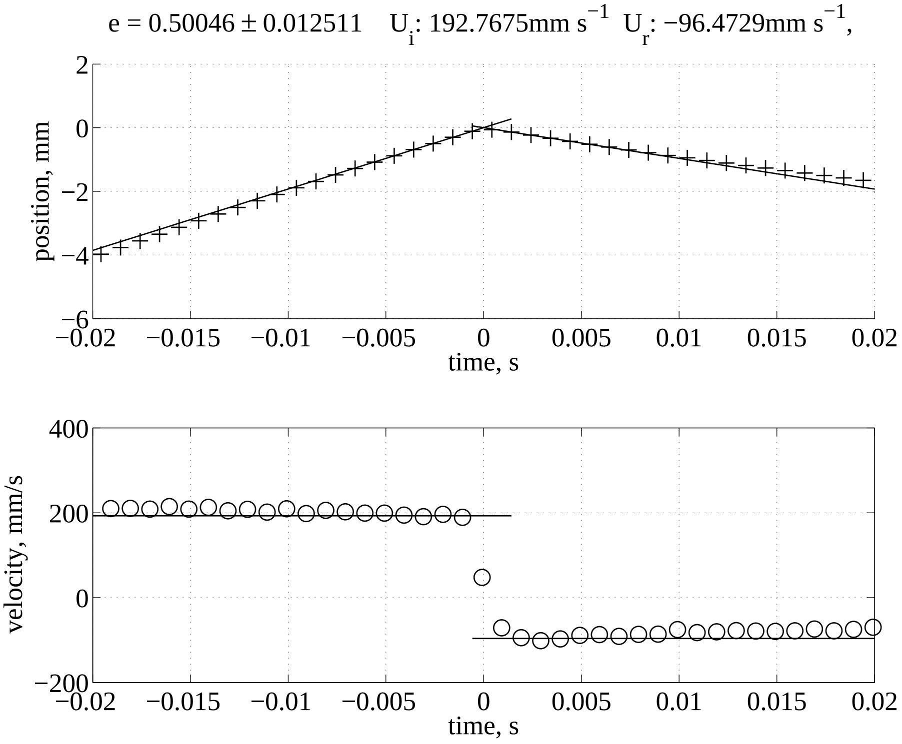

Figure 3.7: Particle position (top) and resulting velocity (bottom) for a steel particle, 12.7 mm in diameter, impacting a sample of Al 2024. The corresponding Stokes number, $St = 68$, $Re = 95$. The sample presented a permanent indentation after the collision.

Alternatively, an image cross-correlation method was implemented, where an image template taken from a given sequence of images was cross-correlated with all the frames. The maximum of the cross-correlation function indicated the location of the center of the particle. Figure 3.8 shows the resulting horizontal position of the particle's center as a function of time. In the lower panels, the frame and its resulting correlation with the template are shown. All the experiments were processed by using *ImageJ* software, due to a relatively large scatter resulting from the cross-correlation method compared to the software.

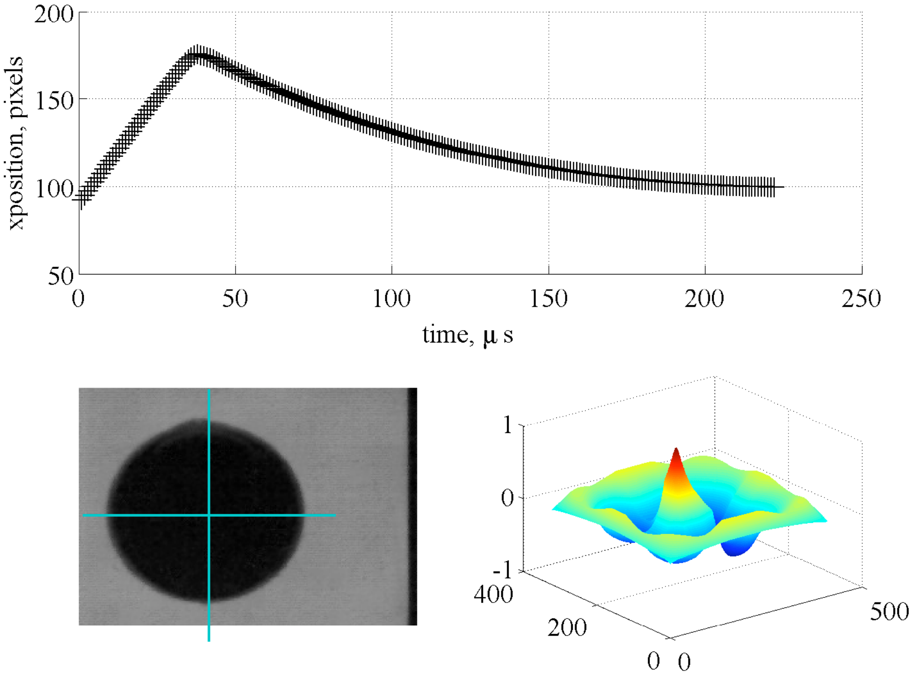

Figure 3.8: The particle position in pixels as a function of time. The lower panels show the center of the particle resulting from the maximum of the cross-correlation function shown on the lower-right panel.

3.3 Wyko, optical profilometer

The Wyko optical profilometer is a non-contact white-light interferometer which can measure surfaces heights from 0.1 nm to 500 μm with a vertical resolution of 0.1 nm. The samples were measured using $5X$ and $10X$ objectives, depending on the expected size of the indentations. By using the built-in software it was possible to obtain the 3D information required to measure the indentation parameters for each sample. The resulting deformations from the experiments were characterized by their crater diameter, d_c, and their indentation depth, H. Figure 3.9 shows a representation of the typical deformation parameters resulting from a particle collision with a flat wall.

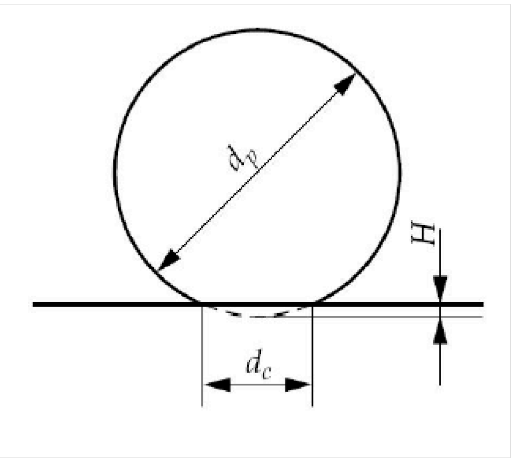

Figure 3.9: Geometry of spherical indentation resulting from a solid particle on a flat surface

Besides the deformation parameters, the topological characteristics of the surfaces for each sample were also measured, since the variations of the surface roughness influences the accuracy of the measurements in contact dynamics (Joseph et al. (2001)). The measured quantities were: the surface roughness, σ_s, and the "root mean square", R_q

$$\sigma_s = \frac{1}{A}\int_0^{Lx}\int_0^{Ly} |z(x,y) - \hat{z}(x,y)|\, dydx \tag{3.2}$$

where $z(x,y)$ is the height within the sampling area, A, and $\hat{z}(x,y)$ is the center plane from where the mean square deviation is a minimum. This implies that the volume of roughness above this center plane and below are exactly the same. From a statistical point of view, the root mean square, R_q, or the standard deviation of the height of the surface from the mean center plane, $\bar{z}(x,y)$ is defined as:

$$R_q^2 = \frac{1}{A}\int_0^{Lx}\int_0^{Ly} \left(z(x,y) - \bar{z}(x,y)\right)^2 dydx. \tag{3.3}$$

For most of the surfaces presented in this work, σ_s and R_q were on the same order of magnitude, since $\bar{z}(x,y) \approx \hat{z}(x,y)$. Hence, the term "surface roughness" will be used only as σ_s throughout this thesis. Figure 3.12 shows typical $y-z$ and $x-z$ surface profiles. Those profiles were measured after the sample of alloy 606 was polished following the procedure previously described.

3.4 Tilt correction and surface smoothing

The output raw data from the optical profilometer, Wyko, was post-processed separately. The first correction was done by suppressing the erroneous peaks and valleys. Secondly, although the samples were lapped and their surfaces were nearly parallel, the output raw data often presented some tilting, which in some cases was on the order of magnitude of the measured indentations. Finally, the resulting indentation parameters have larger length scales compared to the average surface topography. The surfaces were smoothed by suppressing the higher wavelengths using a low-pass filter.

3.4.1 Peaks and valleys suppression

The output data resulting from the built-in software of the WYKO profilometer used to measure the surfaces' topography is often noisy. The raw measurement often has gaps that correspond to a reflected beam that was not captured; the software represents those gaps with either large peaks or deep valleys. To remove those gaps and preserve the surface roughness, the peaks and valleys are replaced by predicted values, which are estimated based on the roughness on the vicinity of the peak or valley. Each of the vertical and horizontal profiles from the raw image were fitted to a large-order polynomial ($15th$); the peaks and valleys are values larger than two standard deviations of the corresponding profiles and those values are replaced by the fitted values. The cut off criteria of $2\sigma_s$ was an arbitrary definition. Figure 3.10 shows the raw output data and the result of the suppression discussed before. The experiment corresponds to the event number 1027; the same experiment will be used as an example throughout this section.

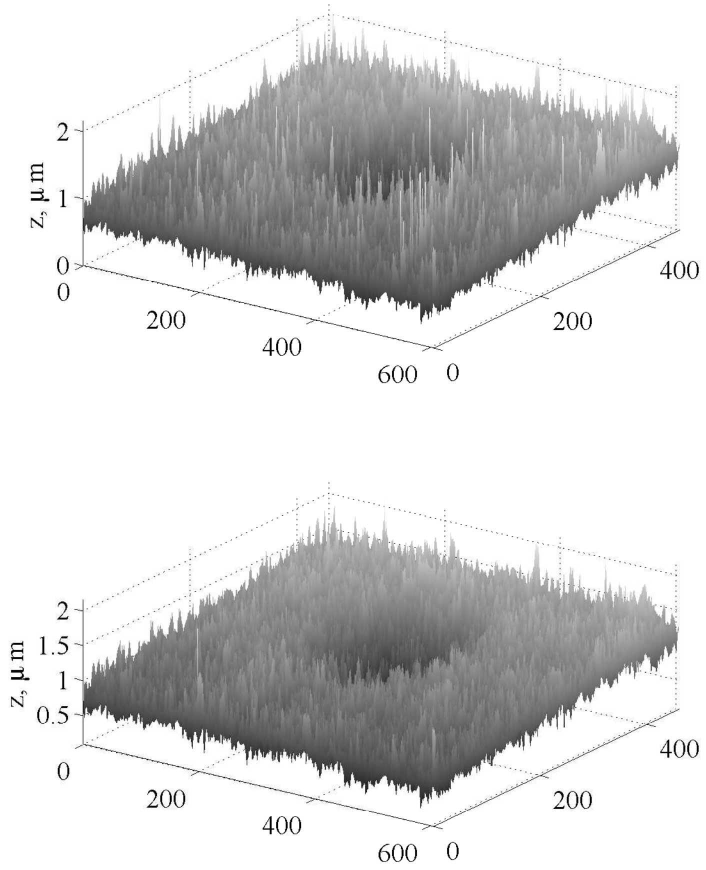

Figure 3.10: The upper panel shows the output data from the Wyko software; the lower panel shows the resulting smoothed surface by using the peaks-and-valley suppression filter. The images are the result of the impact of a stainless-steel particle (See Table 2.1) in a 70% glycerol-water mixture. The corresponding Stokes number and the xxxxxx

3.4.2 Tilt correction

Most of the 3D surfaces are fairly isotropic (or weakly anisotropic), in terms of surface roughness, in any direction (Thomas (1982)). As a result of the surface preparations — grinding and polishing — the surfaces are almost two-dimensional on the $x - y$ plane. However, the individual profiles, $x - z$ and $y - z$, have a preferential slope (See Figure 3.11), in a particular direction or in both directions. The magnitude of the *tilt* cannot be neglected for most of the cases. In surface technology, the *tilt* is known as the RMS slope parameter defined as the root mean square of the ordinate slopes dx/dz within the sampling length (Griffiths (2001)). Since the surfaces are nearly isotropic, the slope of one individual profile is comparable with any other slope in the same direction; therefore, the slopes dx/dz and dy/dz of single profiles were estimated and then subtracted from the rest of the corresponding profiles.

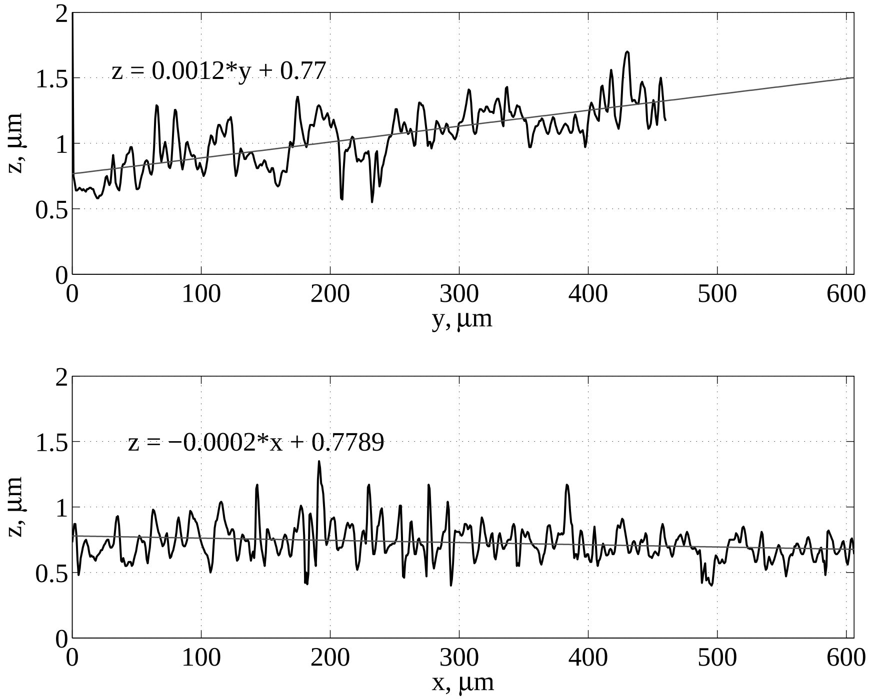

Figure 3.11: Typical $x - z$ and $y - z$ raw profiles corresponding to the measured surface of a 6061 alloy sample. On each profile, the fitted line and the equation is shown. The fitted data was subtracted from the corresponding profiles (see Figure 3.12).

Figure 3.11 shows the typical tilted profiles. By subtracting the tilting factor the *zero* in z direction corresponds to the average surface roughness; this is convenient for further analysis. Figure 3.12 is a typical example of the result from this analysis, where the profiles from Figure 3.11 were un-tilted. In addition to the tilt correction, $z = 0$ corresponds now to the average of the surface roughness.

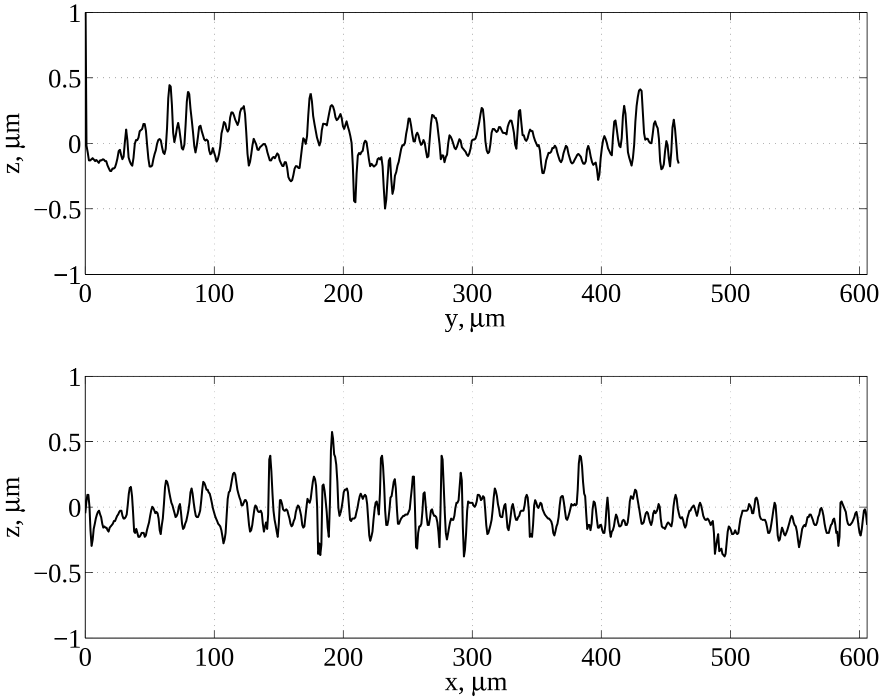

Figure 3.12: The X and Y profiles resulting from the tilt correction. Notice that the $z = 0$ corresponds with the average of the surface roughness.

3.4.3 Low-pass filter

Typically, the characterization of the post-collision surfaces requires measurements of the surface roughness and the indentation parameters. In terms of wavelengths, those two sets of measurements could be separated since their wavelengths are clearly different; the indentation parameters have larger wavelengths than the surface roughness. To characterize the surface roughness, the Equations 3.2 and 3.3 were used on the profiles resulting from the peak and valley suppression. After the valley and peak suppression filter, a low-pass filter was applied to remove the roughness and the waviness. At large wave numbers the surface topography is dominated by the roughness. Moderate wave numbers describe the waviness of the surface. At a very small wave numbers, the indentation's form is preserved; the indentation parameters were measured after combining these three effects.

3.4.3.1 Ideal surface

Figure 3.13 shows an ideal surface profile representing the three characteristic wavelengths discussed above. The surface was artificially made by superimposing sinusoidal functions with three different wavenumbers and amplitudes. The lower panel shows the associated power spectrum in Fourier space. The peaks correspond to the characteristic wavenumbers previously defined. The following sequence of images shows the result of low-pass filtering the profiles using cutoff wave numbers below the characteristic wave numbers. Figure 3.14 shows the result of removing the roughness using a cutoff wave number that is slightly below the characteristic roughness wave number; the resulting profile keeps both waviness and form. The wavelength of the indentation parameters is larger than the waviness. The upper panel of Figure 3.15 shows the profile resulting from the second low-pass filter with a cutoff wave number below the waviness peak. The lower panel compares the ideal raw data with the data resulting from low-pass filtering below the waviness characteristic wave number.

For this ideal example, the window of wave numbers between two characteristic wave numbers were equally valid since the power of those wavenumbers is equal to zero. Real surfaces have more complicated power spectrums and there is no generally agreed wavelength that divides roughness from waviness; it is a matter for subjective assessment.

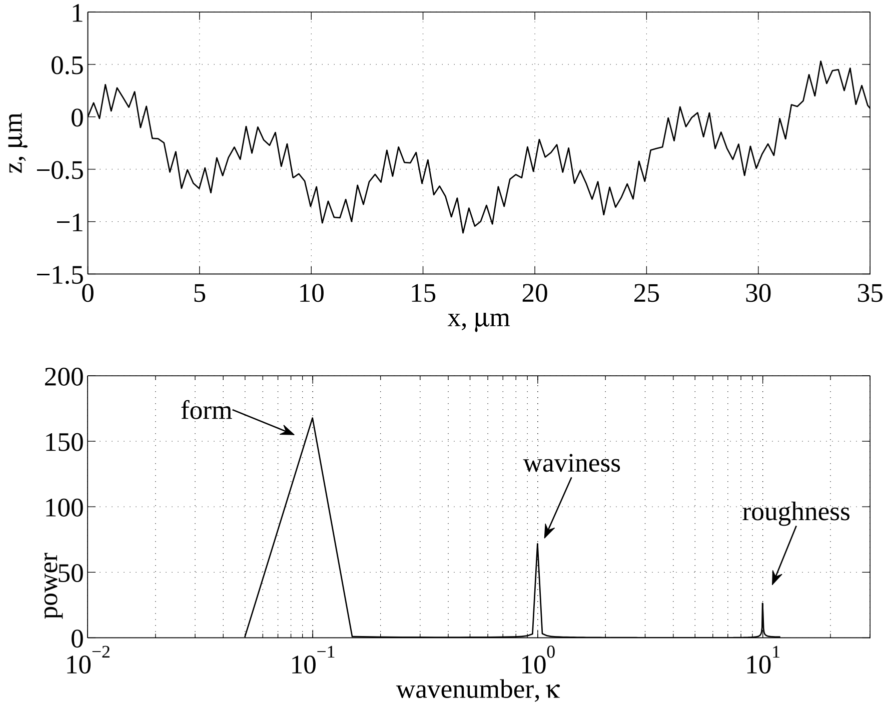

Figure 3.13: Ideal indentation surface profile (top), and the corresponding power spectrum (bottom).

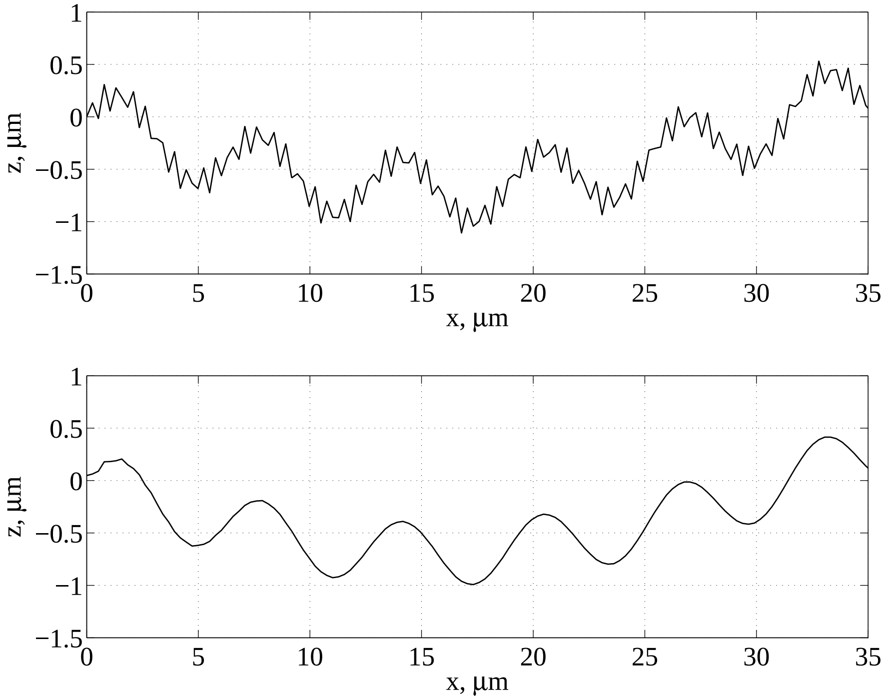

Figure 3.14: Ideal surface profile (top), and the profile resulting from low-pass filtering the roughness while still preserving the waviness (bottom).

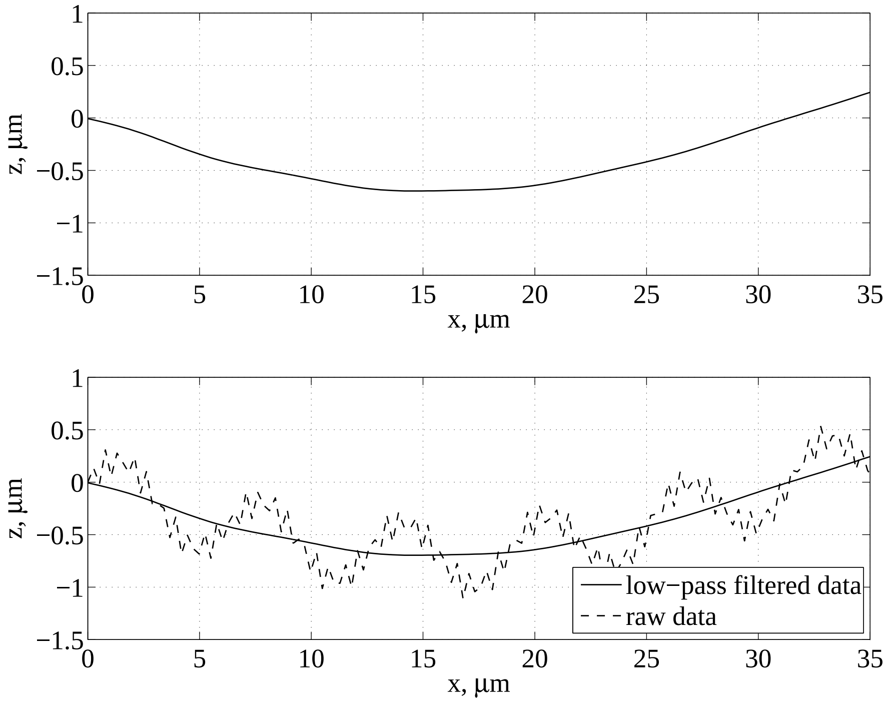

Figure 3.15: Surface profile resulting from low-pass filtering both the surface roughness and the waviness from the ideal surface profile (top), and the combined raw profile and the low-pass filtered surface profile (bottom).

3.4.3.2 Real surface

For the same event used in Figures 3.12 and 3.11, the corresponding $x - z$ and $y - z$ indentation profiles are shown in Figures 3.16 and 3.17. Those profiles were previously filtered by suppressing the peaks and valleys, and tilt corrected[3]. The associated power spectrums are plotted below each profile.

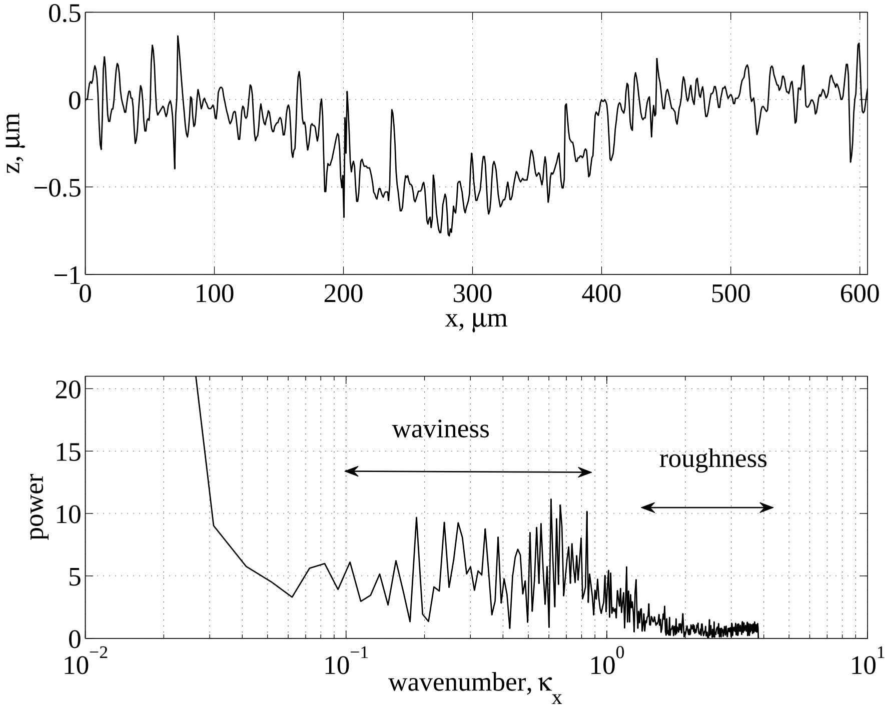

Figure 3.16: $x-z$ indentation profile (top), and the corresponding power spectrum (bottom) showing the waviness and roughness wave numbers. Event number: 1027

After the two previous filtering stages, the entire domain of the images was divided in $x - z$ and $y - z$ profiles, which were individually low pass filtered. In Fourier space a sharp step function was superimposed, removing all the wave numbers greater than a cutoff wave number, κ_c; the remaining data points were inverse transformed, resulting in a smooth curve preserving the shape of the indentation. Figure 3.18 shows the result of the low-pass filter used on the profiles from Figures 3.16 and 3.17. The cutoff wave number used was $\kappa_c = \kappa_x = \kappa_y = 0.05\mu m^{-1}$. This cutoff wave number allows wavelengths, λ, greater than

---

[3] Note that the indentation depth is on the order of the previous tilting absolute distance.

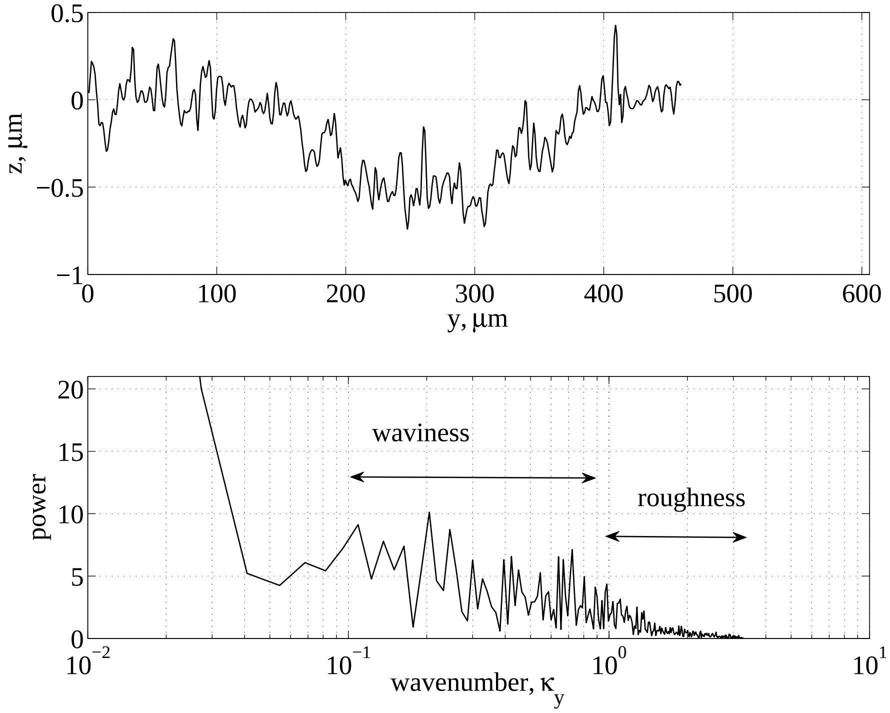

Figure 3.17: $y-z$ indentation profile (top), and the corresponding power spectrum (bottom) showing the waviness and roughness wave numbers. Event number: 1027

125 μm. The next section describes the indentation parameters, such as the crater diameter, which is on the order of the remaining wavelengths.

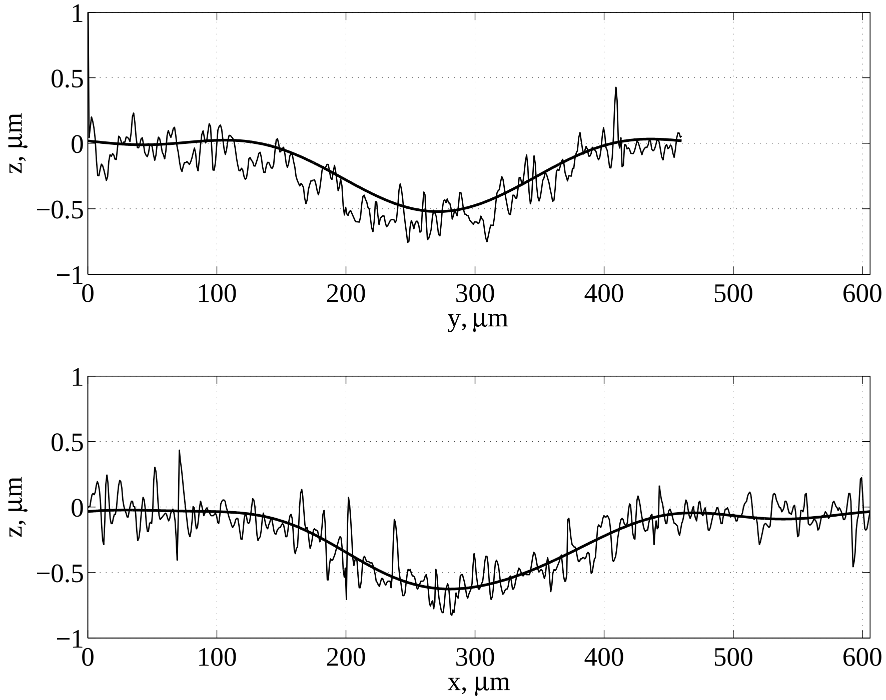

Figure 3.18: Raw and low-pass filtered profiles, $y - z$ (top) and $x - z$ (bottom). The cutoff wave number used was $\kappa = 0.05 \mu m^{-1}$. Event number: 1027

3.5 Indentation parameters

The indentations were characterized by the crater diameter, d_c, and the indentation depth, H. Figure 3.9 shows the indentation parameters resulting from a spherical indenter with diameter, d_p. For all the indentations measured, the data was pre-filtered using the three stages described in Section 3.4.

Figure 3.19 shows 3D images resulting from the first two filtering stages (upper panel) and the final low-pass filter (lower panel). The indentation parameters were measured after the final low-pass filter stage. Since all the collisions presented in this work were normal, the indentations should follow closely the shape of the impacting particle (quasi-conformal elastic-plastic contact), as shown in Figure 3.9. To start the analysis, the reference point was taken as the location of the *theoretical indentation's center*, (x_{tc}, y_{tc}), corresponding to the minimum depth of the previously filtered data.

3.5.1 Crater diameter, d_c

From the contours of the full-filtered data, the crater diameter was measured by fitting circles and ellipses, in a least-squares sense, to the concentric closed contours. The resulting fitted contours were post-processed, and based on a set of geometrical constraints the appropriate contour was elected. The algorithm chose the best contour based on the following three parameters: The circular *eccentricity*, given by Equation 3.4, is defined as the absolute distance from the theoretical center of the indentation, (x_{tc}, y_{tc}), to the center of the actual fitted circles, (xc_{fit}, yc_{fit}). The eccentricity of the fitted ellipse was defined as the distance from the indentation's theoretical center to the center of the fitted ellipses (xe_{fit}, ye_{fit}):

$$Sc_{xy} = \sqrt{(xc_{fit} - x_{tc})^2 + (yc_{fit} - y_{tc})^2}. \tag{3.4}$$

For any given closed contour, the *fitting quality*, CC, was defined as the distance from the data points to the center of its corresponding fitted circle; in a sense this is equivalent to the error on fitting those points as a radial square deviation. The expression used to

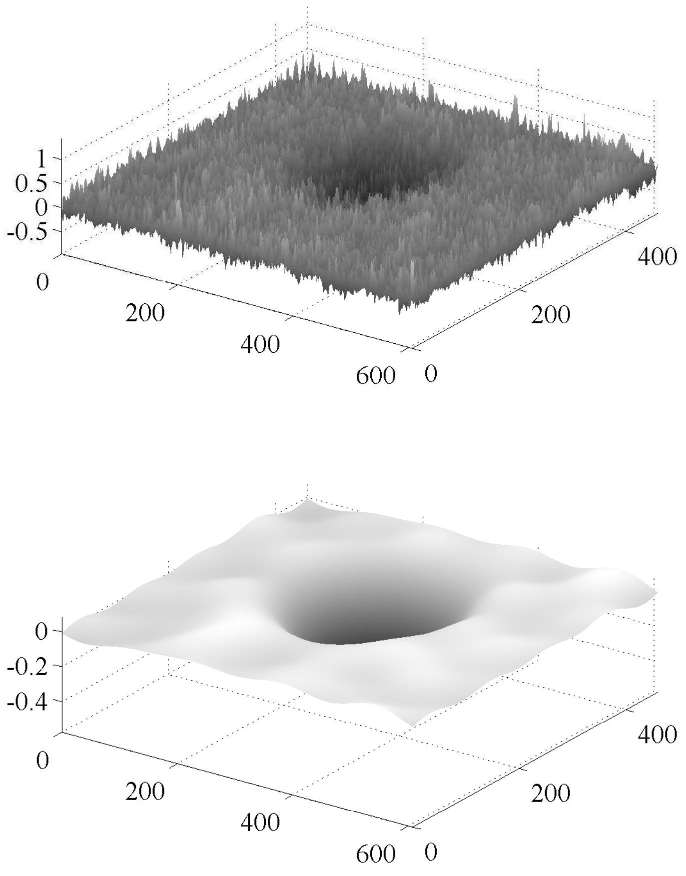

Figure 3.19: Typical surface indentation resulting from the first two filtering stages (top), and the corresponding low-pass filtered surface (bottom). Event number 1027

estimate this parameter is given by:

$$CC = \frac{1}{N}\sum_{i=1}^{N}\sqrt{|r_{fit}^2 - (x_i - x_{tc})^2 + (y_i - y_{tc})^2|}. \tag{3.5}$$

The third parameter, the *theoretical radius* r_t, was used to constrain the domain of the analyzed data, and also to estimate both the minimum and maximum values of the fitted radius. Based on the measured indentation depth, H, and the geometry of the idealized indentation shown in Figure 3.9, the expression for r_t is given by:

$$r_t = \sqrt{H^2 - 2\ d_p\ H}. \tag{3.6}$$

The parameters mentioned above were carefully monitored for each indentation measurement. Following the analysis of the previous example (event 1027) Figure 3.20 shows, on the right panel, the raw image obtained using the optical profilometer; the corresponding fitted circle is superimposed as well. On the left panel, the $2D$ contour lines used for the analysis and the fitted circle and ellipse are plotted. The corresponding $3D$ image and the best-fitted contour are shown in Figure 3.21. For this particular example, the measured crater diameter was $d_c = 260.22\ \mu$m. Experiments reported previously by Clark (1995) used optical microscope techniques to measure the indentations' diameters, by taking the mean of two diameters at right angles without looking at the circularity of the craters. Adding the third component, the depth, improves the quality of the measurements. Without losing the indentation's shape, the indentation parameters could be measured confidently within the surface roughness range, i.e., indentation parameters on the order of the surface roughness are not very reliable. The fitting quality was used to determine the error generated on estimating the crater diameter.

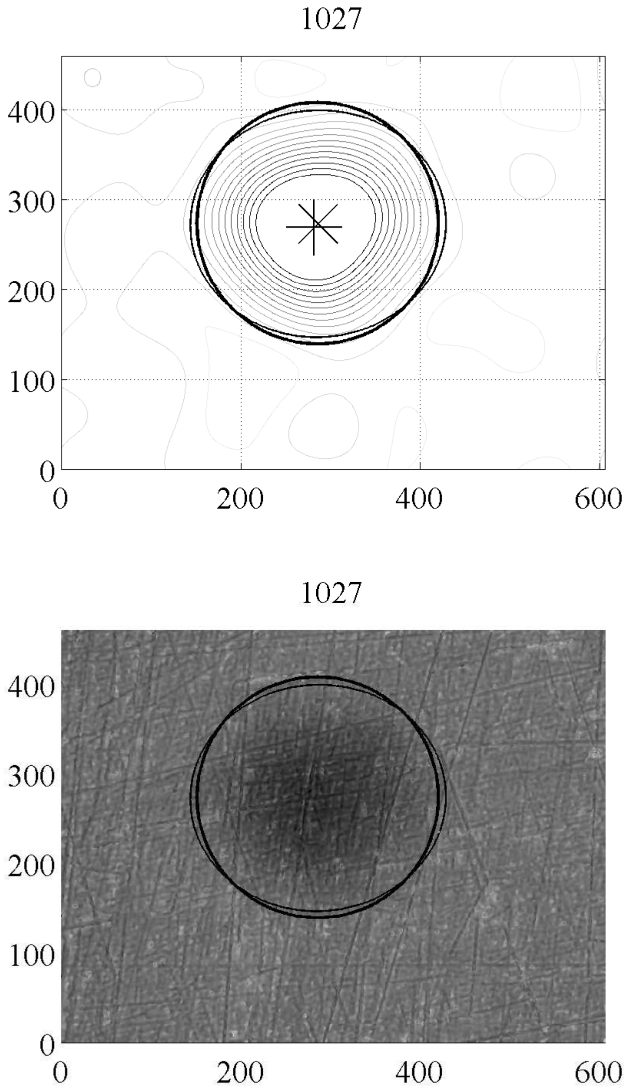

Figure 3.20: Typical original image of the indentation (bottom) and the 2D contours (top) corresponding to event number 1027. The measured crater diameter, represented by the superimposed circle, was $d_c = 260.22\ \mu$ m.

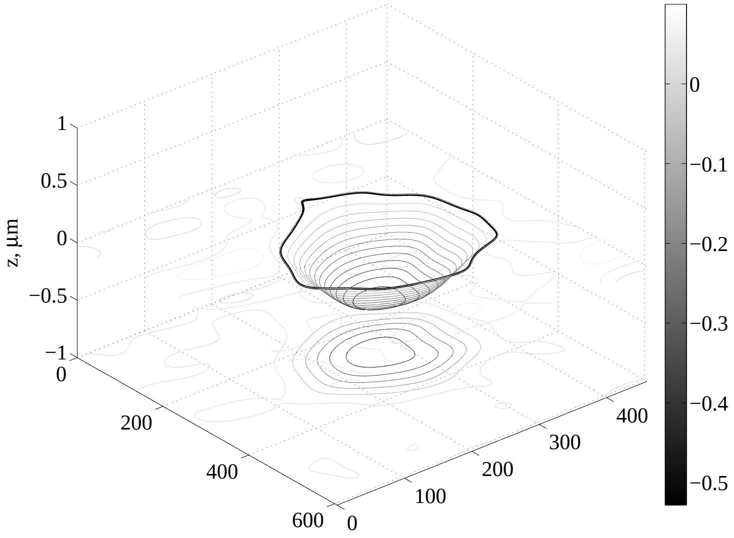

Figure 3.21: 3D contours and their respective $x - y$ projection for the indentation corresponding to event number 1027. The thick black line represents the best-fitted contour.

3.5.2 Indentation depth, H

For most of the cases the first approximation for the center of the crater did not coincide with the measured center, $Sc_{xy} \neq 0$. Hence, the *final* indentation depth, H, was defined as the depth located at the center of the final fitted circle, $H = z(xc_{fit}, yc_{fit})$. The error between the first approximation depth and the real depth was not as dramatic as the difference between the theoretical radius (Equation 3.6) and the real radius. For the example shown in Figure 3.20, the ratio of measured to theoretical indentation depth values was: $H/H_t = 0.99$ with a ratio of crater diameter to expected diameter of $d_c/2r_t = 1.59$. The contour selected to fit the crater diameter was slightly less than the zero, $CL = -0.05$ μm. The corresponding final indentation depth was $H = -0.58$ μm.

3.6 Discussion

The typical experimental techniques for particle-wall collisions were extended, allowing the surface of the wall to deform plastically. Due to the non-reversibility of the deformations, each experiment was done on a newly prepared sample. In addition to the image processing required to track the position of the particle over time, the 3D profiles of the indentations were measured. The range of impact velocities used in this work produced small indentations; some of them on the order of the surface roughness. By low-pass filtering the raw data, the effects of the surface roughness and, if present, the waviness were removed. For relatively large deformations, the surface roughness was negligible compared to the size of the indentation.

Chapter 4

Coefficient of restitution

The coefficient of restitution represents, in a very general way, the energy losses during a collision. This section shows the experimental results for dry collisions, where the surrounding fluid is air, and for collisions submerged in various viscous fluids. The collisions occur within the elastic-plastic regime. Therefore, for dry collisions, it is expected that the coefficient of restitution decreases as the impact velocity increases. When the viscous effects are important, the coefficient of restitution has a complex behavior which is combined with the losses due to plastic deformation. This section presents the experimental results on the coefficient of restitution for both cases.

4.1 Dry coefficient of restitution

As described in Section 1, for dry collisions at sufficiently low impact velocities ($U_i < U_{el}$) the resulting deformation is elastic and, in theory, $e = 1$. Beyond the elastic limit, yield begins causing the coefficient of restitution to gradually decrease with increasing severity of impact. Johnson carried out an analysis to estimate the coefficient of restitution resulting from a rigid particle impacting a soft half-space. Considering the rebound to be elastic, the kinetic energy of the rebound can be calculated from the size of the indentation, which is a function of the *dynamic pressure*, p_d. The expression for the coefficient of restitution is given by

$$e_J = K_J \sqrt{\frac{p_d}{E^*}} \left(\frac{\rho_p U_i^2}{p_d} \right)^{-1/8} \tag{4.1}$$

where $K_J = \sqrt{(3/2)^{1/2}\, 6^{3/4} \pi/5} \approx 1.718$.

Figure 4.1 shows the coefficient of restitution for steel particles impinging on blocks

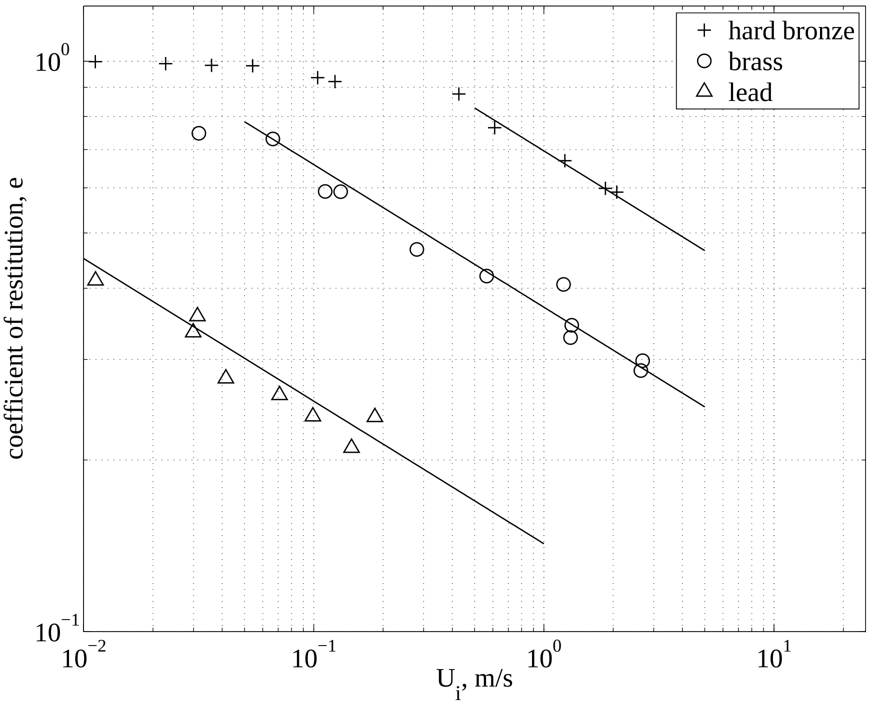

Figure 4.1: Measurements of the coefficient of restitution of a steel ball on blocks of different materials. The experimental data was taken from Goldsmith (1960). The solid lines represent the predicted decay of $e \sim O(U_i)^{-1/4}$.

of different materials. This experimental work was previously completed by Goldsmith (1960). Unfortunately, estimating the coefficient of restitution based on Equation 4.1 from this work is not possible, due to the lack of detailed information on the materials used during those experiments. For the materials used in Goldsmith (1960) the elastic properties varied widely.

The model proposed by Johnson (1985), and the experiments carried out by Goldsmith (1960), neglect the influence of the surrounding fluid; the experiments reported were dry collisions. Since the impact velocities used for those experiments are on the same order of magnitude as the experiments reported in this thesis, in Figure 4.2 the corresponding set of dry collisions for the three different alloys are presented. As mentioned by Johnson, the typical $e \sim U_i^{-1/4}$ is valid only for fully plastic collisions. Under those conditions, the dynamic pressure, p_d, is constant, $p_d/Y \approx 2.8$. However, between the elastic and the fully plastic regime, the dynamic pressure is $1.1 < p_d/Y < 2.8$. The compliance relationship for an elastic-pastic contact is not precisely defined. For the three different alloys, Figure 4.2 suggests that the beginning of the fully plastic regime was reached only for the alloys 6061 (□) and 2024 ($*$), but not for 7075 (□). The lines of slope $-1/4$ seemed to fit well with the experiments.

Prior to the theoretical model proposed by Johnson, in a more empirical manner Tabor (1951) estimated the coefficient of restitution based on an energy balance. By assuming that the energy of plastic deformation is proportional to the residual volume of the indentation after rebound, the implicit expression proposed by Tabor in terms of the coefficient of restitution, e_{Ta}, is given by

$$\frac{e_{Ta}}{\left(1-\beta\, e_{Ta}^2\right)^{\beta}} = \frac{1}{1-\beta}\left(\frac{U_i}{U_{el}}\right)^{2\beta-1} \tag{4.2}$$

where $\beta = (2n-1)/(4n+1)$ is a constant related to the Meyer index, n. The Meyer index varies between values of 2 for a perfectly plastic metal, and 2.5 for an annealed metal. The perfectly elastic contact can be recovered by using $n = 3$, which yields $e = 1$.

More recently, studies on contact mechanics and coefficients of restitution were undertaken by Thornton (1997), who found an analytical solution for the normal coefficient of restitution

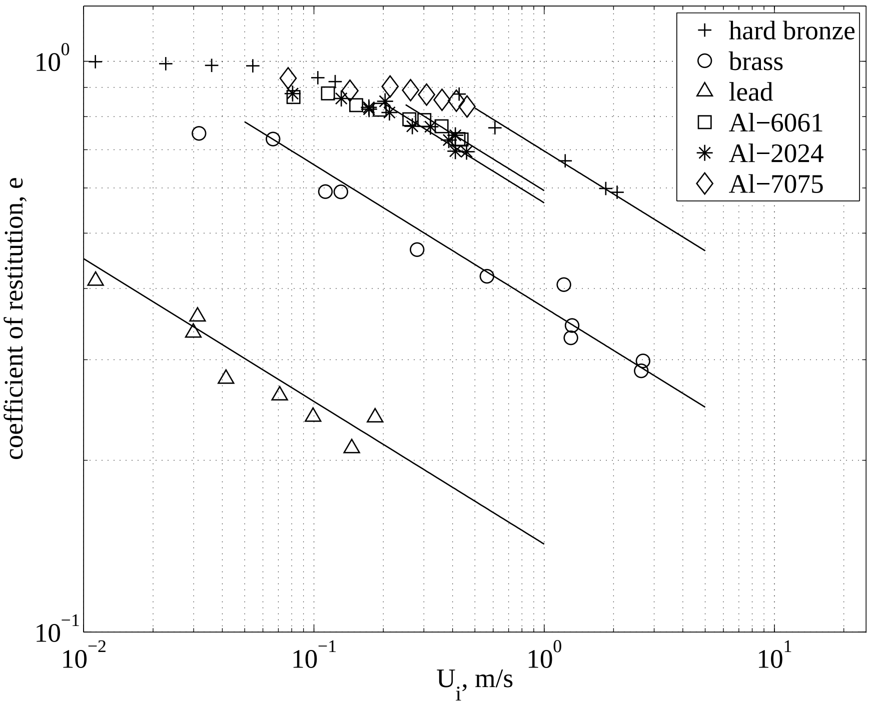

Figure 4.2: Comparison between the experimental results of Goldsmith (1960) and the normal collision of a steel particle in air on the three different alloys. The solid lines (–) correspond to a power-law regression fit, forcing the predicted decay of $e \sim O(U_i)^{-1/4}$.

for elastic-plastic spheres. The expression, which is velocity dependent, is given by

$$e_{Th} = \sqrt{\frac{6\sqrt{3}}{5}}\sqrt{1-\frac{1}{6}\left(\frac{U_Y}{U_i}\right)^2}\left[\frac{\frac{U_Y}{U_i}}{\frac{U_Y}{U_i}+2\sqrt{\frac{6}{5}-\frac{1}{5}\left(\frac{U_Y}{U_i}\right)^2}}\right]^{1/4} \tag{4.3}$$

where U_Y is the relative impact velocity below which the collisional interaction is assumed to be elastic. In evaluating this model, $U_Y = U_{el}$.

All of the models discussed above (Johnson, Tabor, Thornton) rely on a dynamic coefficient to describe the elastic-plastic regime, which does not yet have a constitutive relation describing the variations on the coefficient of restitution due to the impact. The comparison of the three aforementioned models, with the experimental data for dry collisions, is shown in Figure 4.3. For the model proposed by Johnson, $pd = 1.1\sigma_Y$. In Tabor's model, $n = 2$. Thornton suggested that U_{el} might vary as U_i increases. In general, for $U_i/U_Y >> 1$, the collision is fully plastic. In that case, U_{el} is no longer a suitable parameter for evaluating the coefficient of restitution. Instead, the *fully plastic velocity*, U_{Yp}, the velocity at which the deformation is fully plastic, is used. This velocity can be estimated with a slight modification in Equation 1.12. The main variation consists on replacing $\sigma_el = 1.65Y$, which is the limit of elasticity, with $\sigma_{el} = 2.8Y$, the beginning of the fully plastic regime. In the fully plastic regime, the characteristic velocity U_{Yp} remains invariant.

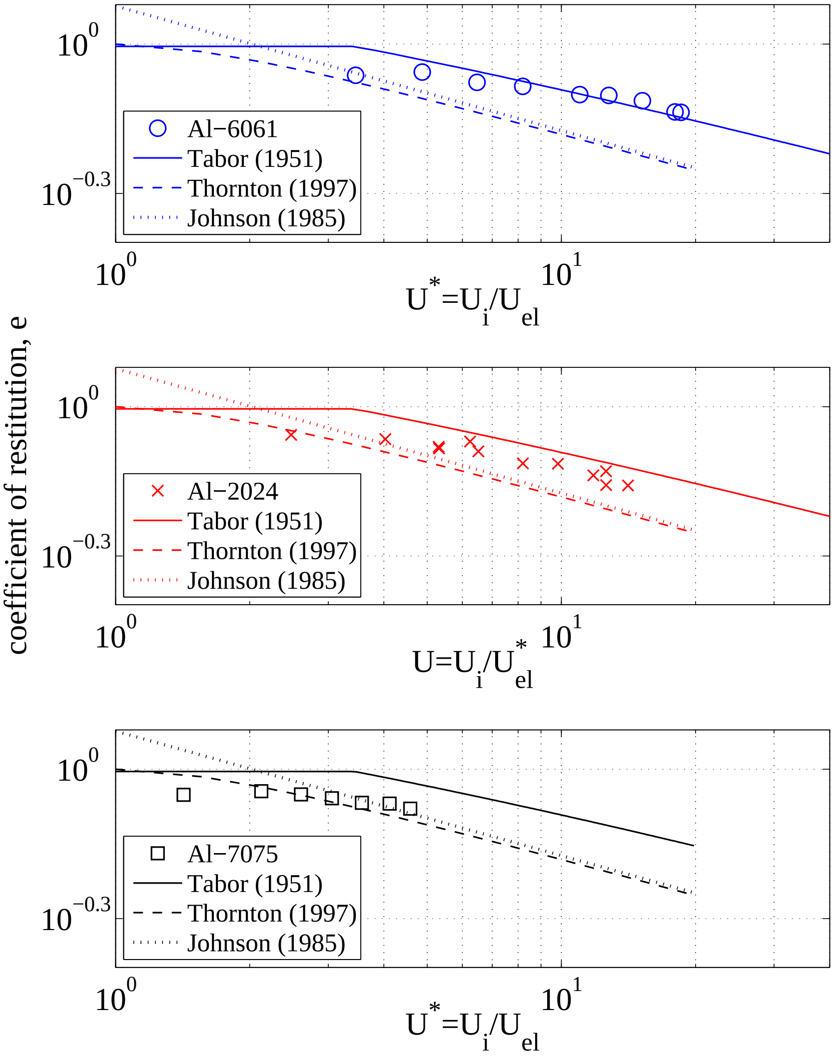

Figure 4.3: Comparison between the models proposed by Tabor (1951) (—), Thornton (1997) (- - -), and Johnson (1985) (· · ·), and the experiments for the three different alloys

4.1.1 Force Sensor

Within the same range of velocities, single particle collisions using the pressure bar with an embedded quartz crystal transducer are presented. The deformable surfaced used for those experiments were samples of aluminum alloy 6061 and the same particles used for the previous experiments was used. The impact and rebound velocities were estimated as before. However, adding the sensor modified the response of the bar to the collision. The coefficient of restitution was significantly reduced. Only the impact velocity was used to characterize the collision forces. It was assumed that the rebound velocity behaved just as the previous experiments, where the bar had no additional discontinuities (See Section4). Figure 4.5 shows the contact force measured for few samples. The experiments are compared with the Hertzian prediction of the contact Force. The collisions showed remained within the elastic-plastic regime. As the impact velocity increases, the equivalent load increases causing the plastic strain to be more dominant.

During the elastic-plastic regime, the collision time seems to remained unchanged respect to the predictions using Hertzian contact theory. The collision time for the experiments is shown in Figure 4.6.

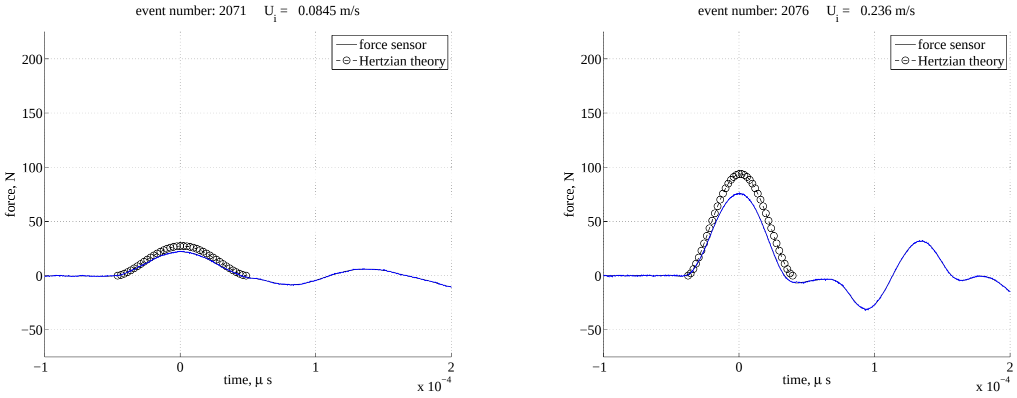

(a) Steel on Al-6061, $U_i = 0.085$ m/s (b) Steel on Al-6061, $U_i = 0.236$ m/s

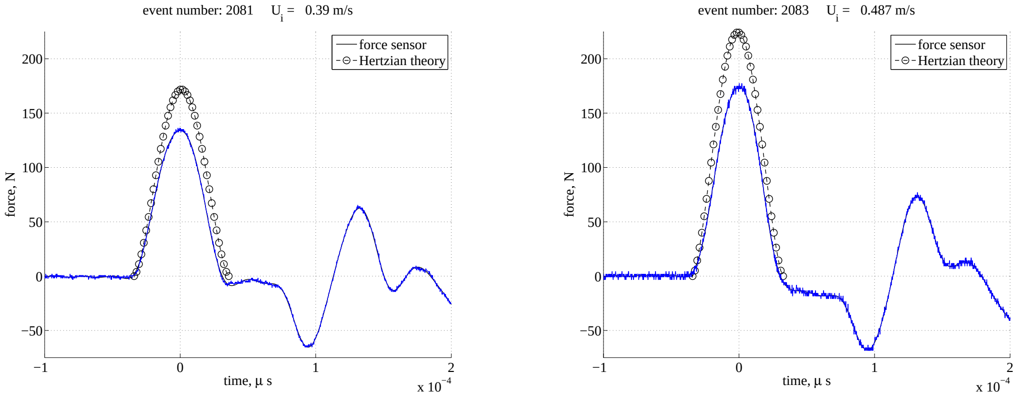

(c) Steel on Al-6061, $U_i = 0.390$ m/s (d) Steel on Al-6061, $U_i = 0.487$ m/s

Figure 4.4: Typical force-time plots generated by a stainless-steel particle on aluminum alloy 6061 at various velocities. The measurements were done on air.

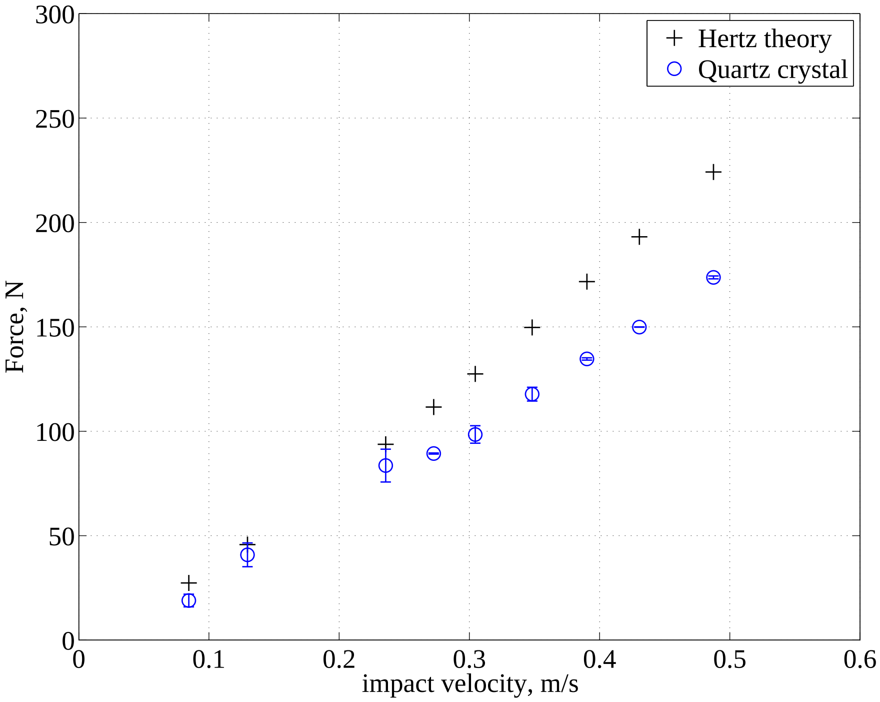

Figure 4.5: Contact force as a function of the impact velocity, U_i. The experiments are compared with the Hertzian theory. All of the collisions showed permanent deformations.

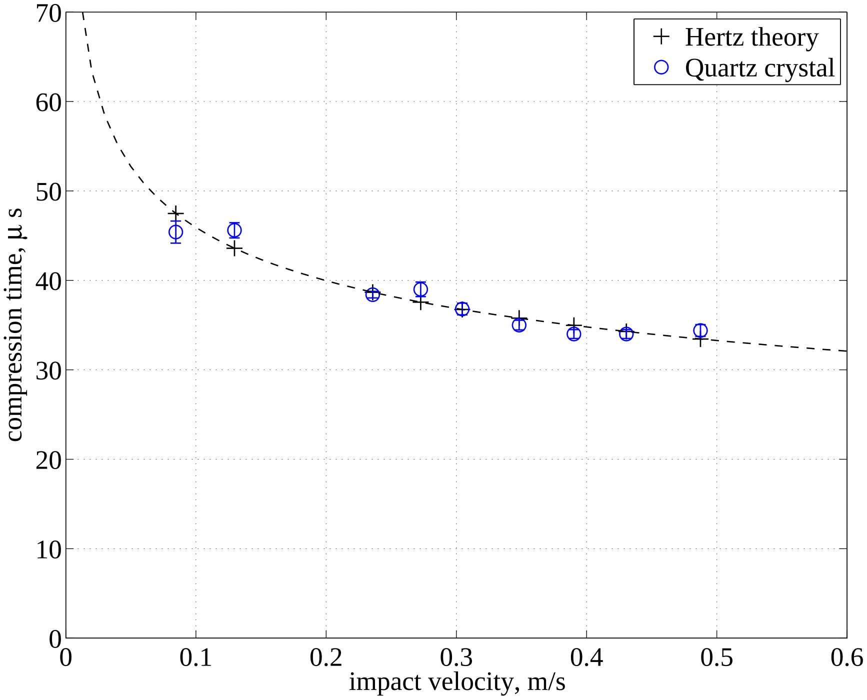

Figure 4.6: Contact time as a function of the impact velocity, U_i. The experiments are compared with the Hertzian theory. All of the collisions showed permanent deformations.

4.1.2 Discussion

The results presented correspond to dry collisions, where the coefficient of restitution decreases monotonically with the impact velocity due to plastic deformation on the surfaces. Those results were compared with models that predict the decay on the coefficient of restitution as a function of the impact velocity. Figure 4.3 shows, for each alloy, the coefficient of restitution as a function of U^*. As mentioned before, the elastic-plastic regime is not well defined within a dynamic process. The dynamic pressure, p_d, might vary with the impact velocity, which in a sense represents the load applied at the contact area.

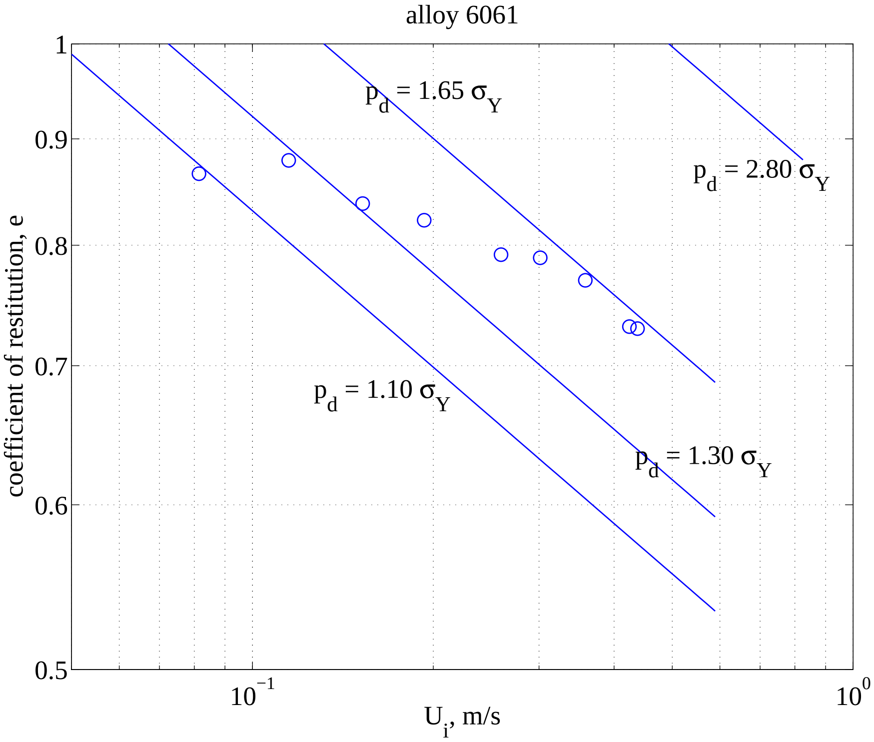

Figure 4.7: Johnson's model compared with the alloy 6061 experiments (∘). The solid lines (–) were estimated based on Equation 4.1 for different values of p_d.

Figure 4.7 shows, only for the alloy 6061, the coefficient of restitution as a function of the impact velocity. The solid lines were obtained using Johnson's model, each line was estimated by choosing different values of p_d, showing that, by varying the impact velocity, the data points intersect lines with different values of p_d, suggesting that for a dynamic process, p_d is a function of U_i. This behavior was observed as well for the other two models when comparing the data points. Thornton emphasized that the characteristic velocity U_{el} might not be a suitable parameter during the entire elastic-plastic regime. The model proposed by Tabor is based on the Meyer's index, which is an "adjustable" parameter. Kharaz and Gorham (2000) found values of the Meyer index by best fitting their experimental data points to Tabor's theory.

So far, the upper and lower limit of the elastic-plastic regime are well defined. However, within this regime, the commonly used models require adjustable parameters to describe the variations on the coefficient of restitution as a function of the impact velocity.

4.2 Hydrodynamic effects on the coefficient of restitution

The hydrodynamic effects in particle interactions, specifically particle-wall collisions, are dominated by the viscosity of the surrounding liquid. As the particle approaches the wall it experiences, in some cases, a deceleration due to the energy consumed in displacing the fluid between the particle and the wall. Experimental results for particle-wall collisions with hydrodynamic effects (McLaughlin (1968), Zenit and Hunt (1998), Joseph et al. (2001), Gondret et al. (2002)) in the absence of plastic deformations reported a critical Stokes number, St_c, below which the viscous effects completely dominate, resulting in a coefficient of restitution of 0. Beyond that critical value, the coefficient or restitution increases as the Stokes number increases. The coefficient of restitution for elastic collisions, asymptotically, reaches a value close to 1.

Figure 4.8 shows the experimental results (Joseph (2003)) for the coefficient of restitution

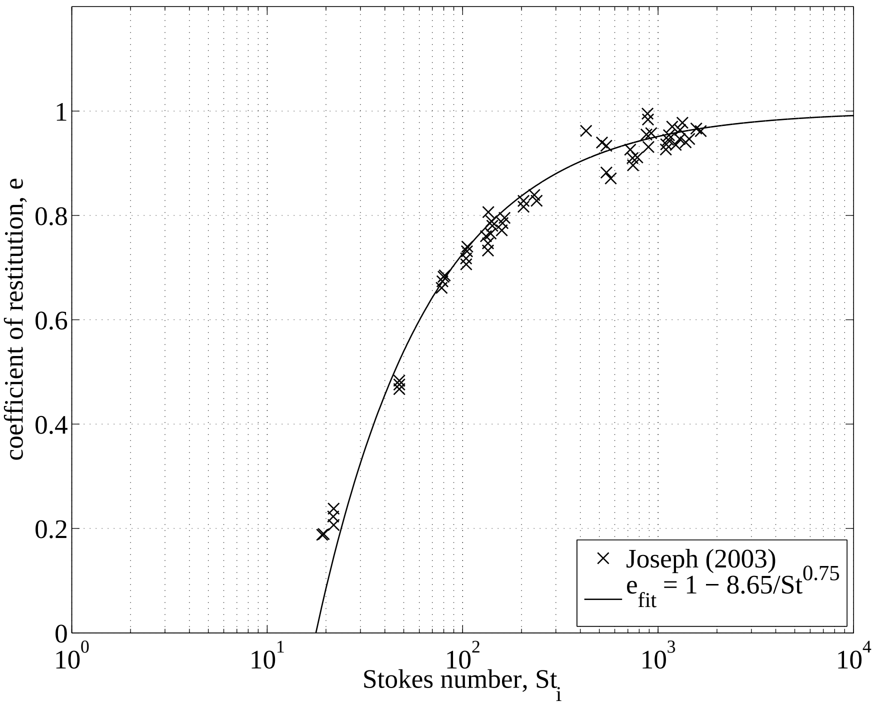

Figure 4.8: Coefficient of restitution, e, as a function of the Stokes number, St_i, for steel particles on a Zerodur wall. The solid line is the best fit of the data points. The results were obtained from Joseph (2003).

for stainless steel particles on the Zerodur wall in glycerol-water mixtures as a function of the Stokes number based on the impact velocity, St_i. As mentioned before, for $St_i > 10^3$, $e \approx 1$. In this figure, the solid line (—) corresponds to the best fit to the experimental data points; this line diverges from the simplified model $e = 1 - St_c/St$. The best fit to the points is: $e_{fit} = 1 - 8.65/St^{0.75}$. Extrapolating from this curve yields the critical Stokes number $St_c \approx 18$. This curve will be used as a reference for the elastic collisions, corresponding to the greatest possible value for the coefficient of restitution.

This section presents the results for the coefficient of restitution as a function of two parameters: the impact velocity nondimensionalized by the elastic velocity, and the Stokes number, based on the impact velocity. The results are sorted by type of alloy.

Figure 4.9 shows the coefficient of restitution as a function of U^*. The symbols represent the different liquids used for each set of experiments. For collision in air, the minimum coefficient of restitution measured was $e = 0.88 \pm 0.01$ with $U^* = 4.87$; this specific collision produced a permanent indentation on the sample, which accounts for the deviation of the coefficient of restitution from the elastic value, $e \approx 1$. The value of the coefficient of restitution dropped with the increase in viscosity of the surrounding liquid, i.e., for a given U^*, the coefficient of restitution increased as the viscosity decreased. Moreover, the decaying rate of the coefficient of restitution seemed to slow down as the viscosity increased. Eventually, this rate is reversed for the high viscosity fluids. Instead of gradually decaying, the coefficient of restitution gradually increased up to what appears to be a maximum value.

4.2.1 Alloy 6061

As shown in Figure 4.9, the results corresponding to the 62% glycerol ($\triangle$) experiments show a quick growth for the coefficient of restitution starting at $e \approx 0$ up to $e \approx 0.64$, where the coefficient of restitution remained constant, within experimental error, for the the interval of $6.00 < U^* < 13.16$. For this range of velocities, the samples experienced plastic deformation (see Section 5.1.1), suggesting that the initial kinetic energy is balanced with the energy loss due to plastic deformation viscous dissipation. Within this interval, as the impact velocity increased, the energy consumed by plastic deformation increased while the energy used to displace the fluid in between the particle and the wall decreased. This fortunate combination resulted in a constant coefficient of restitution, which only accounts for the overall energy budget regardless of the specific type of energy losses. If the impact

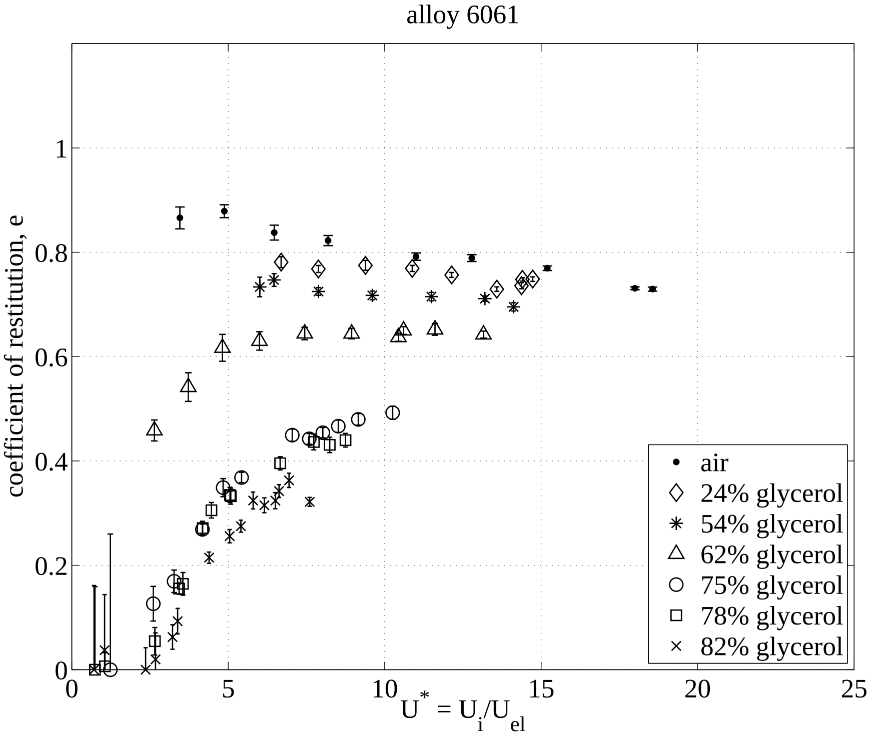

Figure 4.9: Alloy 6061: Coefficient of restitution, e, as a function of the nondimensionalized impact velocity, $U^* = U_i/U_{el}$

velocity were to further increase, the coefficient of restitution would have eventually dropped as the energy loss due to deformation begins to dominate. The limited range of velocities presented in this thesis did not cover regimes where the plastic deformation dominated over the hydrodynamic effects.

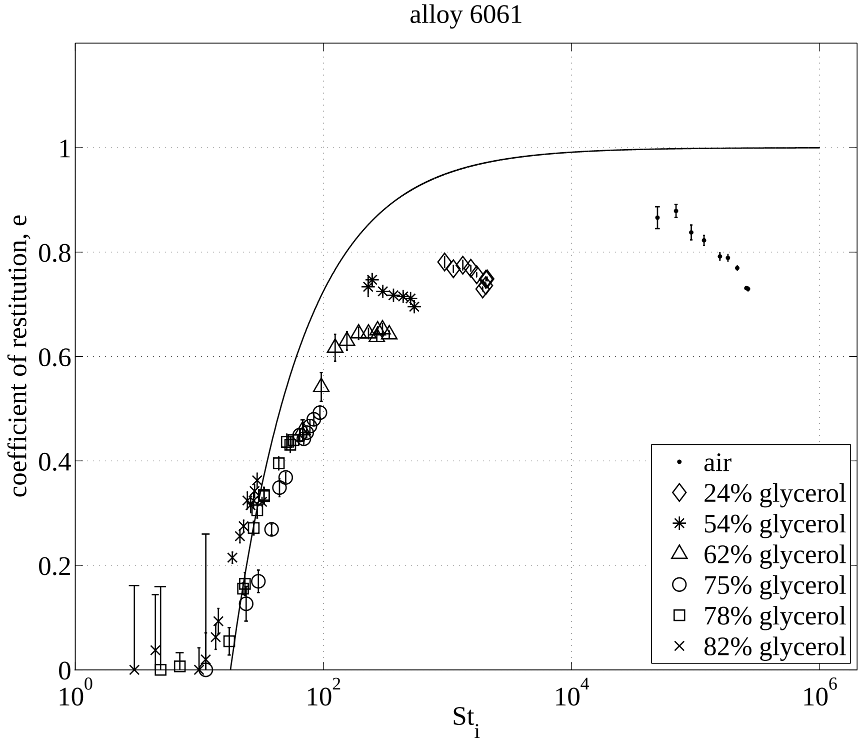

Figure 4.10: Alloy 6061: Coefficient of restitution, e, as a function of the Stokes number, St_i

For immersed elastic collisions, previous studies (Joseph et al. (2001)) have shown that the Stokes number is a suitable parameter to characterize the coefficient of restitution. However, the plastic deformation present in immersed elastic-plastic collisions consumes energy, yielding the Stokes insufficient to fully describe the system. Figure 4.10 shows the results of immersed collisions of steel particles on alloy 6061 with the curve fitted to the measurements done by Joseph (2003). The data compare well with the measurements at low Stokes numbers, where the collisions are either elastic or the deformations are small. The experiments begin to deviate from the solid line (—) at higher St, where the severity of the deformations increases. In this figure, the region of constant coefficient of restitution, corresponding to the 60% glycerol (△), is bounded between $154 < St_i < 340$.

4.2.2 Alloy 2024

The measured restitution coefficient of stainless steel particles impacting on samples of aluminum alloy 2024 as a function of the nondimensionalized impact velocity, U^*, is shown in Figure 4.11. For collisions in air, and the low glycerol-water concentrations (24% and 54%), the coefficient of restitution decreases as U^* increases. The decay rate of the coefficient of restitution with the impact velocity decreases as the viscous effects increase. The experiments completed with 62% glycerol (△) showed the same apparent constant coefficient of restitution reported for the alloy 6061. Within the interval $4.39 < U^* < 9.68$, the mean value of the coefficient of restitution is: $e = 0.64 \pm 0.01$. For this material, the maximum coefficient of restitution was $e = 0.88 \pm 0.01$ at $U^* = 2.48$. The elastic properties between the alloys 6061 and 2024 are comparable, therefore, the response of the materials to the collisions is also comparable.

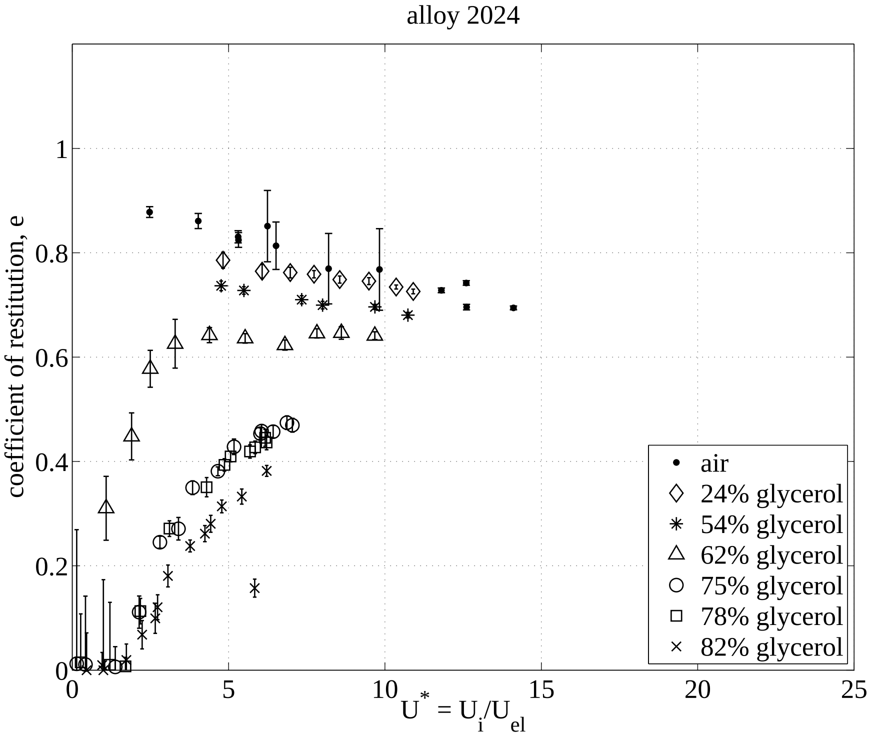

Figure 4.11: Alloy 2024: Coefficient of restitution, e, as a function of the nondimensionalized impact velocity, $U^* = U_i/U_{el}$

Figure 4.12 shows the coefficient of restitution as a function of the Stokes number. As a reference, the elastic limit is represented by the solid line (—). As mentioned before, the elastic limit is based on experimental data from collisions involving elastic materials, i.e., no plastic deformation took place. In this figure, the quasi-constant coefficient of restitution interval, corresponding to the 60% glycerol ($\triangle$), is bounded between $157 < St_i < 346$.

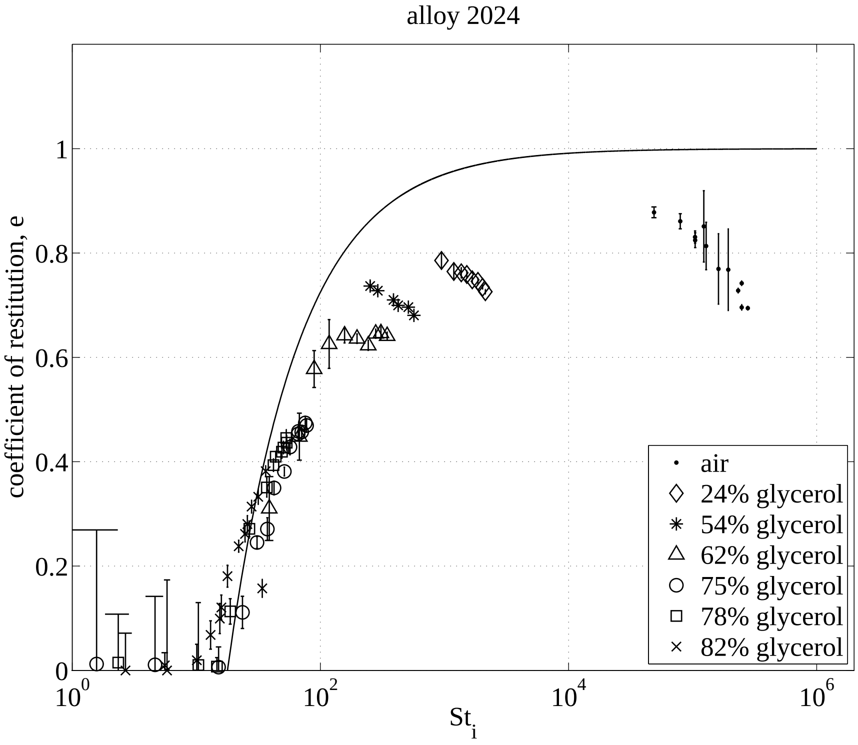

Figure 4.12: Alloy 2024: Coefficient of restitution, e, as a function of the Stokes number, St_i

4.2.3 Alloy 7075

Experiments were also performed using the alloy 7075, the hardest of the three alloys. The measured coefficients of restitution resulting from steel particles impinging on samples of this aluminum alloy are plotted as a function of U^*, as shown in Figure 4.13. The results show a maximum value in the coefficient of restitution of $e = 0.93 \pm 0.03$ at $U^* = 0.77$. The maximum value for the coefficient of restitution was slightly higher than for the other aluminum alloys, since according to the value of U^* plastic deformations were not reached. A possible explanation for the deviation from the elastic limit may be attributed to the intrinsic experimental errors.

The coefficient of restitution for this alloy presents two possible quasi-constant regions corresponding to the 62% ($\triangle$) and 54% ($*$) glycerol experiments. The apparent constant coefficient of restitution regime for the 62% glycerol ($\triangle$) has a value of $e = 0.71 \pm 0.02$, which spans over the range of $2.00 < U^* < 3.22$. The measured coefficient of restitution for the collisions in the aqueous solution of glycerol at 54% wt., remained, within the experimental error, constant between $1.57 < U* < 3.46$. Those collisions had an average value of $e = 0.81 \pm 0.01$. Compared to the two previous alloys, U^* is smaller for 7075 aluminum since the value of U_{el} is considerably larger.

Figure 4.14 shows the measured coefficient of restitution resulting from collisions of stainless steel particles impinging over samples of alloy 7075 as a function of St. The response of this particular alloy to the impacts is relatively close to the elastic limit, compared to the two previous alloys. Although the plateau on the coefficient of restitution seems to occur at two different concentrations of aqueous solution of glycerol (54% and 62%). The results suggests that, for "harder" materials, the balance between the energy of deformation and the hydrodynamic losses occurs at higher coefficient of restitution values. The energy lost due to viscous dissipation is approximately constant irrespective of the contacting materials. However, the energy required to cause plastic deformations is a function of σ_{el}, which for this alloy (7075) is considerably larger than the previous two alloys. Also, the plastic deformations are considerably smaller in magnitude than the deformations on softer materials.

The constant coefficient of restitution period occurs between $256 < St_i < 565$ and $208 < St_i < 335$ for the 54% ($*$) and the 62% ($\triangle$) glycerol solutions, respectively.

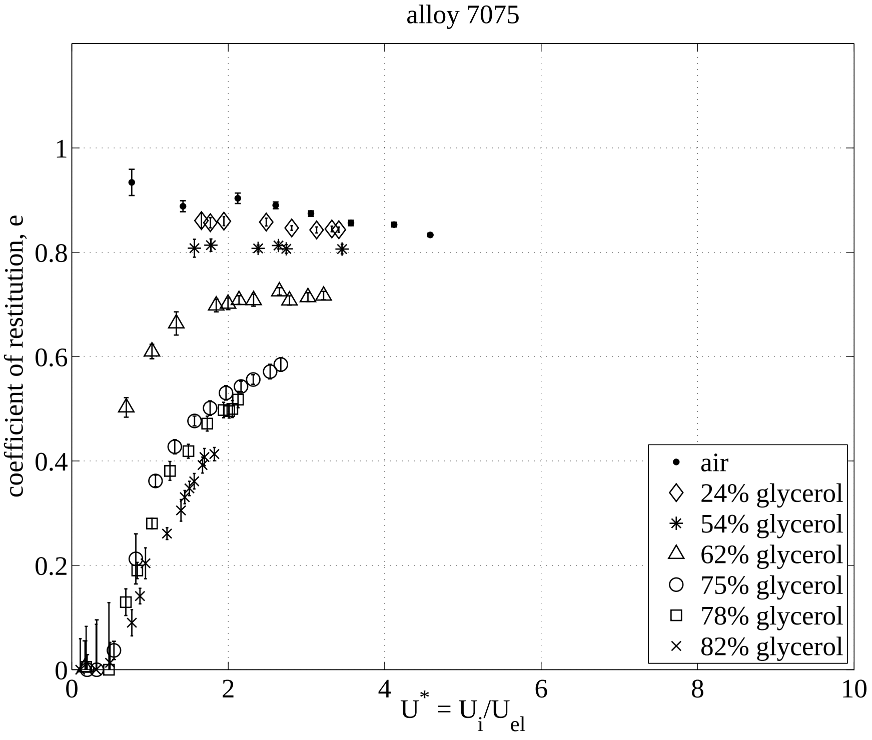

Figure 4.13: Alloy 7075: Coefficient of restitution, e, as a function of the nondimensionalized impact velocity, $U^* = U_i/U_{el}$

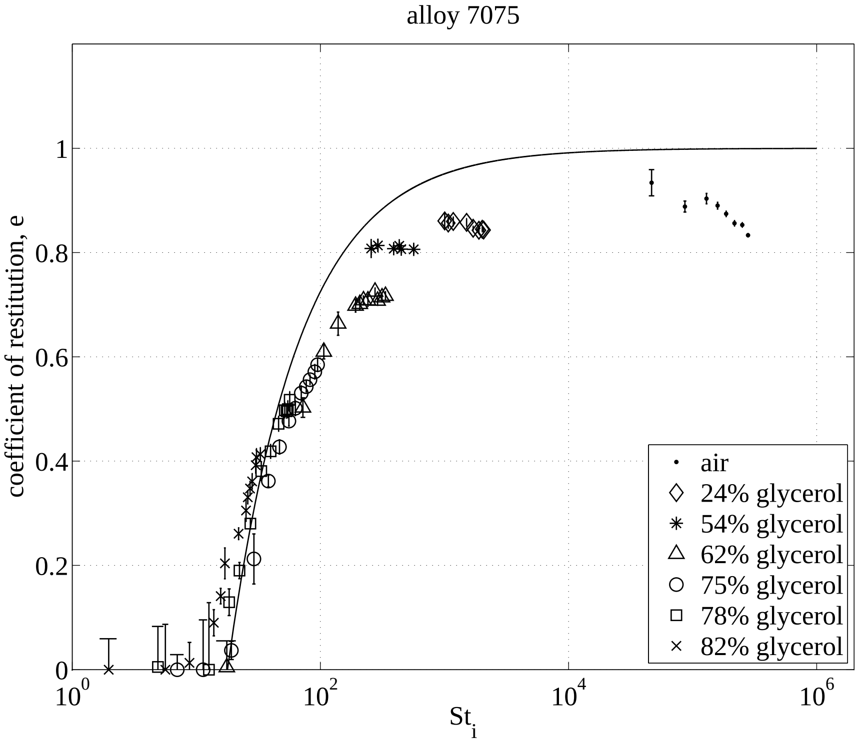

Figure 4.14: Alloy 7075: Coefficient of restitution, e, as a function of the Stokes number, St_i.

4.3 Discussion

Figure 4.3 shows the coefficient of restitution as a function of the Stokes number. This plot summarizes all the experiments for the three different alloys conducted for this thesis. The colors used to differentiate the alloys, are: blue — alloy 6061, red — alloy 2024, and black — 7075.

In terms of the coefficient of restitution, the elastic collisions are fully described as a function of the Stokes number. However, as shown in Figure 4.3, the plastic deformation introduces an extra energy loss mechanism that is not included in either of the two previous parameters. For low Stokes numbers, the collisions approximate the elastic regime dominated by the viscous effects. In the case of the experiments with alloy 7075, the coefficient of restitution increases monotonically with the Stokes number, closely following the elastic limit line (—). The other two alloys deviate from the line at a lower Stokes numbers. For the softer materials, the impact velocity reaches the elastic limit at lower Stokes number. The viscous effects are still dominating the collision process until the coefficient of restitution plateau, where the two dominant energy losses are balanced: the energy in plastic deformation and the viscous dissipation. Beyond this threshold, the coefficient of restitution is monotonically decreasing, since the plastic deformation dominates the energy budget. When plasticity occurs, the Stokes number is no longer a suitable parameter to describe the collisions, Each set of experiments branches out from the solid line since the energy balances differently for each combination of yield strength and liquid concentration. For example, in Figure 4.14 for $St \approx 250$ there are two possible values for the coefficient of restitution, those values are determined by the viscosity of the surrounding liquid.

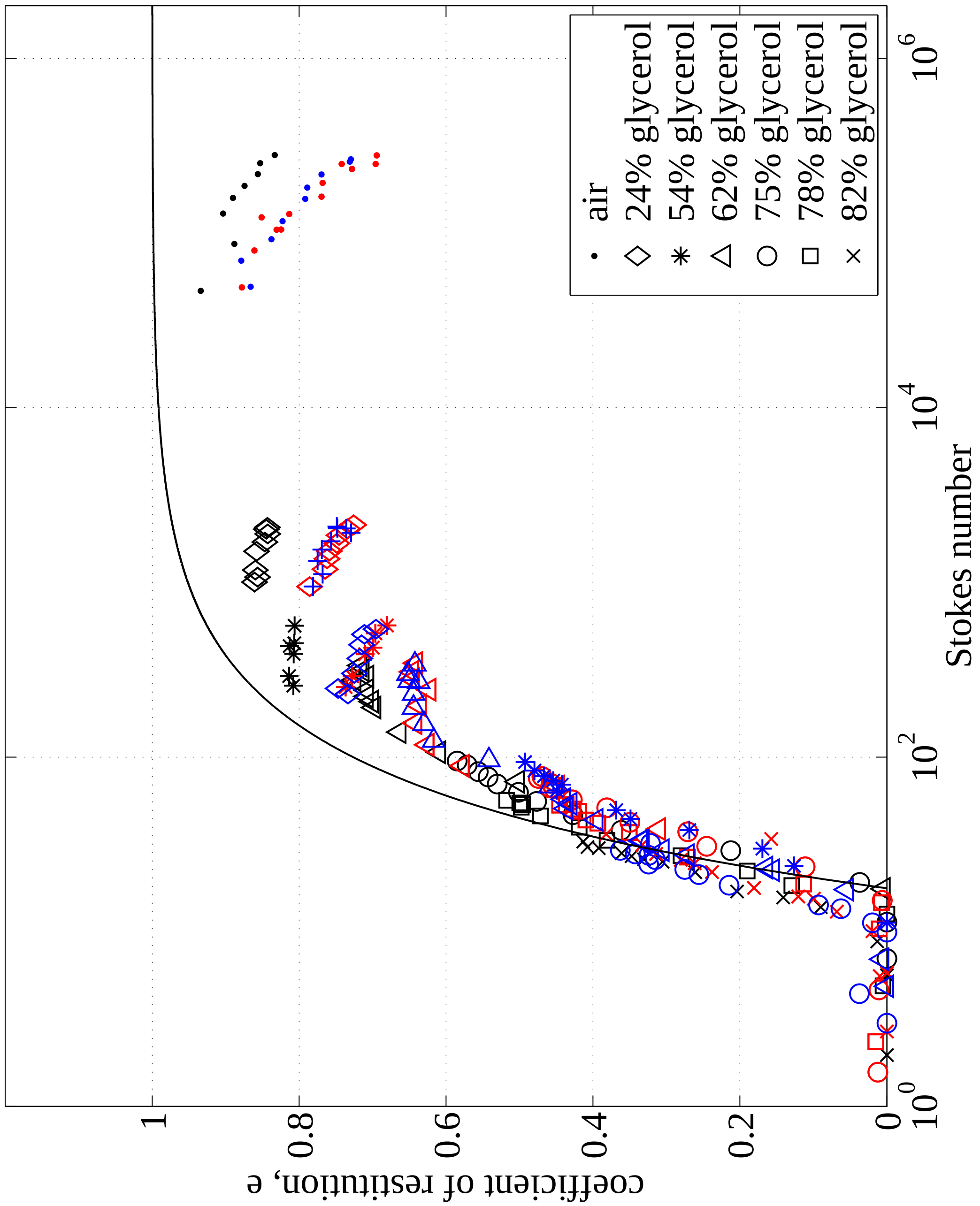

Figure 4.15: Coefficient of restitution, e, as a function of the Stokes number, St_i. The points in blue correspond to the alloy 6061, red — alloy 2024, and black — alloy 7075. The solid line (—) is the best fit to the experimental data from Joseph (2003), corresponding to the elastic limit.

Chapter 5

Elastic-plastic deformations

The result of a various number of experiments are presented in this section. The experiments were carried out using particles with the same properties impacting several targets. The results are presented in two different ways: the solid mechanics viewpoint, where the fluid effects are not considered; and the fluid mechanics perspective including the effect of the surrounding fluid through the impact Stokes number, St. As a result of the impact, some specimens showed permanent deformations on the surface. For those cases the typical indentation parameters are presented as the indentation depth, H, and the crater diameter, d_c. Combining the impact and rebound velocities, the coefficient of restitution, e, was estimated. The error bars for the indentation parameters were estimated from the misfit of the filtered contours to a circle for the d_c measurements, and by adding the surface roughness and the contour level at which the crater diameter was optimally fitted. The error bars on the coefficient of restitution represent the correlation between the estimated velocities and the data. For small Stokes numbers, the error bars are more pronounced since the fluid effects are larger, and the small changes of the particle position with time, close to the collision point, are on the order of the estimated velocities resulting in a poor correlation. The results are grouped according to the material properties of the target, tabulated in Table 2.2. Each experiment was performed on a new and pre-stressed free surface. After each experiment the specimen was replaced with a new one so that the targets had roughly the same initial conditions between experiments.

Table 5.1: Elastic quantities

Material	Alloy	Elastic velocity, U_{el} ($\mathrm{m\ s^{-1}}$)	Combined yield strain, Y/E^*
Aluminum	6061	0.024	0.0048
Aluminum	2024	0.033	0.0054
Aluminum	7075	0.101	0.0085
Ultra-Hard Wear-Resistant Stainless Steel	440C	4.631	0.0317

5.1 Solid mechanics perspective

This section summarizes the deformation parameters measured for the three different alloys used in this thesis. The idea behind this perspective is to present the results using the typical contact-mechanics argot, ignoring the hydrodynamic parameters. For all the plots presented below, the different symbols represent the surrounded liquids used in this work.

5.1.1 Al-6061

The following section presents the individual results for the most extensively studied material, which was the 6061 alloy. The impacting particles were stainless-steel spheres 12.7 mm in diameter (See Table 2.1). Figure 5.1 shows the crater diameter, d_c, nondimensionalized by the particle diameter, $D_p = 2R$, as a function of the normalized impact velocity, U^*, defined as the ratio of the particle impact velocity to the *elastic velocity.* Considering a Hertzian contact, the maximum elastic contact radius normalized with the particle radius can be calculated using Equation 1.14 the corresponding value is $r_e^*/R = 0.012$. For $U^* > 1$, plastic deformation is expected to occur. However, the maximum stress concentration occurs just below the surface; therefore, no "visible" permanent deformations are observed for $U^* = 1$. The first permanent indentation observed corresponds to $U^* \approx 4$, with $d_c/2R \approx 0.012$. This value is on the order of the value predicted by the Hertzian theory. The nondimensionalized crater diameter increases with the normalized impact velocity as $d_c/2R \sim O(\sqrt{U^*})$. Figure 5.2 presents the measurements of the indentation depth, H, nondimensionalized by the particle radius, R, as a function of U^*. The minimum permanent indentation observed

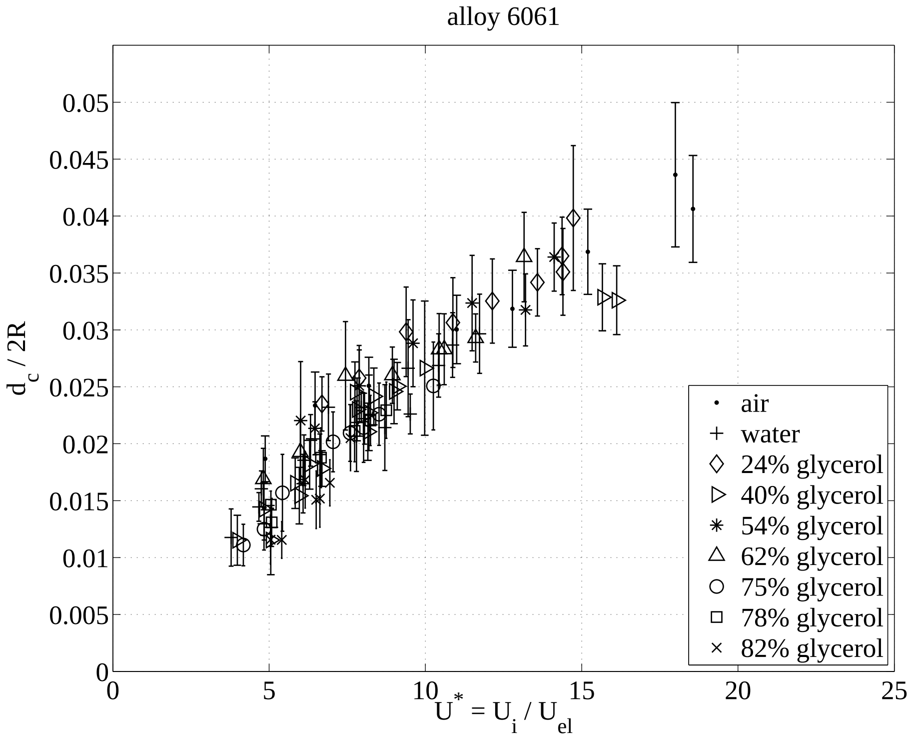

Figure 5.1: Crater diameter nondimensionalized by the particle diameter, $d_c/2R$, plotted as a function of the nondimensionalized impact velocity, $U^* = U_i/U_{el}$. The overall average surface roughness is $\sigma_s = 0.068 \pm 0.03\ \mu$ m.

corresponds to the same case as the minimum crater diameter reported. Hence, the indentation depth relative to to the particle radius is $H/R \approx 2.50 \times 10^{-5}$, at $U^* \approx 4$. On average, the lowest values of H are on the order of the surface roughness. For all the experiments done using the alloy 6061, the overall average surface roughness is $\sigma_s = 0.068 \pm 0.03$ μ m. Hence, $\sigma_s/R = 1.08 \pm 0.43 \times 10^{-5}$, which is on the order of magnitude of the minimum value of H/R. Typically, the measurements of the smallest deformations show very large scatter in the data. The maximum elastic penetration estimated from the Hertzian theory , $\delta_e^*/R = 1.55 \times 10^{-4}$, is large compared to the minimum indentation depth, suggesting that for small deformations, the elastic contribution to the total deformation is considerable. The data points corresponding to the experiments done in water (+) and 40% glycerol ($\triangleright$) presented in this section, are missing the corresponding measurements on the coefficient of restitution. Due to excessive blurriness on the images it was impossible to rely on the

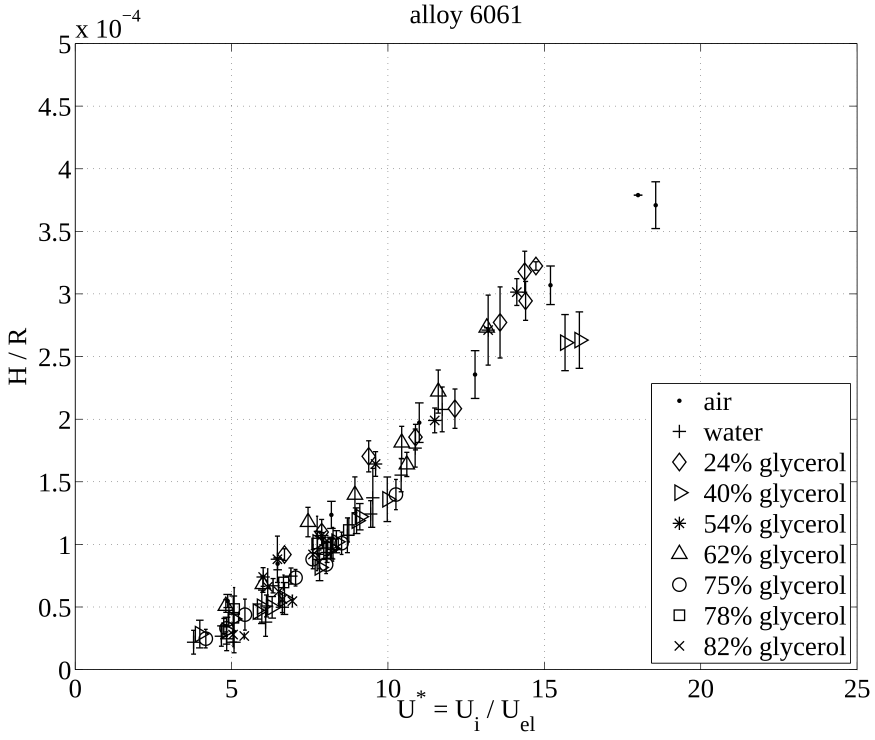

Figure 5.2: Indentation depth nondimensionalized by the particle radius, H/R, plotted as a function of the nondimensionalized impact velocity, $U^* = U_i/U_{el}$. The overall average surface roughness is $\sigma_s = 0.068 \pm 0.03$ μ m.

rebound velocity measurements. The impact velocity was estimated using several points before the contact, which is valid for large Stokes numbers, since the deceleration of the particle due to the presence of the wall was imperceptible. The indentation parameters were obtained using the typical procedure described in Section 3. In both Figures 5.2 and 5.1, there are two points corresponding to the 40% glycerol ($\triangle$) that exhibit a clear offset from the experimental trend, those two data points belong to the set of data that was obtained with the malfunctioning camera.

5.1.2 Al-2024

Figure 5.3 shows the crater diameters measured after stainless steel particles impacted several samples of alloy 2024. The crater diameters are nondimensionalized by the radii of the particles and they are plotted as a function of U^*. As expected, the permanent indentations are visible for $U* > 1$. The minimum value was measured at $U^* \approx 2.7$, with $d_c/2R \approx 0.011$. The overall average surface roughness of the samples in this set of experiments is: $\sigma_s = 0.054 \pm 0.019\ \mu m$. The maximum contact radius resulting from the elastic deformation, $r_e * /R = 0.014$, is again on the order of magnitude of the minimum value observed. The normalized crater diameter increases monotonically with U^* as $\sim O(\sqrt{U^*})$. The measured indentation depths, nondimensionalized by the radius of the impacting particle, are shown in Figure 5.4 as a function U^*, the normalized impact velocity. The minimum indentation depth occurs approximately at $U^* \approx 2.7$, with $H/R \approx 1.50 \times 10^{-5}$. The Hertzian prediction for the maximum normal displacement, estimated using Equation 1.13 is: $\delta_e^*/R = 1.97 \times 10^{-4}$.

5.1.3 Al-7075

In addition to the data presented using alloys 6061 and 2024, the alloy 7075 was also used. The elastic velocity for this alloy is relatively higher than for the previous alloys. In Figure 5.5, the nondimensionalized crater diameter formed as a result of the collisions is plotted as a function of U^*. Although the range of impact velocities, $11 < U_i < 500\ mm/s$ was the same for the three different alloys, the range of U^* for this alloy is reduced compared to the previous ones. As a result of increasing U_{el}, the tendency for a material to deform plastically decreases. The minimum crater was measured at $U^* \approx 1.8$, with $d_c/2R \approx 0.011$. The estimated maximum $r_e^*/R = 0.022$ is in this case slightly larger than the minimum value

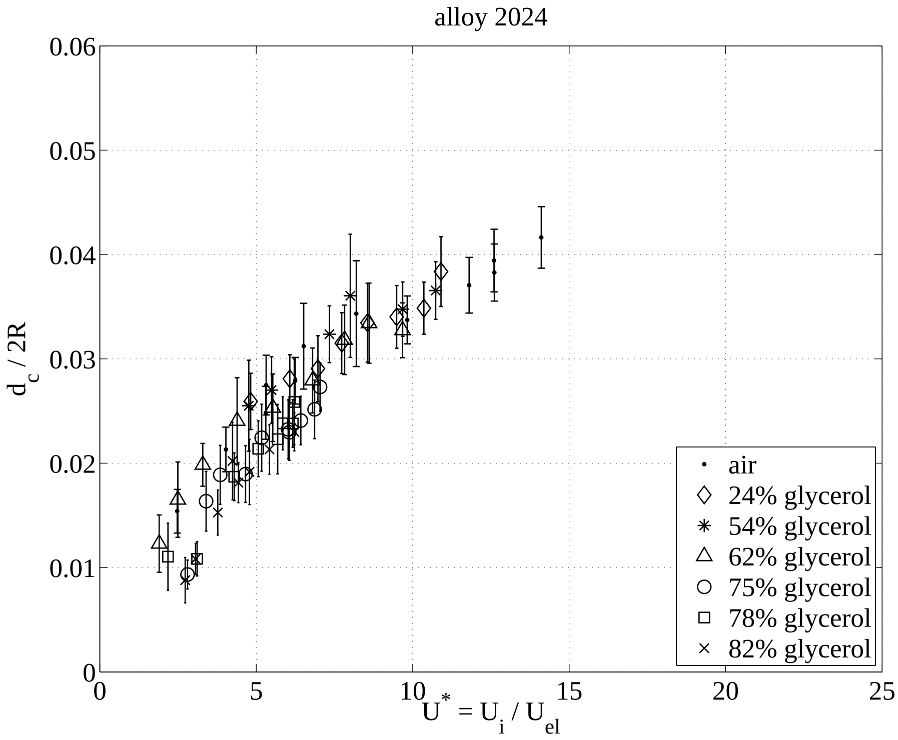

Figure 5.3: Crater diameter nondimensionalized by the particle diameter, $d_c/2R$, plotted as a function of the nondimensionalized impact velocity, $U^* = U_i/U_{el}$. The overall average surface roughness is $\sigma_s = 0.054 \pm 0.019\ \mu m$.

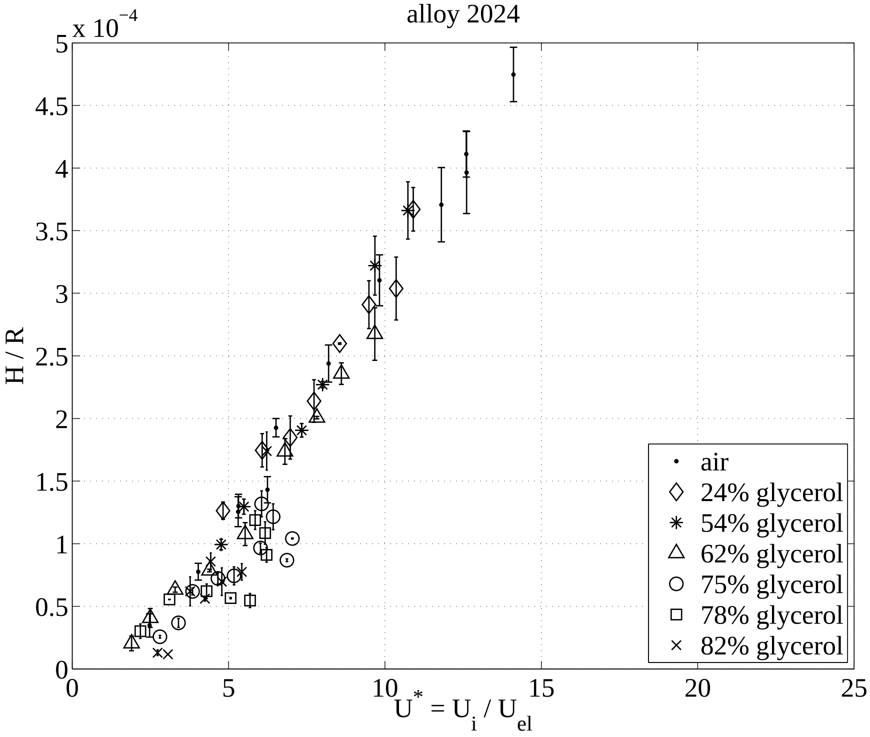

Figure 5.4: Indentation depth nondimensionalized by the particle radius, H/R, plotted as a function of the nondimensionalized impact velocity, $U^* = U_i/U_{el}$. The overall average surface roughness is $\sigma_s = 0.054 \pm 0.019$ μm.

measured. The corresponding nondimensionalized indentation depth is shown in Figure 5.6,

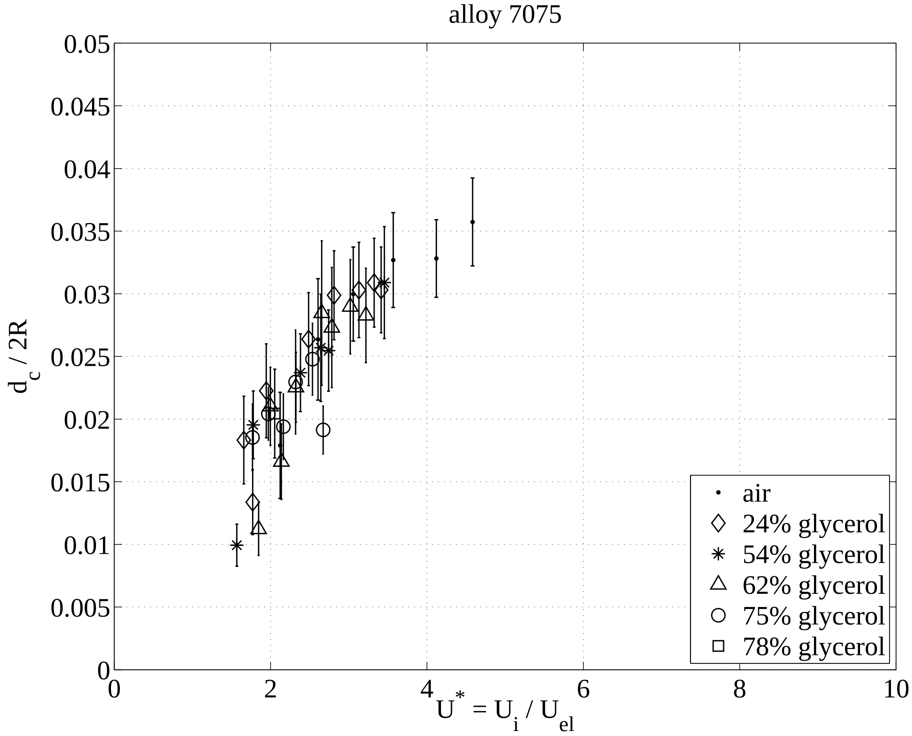

Figure 5.5: Crater diameter nondimensionalized by the particle diameter, $d_c/2R$, plotted as a function of the nondimensionalized impact velocity, $U^* = U_i/U_{el}$. The overall average surface roughness is $\sigma_s = 0.037 \pm 0.008$ μm.

plotted as a function of the normalized impact velocity. The minimum indentation depth was measured at $U^* \approx 1.8$, with $H/R \approx 1.4 \times 10^{-5}$. Again, in comparison with the estimated maximum elastic deformation, $\delta_e^*/R = 4.89 \times 10^{-4}$, the minimum depth measured is significantly smaller than the maximum elastic displacement. The nondimensionalized average surface roughness is $\sigma_s/R = 5.83 \pm 0.12 \times 10^{-6}$, which is smaller than the minimum value measured.

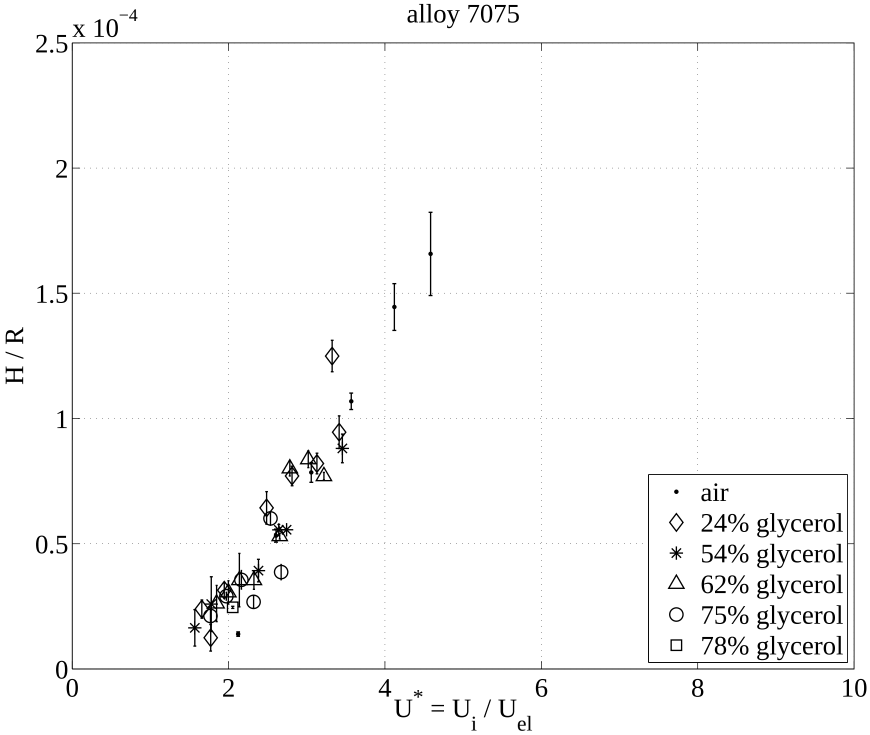

Figure 5.6: Indentation depth nondimensionalized by the particle radius, H/R, plotted as a function of the nondimensionalized impact velocity, $U^* = U_i/U_{el}$. The overall average surface roughness is $\sigma_s = 0.037 \pm 0.008\ \mu m$.

5.2 Discussion

For three different alloys used in this thesis, the indentation parameters were previously reported individually. The different symbols for those plots were used to distinguish, if existent, the variability of the deformations with the surrounding liquid. Within experimental uncertainty, the data show the deformations to be independent of the surrounding fluid. Figure 5.7 shows, for all the experiments, the dimensional indentation depths for the three different alloys as a function of the impact velocities, omitting the distinction of the surrounding liquids. The solid lines represent the best linear fit of the data points. As suggested by Bitter, the indentation depth increases linearly with the impact velocity. During the elastic deformation regime ($U_i < U_{el}$) the material response to the collisions, given by Equation 1.13 is also linear, for the combination of materials selected for this work.

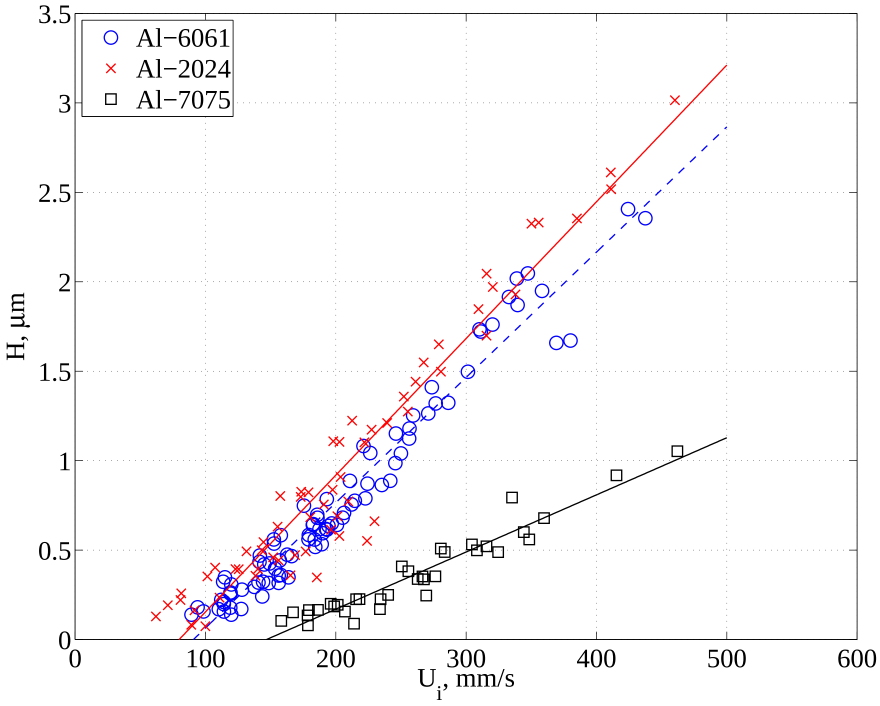

Figure 5.7: Indentation depth, H, as a function of the impact velocity, U_i

In addition to the indentation depth, the crater diameter resulting from the impacts is shown in Figure 5.8. The solid lines were estimated based the analysis done by Bitter.

The expression for the crater diameter was obtained by substituting $H \approx r_c^2/2R$ in Equation 1.26, where $r_c = d_c/2$. For alloys 2024 and 6061, almost no difference in the crater size was noticed from the measurements. However, the measurements of the crater diameter corresponding to the aluminum alloy 2024 appear to be slightly larger than the ones for the alloy 6061, which has the lowest yield strength (see Table 2.2). In Figure 5.8, the predicted crater sizes, based on the material properties, are as expected; for a given impact velocity, they are slightly larger for the Al — 6061 (blue - -), than for the Al — 2024 (red −). Those small differences can be observed from the model proposed by Bitter, but are less apparent in the experiments. The same misfit with the theory can be observed in Figure 5.7, where the indentation depth measurements corresponding to the Al — 2024 are, on average, slightly larger than the values measured for the Al — 6061. A possible explanation for this inconsistency can be attributed to the average values on the elastic properties of those materials. Often, the yield strength is an average value. If the difference between the values of yield strength provided by the manufacturer of the Al — 2024 and Al — 6061 is smaller than the standard deviation of the nominal values, then the expected response of those materials may appear to be contradictory, especially when looking at fine-scale differences on materials with similar elastic properties.

Figure 5.7, clearly shows the difference between Al — 7075 and the other two alloys. Typically, the indentation depth nondimensionalized by the particle radius is a representation of the localized strain, often called *interference*. In Figure 5.9, H/R is plotted as a function of U^*. As expected, the hardest of the three alloys, Al — 7075 requires a higher impact velocity to cause the same deformation as the other two alloys.

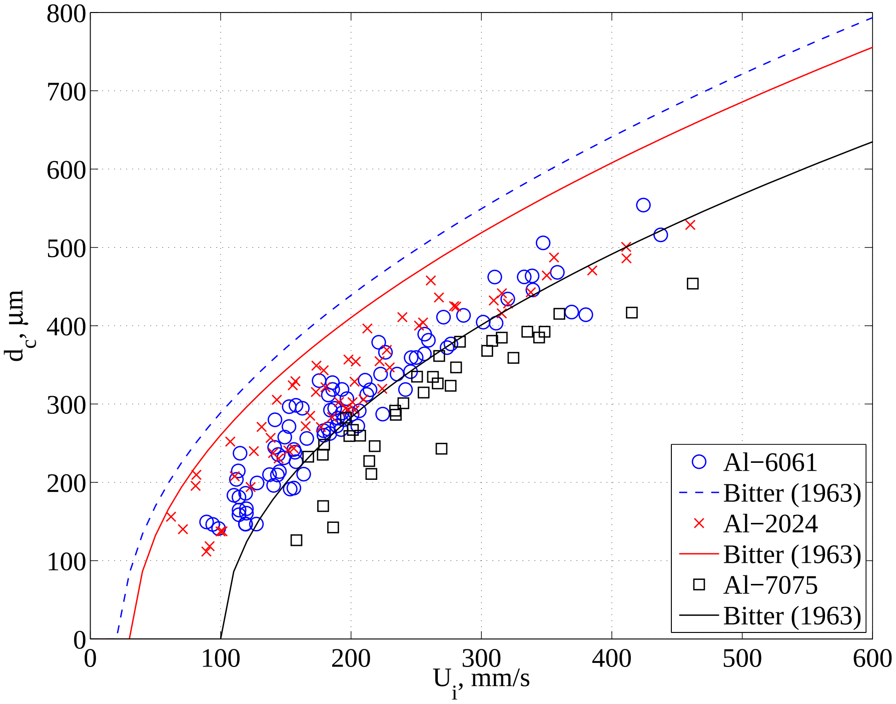

Figure 5.8: Crater diameter, d_c, as a function of the impact velocity, U_i

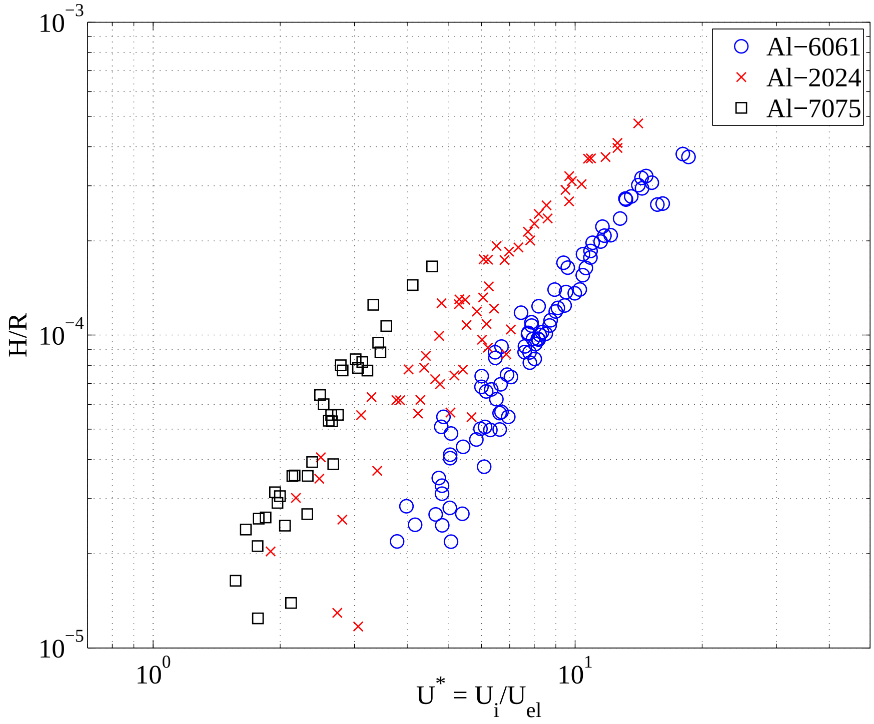

Figure 5.9: Indentation depth nondimensionalized by the particle radius as a function of U^*

Chapter 6

Energy of deformation

This section presents a the general chart that spans the elastic and elastic-plastic deformation regimes for fully immersed collisions. In addition to the energy of deformation, the hydrodynamic effects contribute significantly to the total energy losses during a collision. Extending the findings done by Eirich and Tabor (1948) and H.M.Clark and Burmeister (1992), it is shown that the fluid pressure during a collision can increase significantly.

6.1 Deformation parameter

The Hertz theory of the elastic impact is valid only during the elastic deformation regime. The boundary between elastic and elastic-plastic regimes can be determined by the *deformation parameter*, D. In general, this parameter compares the kinetic energy of the striker with the yield strength of the softer material (energy of deformation). Thus, D is defined as

$$D = \frac{\rho_p U_i^2}{Y}. \tag{6.1}$$

The experiments presented in this thesis used rigid particles as strikers and soft targets. Yield is expected to occur on the soft samples. The corresponding yield strength of the three different aluminum alloys was used to determine their elastic limit. Table 6.1 shows the elastic limits in terms of the deformation parameter, estimated using U_{el}. As discussed before, the elastic velocity(U_{el}) is used as a reference for the elastic limit for collisions.

Table 6.1: Elastic limit of the materials in terms of the deformation parameter, D

Material	Alloy	Elastic velocity, U_{el} (m s^{-1})	Deformation parameter, D$_{el}$
Aluminum	6061	0.024	1.58×10^{-8}
Aluminum	2024	0.033	2.56×10^{-8}
Aluminum	7075	0.101	1.58×10^{-7}

6.1.1 Residual volume

The residual volume, V_r, is defined as the volume of the indentation left on the soft material after the impact. This volume is approximated to a "spherical" cap, $V_r = 1/6\pi\, H(3(d_c/2)^2 + H^2)$. In this section, the residual volume is used to represent the magnitude of the indentation. Figure 6.1 shows the residual volume nondimensionalized by the volume of the particle, V_p, as a function of the nondimensional strain, $d_c E^*/d_p Y$, for the different aluminum alloys used in this thesis.

For nondimensional strains below 2.6, the residual volume is zero. For those strain values, the deformations remain elastic.

6.2 Fluid pressure

For immersed particle-wall collisions where the hydrodynamic effects cannot be neglected, the collision process results in a significant increase of the pressure in the liquid between the particle and the wall. As mention in Section 1.1, this increasing pressure may slow down the particle as it approaches the wall. Besides slowing down the particle, the pressure might also elastically deform either the particle or the wall. As shown in Figure 1.5, the minimum distance of approach with significant deformation, δ_m, is a function of the Stokes number. The solution given in Section 1.5.2 is limited in applicability since the minimum approach distance is constant, which is valid for a small range of Stokes numbers.

The following analysis is the result of the combination of the approaches done by Eirich and Tabor (1948) and H.M.Clark and Burmeister (1992). For simplicity, they started with a cylinder of finite length approaching a plane. The pressure in the liquid was calculated

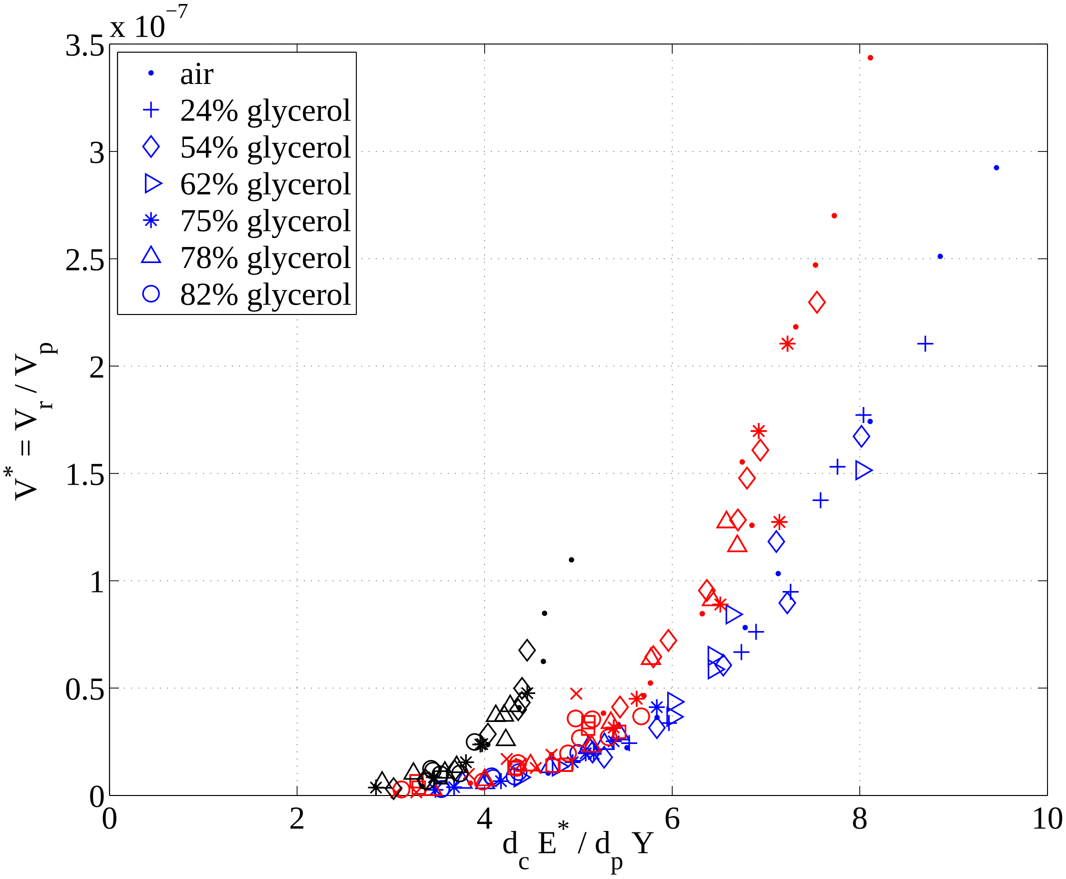

Figure 6.1: Nondimensional residual volume, $V^* = V_r/V_p$, as a function of the nondimensional strain d_cE^*/d_pY (Johnson (1985)). The colors represent: blue — alloy 6061, red — alloy 2024, and black — alloy 7075.

as a function of the impact velocity of a simplified particle. As the cylinder approaches the wall with a velocity U, the pressure of the interstitial fluid increases to its maximum value, p_{max}, corresponding to the critical thickness of the viscous fluid layer, δ_{i0}. Eirich and Tabor (1948) found a relation for the pressure as a function of the approaching velocity. The maximum value for that expression is given by

$$p_{max} = 0.934 \left(\frac{\rho_p^3 U_{i0}^5 d_p}{\mu} \right)^{1/2}, \tag{6.2}$$

with the corresponding film thickness

$$\delta_{i0} = \left(\frac{15}{32} \frac{\mu d_p}{\rho_p U_{i0}} \right)^{1/2} = R \left(\frac{5}{24} \right)^{1/2} \left(\frac{1}{St} \right)^{1/2}. \tag{6.3}$$

The film thickness where the pressure is maximum for a given fluid changes as a function of the critical impact velocity, U_{i0}. In the right panel of Figure 6.2 the maximum pressure is plotted as a function of the Stokes number, St_{i0}, based on the U_{i0}; the symbols represent different viscosity values. On the left panel, the film thickness, δ_{i0}, at which the pressure is maximum is plotted. To compare Figure 6.2 with previous studies, δ_{io} was nondimenzionalized by the particle radius, R, shown in Figure 6.3. The expression for the film thickness given by Equation 6.3 can be written as a function of St and it decays as $\sim (St_{io})^{-1/2}$.

Compared to the work done by Davis et al. (1986), which used a fixed value to approximate the critical distance, $\delta_{i0} \approx 0.01R$ is only valid for small Stokes numbers. Based on the previous work done by Eirich and Tabor (1948), Figure 6.3 (left panel) shows that for large Stokes numbers, $\delta_{io}/R < 0.01$. However, for $St_{io} < 20$ the assumption by Davis et al. remains consistent, i.e., $\delta_{io}/R \approx 0.01$. The pressure at the lowest point of the particle should match the maximum pressure of the squeezed liquid. As shown in Figure 6.3 (right), the maximum pressure in the squeezed liquid can be large enough to cause plastic deformations on either the particle or the wall. For any given impact velocity, U_{io}, the lower the viscosity, the larger the pressure in the squeezed film. The detail on Figure 6.3 (right) shows surfaces of constant velocity (dashed lines) ranging from 0.05–1.00 m/s, increasing from the bottom to the top.

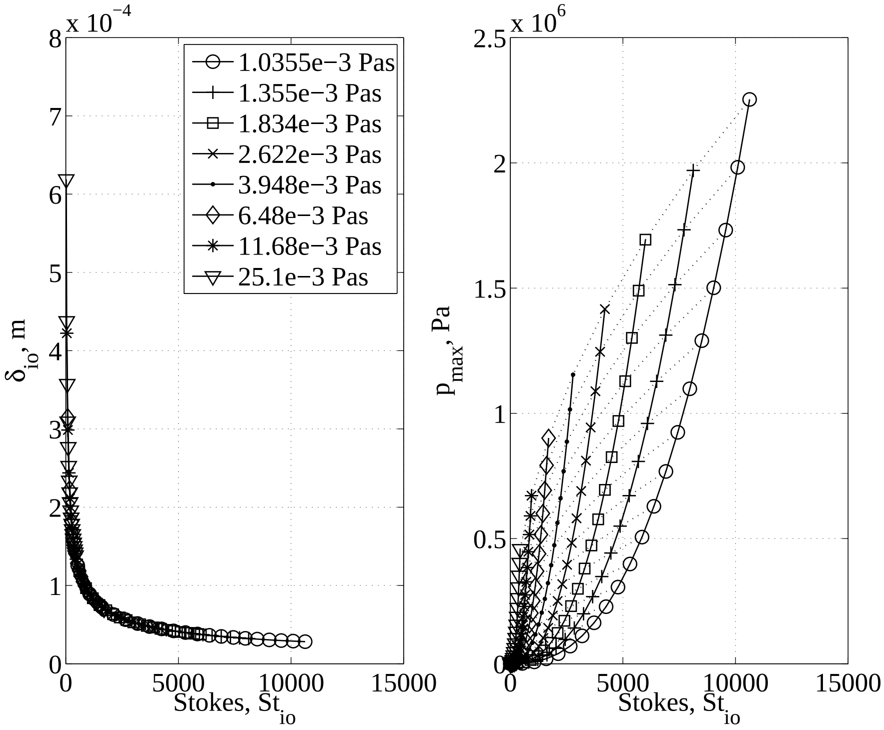

Figure 6.2: Simplified model proposed by Eirich and Tabor (1948) of a collision through liquid films. The particle approaching the wall corresponds to a stainless-steel solid sphere with a diameter, $d_p = 12.7$ mm, and a density $\rho_p = 7800\ kg\ m^{-3}$. The left panel represents the fluid film thickness, δ_{i0}, at which the pressure in the squeezed film is maximum, p_{max}. The panel on the right-hand side shows the variations of p_{max} as a function of St_{io}; the different symbols correspond to different values of viscosity.

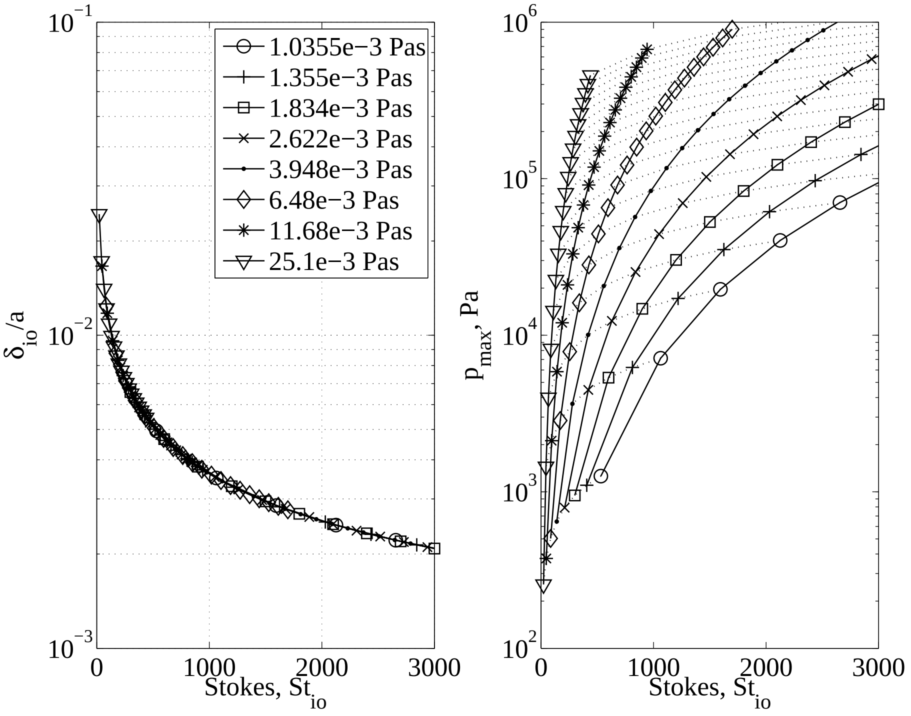

Figure 6.3: Nondimensionalized fluid film thickness, δ_{i0}, by the particle radius, R, (left panel) at which the pressure in the squeezed film is maximum, p_{max}. For a wide range of Stokes numbers (within the experimental range), the curve does not suggest a constant value for δ_{io}/R. The panel on the right-hand side shows a detail of the maximum pressure. The dashed lines represent constant velocity surfaces decreasing from top to bottom.

6.3 Comparison between surface deformation and coefficient of restitution

As the energy of the collision is consumed on plastic deformation, the coefficient of restitution decreases. Figure 6.4 shows the coefficient of restitution as a function of the Stokes number. The size of the symbols is proportional to the residual volume of the indentation. The larger indentations occur, as expected, for the aluminum alloys with lower yield strength. For the aluminum alloy with the highest value on yield strength, Al — 7075, the coefficients of restitution are the highest, and the magnitude of the indentations are significantly smaller.

The results in Figure 6.4 suggest that the magnitude of the indentation does not depend uniquely on the Stokes number. At a fixed Stokes number, the magnitude of the indentation (for a given material) is considerably larger for the glycerol-water mixtures with higher viscosity. This result is consistent with the analysis of the fluid pressure (see Figures 6.2 and 6.3). The combination of material properties and the surrounding liquid determine the maximum value for the coefficient of restitution. The same value on the magnitude of the indentation corresponds to various values on the coefficient of restitution. Collisions mixing hydrodynamic effects and surface deformations are not described by the parameters typically used for immersed elastic collisions.

For elastic collisions, the coefficient of restitution monotonically increases with the Stokes number. Figure 6.5 shows the coefficient of restitution as a function of the Stokes numbers for several combination of materials and liquids. Note that the coefficient of restitution approaches one ($e \approx 1$) as the Stokes number increases. For those experiments (Joseph et al. (2001)), neither the particles nor the surfaces suffered plastic deformation. Compared with Figure 6.4, when the surfaces undergo plastic deformations, the coefficient of restitution does not reach the elastic limit, i.e., $e = 1$. Within this interval of Stokes numbers, the values on the coefficient of restitution deviate from the experimental trend obtained by Joseph et al. (2001).

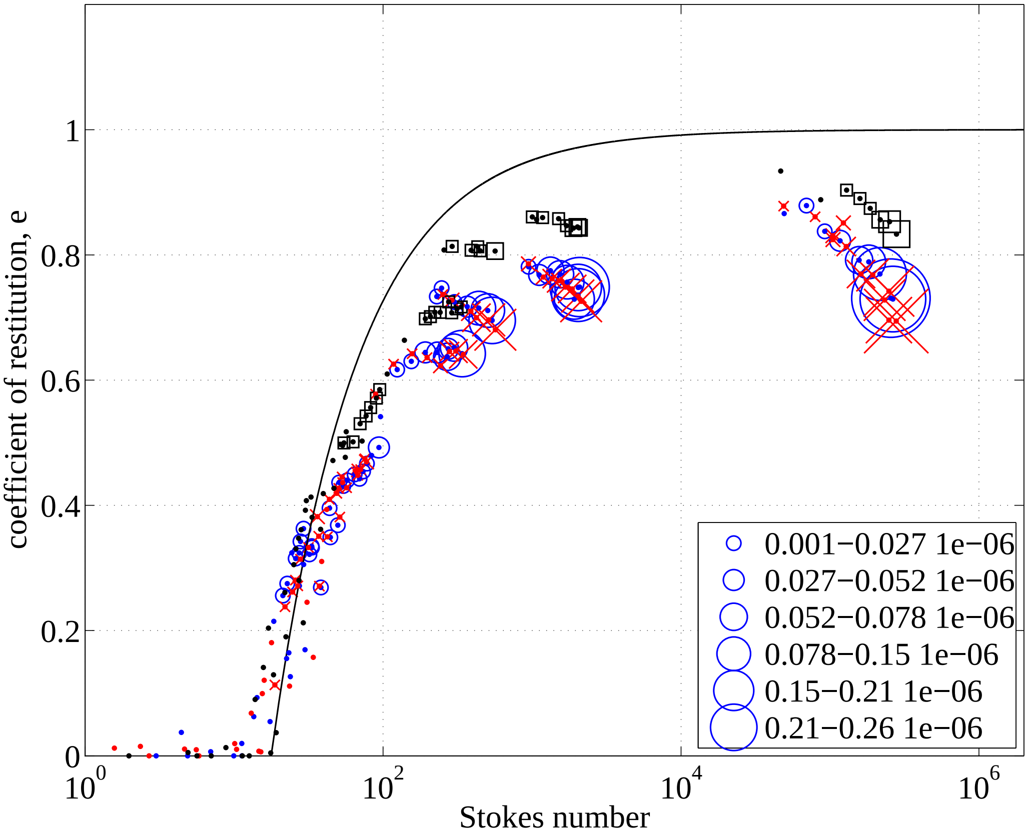

Figure 6.4: Coefficient of restitution as a function of the Stokes number. The size of the symbols is proportional to the residual volume of the permanent indentation relative to the volume of the impacting particle. The colors represent the different aluminum alloys: blue — alloy 6061, red — alloy 2024 and black — alloy 7075.

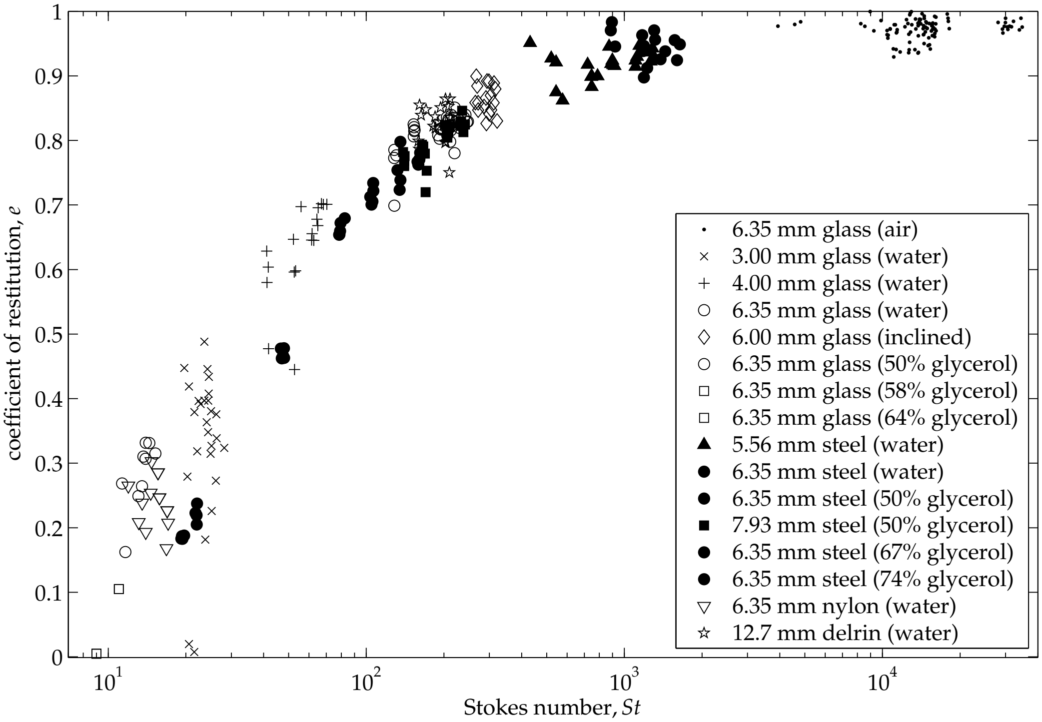

Figure 6.5: Coefficient of restitution as a function of the Stokes number. The experiments were done using several single particles impacting on a Zerodur block in different liquids (Joseph et al. (2001)).

6.4 General map for immersed collisions

The experiments presented in this thesis spanned two of the important deformation regimes, the elastic and the elastic-plastic regimes. In addition to those regimes typically studied in the absence of significant viscous forces, the experiments also covered the regimes where the hydrodynamic effects become important.

Figure 6.6 shows the nondimensionalized deformation parameter, $D^* = D/D_{el}$, as a function of the Stokes number. The size of the symbols represent the magnitude of the indentation based on the residual volume.The different values for the elastic limit in the deformation parameter, D_el, are shown in Table 6.1. This figure spans the following four regimes: elastic without rebound, elastic with rebound, elastic-plastic without rebound, and elastic-plastic with rebound.

The deformation regimes are determined by D^*. For $D* < 1$, the collisions remain in the elastic regime. For $D^* > 1$, the deformation is elastic-plastic. The collisions present small plastic deformations, which are comparable in magnitude with the elastic deformations. The critical Stokes number, St_c, is used as the boundary for the hydrodynamic effects. For $St < St_c$, no rebound occurs after the collision; correspondingly, for $St > St_c$ the particle rebounds after the collision. The results clearly show that for a fix Stokes number, the crater size increases as D^* increases. Similarly, for a given D^*, above the elastic limit, the crater size increases as the Stokes number increases.

Figure 6.7 shows the nondimensionalized deformation parameter, $D^* = D/D_{el}$, as a function of the Stokes number. The size and color of the symbols represent intervals of the coefficient of restitution. The sequence of dots showed at $D^* = 1$ represents the elastic limit, the region below that line correspond to the region of maximum coefficient of restitution. When the Stokes number is low enough, so that some lubrication effects are still important, for a given Stokes number, as D^* increases, the coefficient of restitution increases until it reaches a maximum and then it gradually drops back due to plastic deformation. For relatively high stokes numbers, the coefficient of restitution is already a maximum at $D^* = 1$, therefore, it begins to drop as we increased D^*. From this diagram, it is clear that the coefficient of restitution depends on both the fluid properties and the material properties.

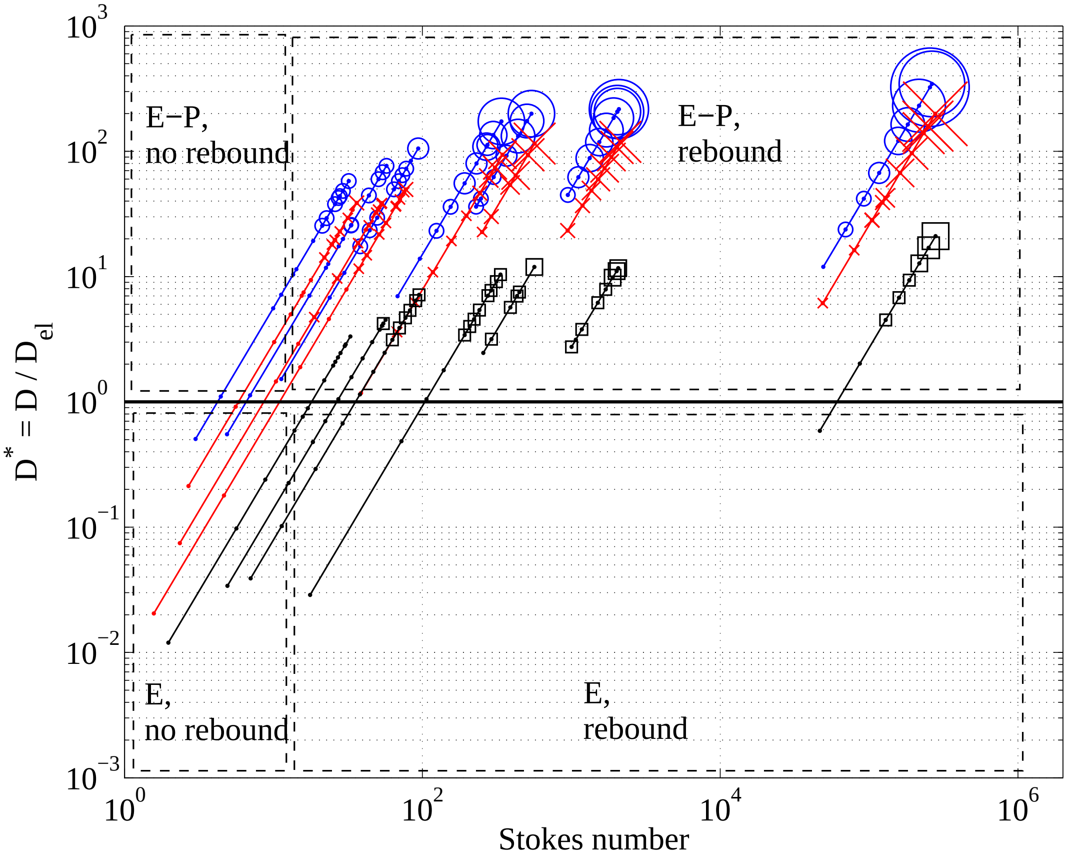

Figure 6.6: Deformation parameter, D, nondimensionalized by, D_{el}, as a function of the Stokes number. The size of the symbols is proportional to the residual volume of the permanent indentation relative to the volume of the impacting particle. The colors represent the different aluminum alloys: blue — alloy 6061, red — alloy 2024 and black — alloy 7075.

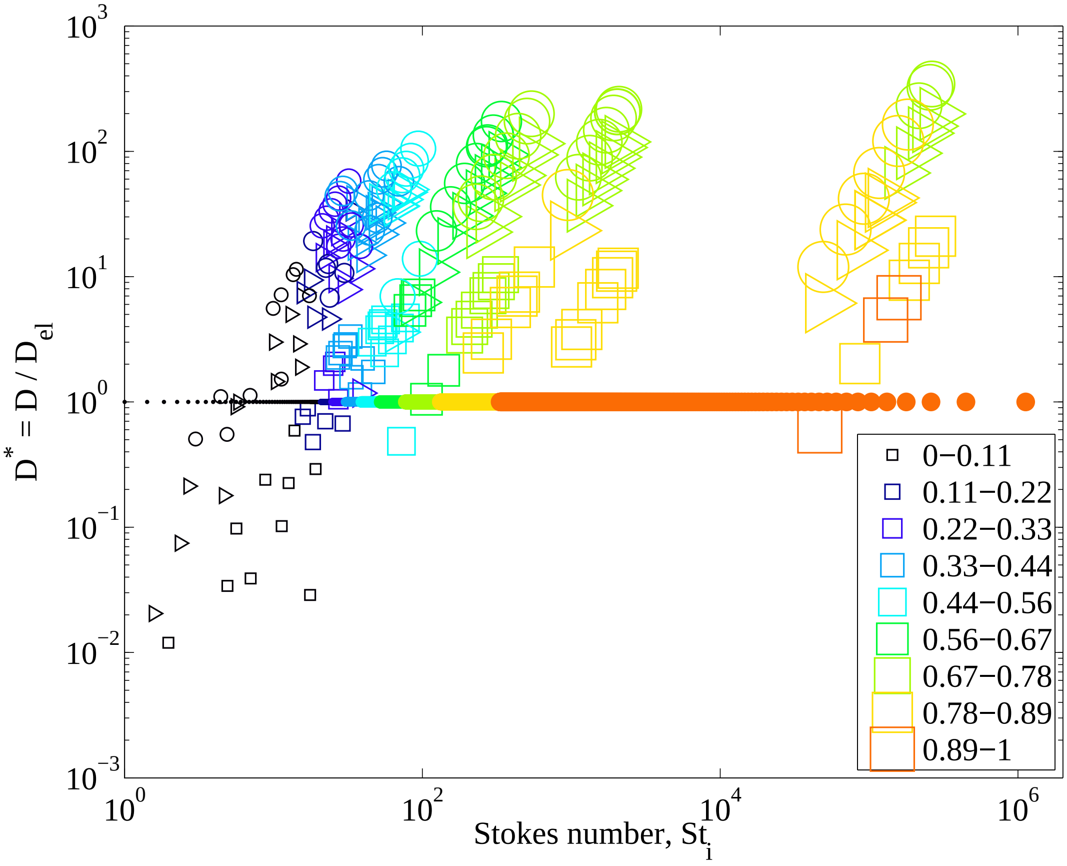

Figure 6.7: Deformation parameter, D, nondimensionalized by, D_{el}, as a function of the Stokes number. The size and color of the symbols are proportional to the coefficient of restitution. The three different aluminum alloys are: $\circ$ $Al-6061$, $\triangleright$ $Al-2024$, $\square$, $Al-7075$.

6.4.1 Elastic regime without rebound

This regime is limited by the $D^* < 1$ and $St < St_c$. In this regime most of the kinetic energy of the particle is dissipated by the viscous drag. For some experiments, the hydrodynamic forces were large enough to fully stop the particle before the collision. For most of those slow collisions, the strain in the samples resulting from the impact was not enough to produce plastic deformations. The stored elastic energy on the materials did not overcome the hydrodynamic load.

6.4.2 Elastic regime with rebound

This regime, limited only by the deformation parameter, $D^* < 1$, shows the dependency of the coefficient of restitution with the Stokes number. The experimental results previously done by Joseph et al. show that beyond the critical Stokes number, St_c, as the inertia of the particle increases overcoming the hydrodynamic effects, the coefficient of restitution monotonically increases. The summary of those experiments is shown in Figure 6.4. The elastic properties of the particles and the targets did not exceed the elastic limit, showing no effect on the measured coefficients of restitution. In this thesis, as shown in Figure 6.6, only the hardest material $Al — 7075$, contributed with a few points in this regime. None of those points presented permanent plastic deformations. This particular alloy remained closer to the elastic coefficient of restitution.

6.4.3 Elastic-plastic regime without rebound

For collisions below the “no rebound” condition given by the critical Stokes number, combinations with relatively soft materials take place in this regime. As shown in Figure 6.3 the pressure in the liquid between a solid body approaching a wall increases as the velocity and viscosity increases. The value of those pressures can be large enough to produce plastic deformation in the softer material. As discussed before in this thesis, the plastic deformation begins below the surface of the materials. Thus, in Figure 6.6, the few experimental points in this regime did not show any noticeable permanent deformation.

6.4.4 Elastic-plastic regime with rebound

As the particle velocity is increased for relatively low yield strength materials, the elastic limit is reached ($D^* > 1$). This regime combines collisions above the elastic limit and also beyond the critical Stokes number, St_c. The majority of the experiments presented in this thesis span this regime.

For low Stokes numbers ($St \sim 100$) the hydrodynamic effects are not negligible, but neither are the the plastic deformations. The energy losses are split in two: viscous dissipation and plastic deformation. As shown in Figure 6.4, those two energy-loss mechanisms balance each other at the maximum value of the coefficient of restitution. Beyond this equilibrium regime, the energy losses on plastic deformation become dominant, resulting in a decrease of the coefficient of restitution dampened only by the small hydrodynamic effects. As shown in Figure 6.6, the severity of the deformation, in terms of magnitude, increases with Stokes number, showing the balance between the two energy-loss mechanisms. For large Stokes numbers, $St > 1000$, the magnitude of the deformations remained unchanged, suggesting that viscous losses are negligible. Hence, the energy-loss mechanisms are dominated by the plastic deformations. The energy losses, as a bulk, are best appreciated by looking at the coefficient of restitution in Figure 6.4, where the elastic-plastic regime is represented by the points deviating from the solid line ($-$) representing the trend for the elastic collisions. In this figure, with the increasing on the coefficient of restitution with the Stokes number, increases, the coefficient of restitution

6.5 Discussion

This section proposed a general map in which collisions can be divided in four regimes according to the energy-loss mechanism. The combination of materials selected in this experimental work, and the low impact velocities limited the coverage of the map to only viscous losses and elastic-plastic deformations. Plastic deformations required either larger particle impact velocities or softer targets. To asses that the collisions remained within the elastic-plastic regime, the nondimensionalized strain was compared with typical quasi-static experiments of spherical indenters (Pane and Blank (2006)).The general map can be best explained by simultaneously looking at both the coefficient of restitution and the deformation parameter (Figures 6.6 and 6.4).

The proposed regimes suggested that during the collision process, the pressure in the liquid between the particle and the sample might be large enough to cause plastic deformation in the materials that are in contact, even if the particle does not rebound after the collision. For bouncing particles at low Stokes numbers, the two energy-loss mechanisms are significant for a short range of Stokes numbers, beyond which the plastic deformation become more dominant. Finally, the hydrodynamic effects are neglected for large Stokes numbers, where the only energy loss mechanism is the plastic deformation.

Chapter 7

Conclusion

7.1 Summary of results

This thesis presents the experimental results describing the hydrodynamic influence on the surface deformation resulting from immersed rigid particles impinging on soft walls. The experiments presented consist of controlled normal single particle-wall collisions. A single particle attached to a thin string was moved in a pendular trajectory towards various soft samples attached to a long bar. The experiments were conducted in air, and in various aqueous glycerol-water mixtures. The indentation parameters were measured for the samples presenting permanent deformations.

The instantaneous coefficient of restitution, e, was used to quantify the overall energy loss. In the elastic regime, the coefficient of restitution is well characterized by the Stokes number. The critical Stokes number, below which no rebound occurs ($e = 0$), was found to be $St_c \approx 10$ for the aluminum alloys Al — 6061 and Al — 2024, and for the alloy Al — 7075 the critical value was $St_c \approx 15$.

The combination of materials and impact velocities selected for this work spanned the elastic and elastic-plastic deformation regimes. The impact velocities needed to cause yield in metal surfaces are very small; therefore, for most of the impacts between metallic bodies some degree of plasticity may be present. Within the elastic-plastic regime, there is an extra critical Stokes number based on the elastic velocity, U_{el}, below which the collisions remain elastic. This elastic Stokes number, St_{el}, is not unique and increases as the viscosity decreases. For some combination of fluids and materials, the elastic limit was reached even for collisions that showed no rebound.

Based on those two critical Stokes numbers, St_c and St_{el}, the general collision chart presented in this thesis spans the following four regimes:

Within this last regime, the hydrodynamic effects are dominant at low Stokes numbers. As the inertia of the particle increases, the permanent indentations become larger. Simultaneously, the coefficient of restitution also increases. During the elastic recovery, the kinetic energy of rebound overcomes the viscous forces. Consequently, the coefficient of restitution increases until it reaches a maximum value. The experimental results suggested that this maximum value is a combination of the elastic properties of the materials and the viscosity of the surrounding liquid. The energy devoted to plastic deformation becomes significant when the maximum value in the coefficient of restitution is reached. The two energy-loss mechanisms seemed to reach partial equilibrium. During this interval of partial equilibrium, as the Stokes number increases, the hydrodynamic effects become less dominant; however, since the size of the indentation increases, the apparent excess of energy on the total budget is consumed as plastic deformation, keeping the coefficient of restitution constant during this interval. If the collisions were perfectly elastic, the coefficient of restitution would monotonically increase with the Stokes number.

Eventually, the energy of deformation becomes more dominant and the hydrodynamic effects negligible. Hence, the coefficient of restitution gradually falls with increasing Stokes numbers. The experimental results suggested that the decaying rate of the coefficient of restitution is damped by the hydrodynamic effects.

The experiments conducted in air showed a decrease in the coefficient of restitution as the impact velocity increased. The results were compared with three different models for elastic-plastic regimes. This particular deformation regime is not precisely defined, resulting in a poor agreement with the models. The models are based on dynamic properties that change with the severity of the impact, from the elastic limit to the fully plastic limit.

The asymptotic decay on the coefficient of restitution of $e \sim V^{-1/4}$ is valid only for fully plastic deformations, i.e., impact velocities a lot larger than the elastic velocity. The fully plastic regime was not covered by any of the experimental results presented in this work.

In order to observe small variations in the indentations formed by dry and wet collisions in the border line of the elastic-plastic regime, the surface of the samples were mirror polished. The deformation parameters were carefully measured. However, the experimental results showed that the magnitude of the indentation parameters is independent of the viscosity of the surrounding liquid within the elastic-plastic regime. Within the experimental error, the size of the indentations for collisions in air were on the order of magnitude of the immersed collisions. Existing theories on the wear of plastic surfaces were compared with the measured deformation. The predicted crater diameter formed by the particle impacts compared relatively well with the experimental results. For the three different aluminum alloys, the estimated value overestimated the experimental values.

The crater dimensions and therefore the energy absorbed by plastic deformation is clearly independent of the liquid or gas medium and only a function of the incident velocity and the material properties. This must mean that viscous effects in the thin contact or near-contact film of fluid are negligible. In other words that the high speed flow in that film is dominated by inertial effects and that vicous stresses are negligible; the fluid pressure in the film did not reach a value sufficient to contribute to creating a crater. If it were not for the craters in air we could say that all the other fluids have similar densities and therefore the film flows and pressures are the same for a given incident velocity. The viscous effects are only different on the rest of the surface of the sphere that is not in contact. So what makes the coefficient of restitution different is not the flow in the film but the flow over the rest of the sphere.

7.2 General comments and future directions

The hydrodynamic effects combined with the elastic-plastic deformation were studied. The limitations on the experimental setup used in this work confined the results within elastic and elastic-plastic regimes. The fully plastic regime remained unresolved. Extending the range of impact velocities and using softer materials as targets would be a good way to span the blank areas in the general collision chart.

Due to the limited range of impact velocities, it was not possible to observe the behavior of the particle-wall collision for a given combination of materials and a given liquid. It was mentioned that the coefficient of restitution increases with the Stokes number. When the energy devoted to plastic deformation becomes important, the coefficient of restitution reaches a maximum value, remaining constant within a range of Stokes numbers. For further increase on the Stokes number, the behavior of the coefficient of restitution is merely qualitative.

Also of interest is the problem where the particles are soft. In fluid-particle systems, the containers might be more rigid than the particles reversing the deformation problem presented in this thesis. Using a similar pendulum setup, soft particles impacting hard surfaces at various velocities might show a similar behavior on the energy loss mechanisms as the severity of the deformations increases. Those experiments might as well be extended for binary collisions.

In order to complement the understanding in the field of erosion in fluid-particulate systems, the study of permanent deformations due to oblique collisions would be necessary. Cutting is the type of wear produced by oblique collisions, in which material from the surface is actually removed by the striker. Previously, for elastic collisions it has been shown that oblique collision can be decoupled into tangential components and normal components. Studying oblique collisions allowing the surfaces to deform, and comparing those results with the normal collisions experiments conducted in this thesis, might show whether cutting wear decouples into tangential shearing and normal indentations.

During the stage of deciding the final experimental setup, a few collisions were done using free-fall techniques, resulting in large impact velocities. Looking at one of the permanent indentations formed during those experiments, evidence of cavitation marks was observed inside the indentation. This observation adds an extra erosion mechanism on the immersed collisions. For a full understanding of the erosion process this additional mechanism deserves some attention.

Bibliography

G. Barnocky and R.H. Davis. Elastohydrodynamic collision and rebound of spheres: Experimental verification. *Physics of Fluids*, 31, 1988.

J.G.A. Bitter. A study of erosion phenomena. *Wear*, 6:5–21, 169–190, 1963.

F.P. Bowden and D. Tabor. *The Friction and Lubrication of Solids*. Oxford University Press, 1986.

H.M. Clark. On the impact rate and impact energy of particles in a slurry pot erosion tester. *Wear*, 147(1):165–183, 1991.

H.M. Clark. A comparison of the particle impact in gas-solid and liquid-solid erosion. *Wear*, 186(2):465–472, 1995.

C.T. Crowe, M. Sommerfield, and Y Tsuji. *Multiphase Flows with Droplets and Particles*. CRC Press, New York, 1998.

R.H. Davis, J.M. Serayssol, and E.J. Hinch. The elastohydrodynamic collision of spheres. *Journal of Fluid Mechanics*, 163:479–497, 1986.

I. Eames and S.B. Dalziel. Dust resuspension by the flow around an impacting sphere. *Journal of Fluid Mechanics*, 403:305–328, 2000.

J.K. Edwards, B.S. McLaury, and S.A. Shirazi. Modeling solid particle erosion in elbows and plugged tees. *Journal of Energy Resources Technology*, 123:227–284, 2001.

F.R. Eirich and D. Tabor. Collisions through liquid films. *Cambridge Philosophical Society*, 44:566–580, 1948.

I. Finnie. Erosion of surfaces by solid particles. *Wear*, 3:87–103, 1960.

B.A. Gama, S.L. Lopatnikov, and Jr J.W. Gillespie. Hopkinson bar experimental technique: A critical review. *Applied Mechanics Reviews*, 57(4):223–250, 2004.

W. Goldsmith. *Impact*. Arnold, London, 1960.

P. Gondret, M. Lance, and L. Petit. Bouncing motion of spherical particles in fluids. *Physics of Fluids*, 142(3):643–652, 2002.

B. Griffiths. *Manufacturing Surface Technology*. Butterworth-Heinemann, 2001.

H.M.Clark and L.C. Burmeister. The influence of the squeeze film on particle impact velocites in erosion. *Journal of Impact Engineering*, 12(3):415–426, 1992.

B. Hu and P. Eberhard. Simulation of longitudinal impact waves using time delayed systems. *Journal of Dynamic Systems, Measurement, and Control*, 126:644–649, 2004.

I.M. Hutchings. Energy absorbed by elastic waves during plastic impact. *Journal of Physics D: Applied Physics*, 12(1819-1824), 1979.

I.M. Hutchings. A model for the erosion of metals by spherical particles at normal incidence. *Wear*, 70:269–281, 1981.

R.M. Iverson. The physics of debris flows. *Reviews of Geophysics*, 35(3):245–296, 1997.

K.K. Johnson. *Contact Mechanics*. Cambridge University Press, 1985.

G. Joseph. *Collisional dynamics of macroscopic particles in a viscous fluid*. PhD thesis, California Institute of Technology, 2003.

G. Joseph, R. Zenit, M.L. Hunt, and A.M. Rosenwinkel. Particle-wall collisions in a viscous fluid. *Journal of Fluid Mechanics*, 433:329–346, 2001.

J.R. Kadambi, P. Charoenngam, A. Subramanian, M.P. Wernet, J.M. Sankovic, G. Addie, and R. Courtwright. Investigations of particle velocities in a slurry pump using piv: Part 1, the tongue and adjacent channel flow. *Journal of Energy Resources Technology*, 126: 271–278, 2004.

A.H. Kharaz and D.A. Gorham. A study of the restitution coefficient in elastic-plastic impact. *Philosophical Magazine Letters*, 80:549–559, 2000.

G. Lian, M.J. Adams, and C. Thornton. Elastohydrodynamic collision of solid spheres. *Journal of Fluid Mechanics*, 311:141–152, 1995.

D.R. Lide. *Handbook of Chemistry and Physics.* CRC Press, Boca Raton, Florida, 2001.

J. Lu, S. Suresh, and G. Ravichandran. Dynamic indentation for determining the strain rate sensitivity of metals. *Journal of Mechanics and Physics of Solids*, 51:1923–1938, 2003.

M.H. McLaughlin. *An experimental study of particle-wall collisions relating to flow solid particles in a fluid.* PhD thesis, California Institute of Technology, 1968.

Ivindra Pane and Eberhard Blank. Role of plasticity on indentation behavior: Relations between surface and subsruface response. *International Journal of Solids and Structures*, 43:2014–2036, 2006.

C.V. Raman. On some applications of hertz's theory of impact. *American Physical Society*, 15(4):277–284, 1920.

J. Reed. Energy losses due to elastic wave propagation during an elastic impact. *Journal of Physics D: Applied Physics*, 18:2329–2337, 1985.

A.W. Ruff and R.G. Bayer. *Tribology: Wear Test Selection for Design and Application.* ASTM International, 1993.

C. Shook and M. Rocco. *Slurry flow: Principles and Practice.* Butterworth-Heinemann, Boston. Chapter 8: Wear in Slurry Equipment, 1991.

R. Sondergaard, K. Chaney, and C.E. Brennen. Measurements of solid spheres bouncing off flat plates. *Journal of Applied Mechanincs*, 112(3):694–699, 1990.

D. Tabor. *The hardness of metals.* Oxford University Press, 1951.

T.R. Thomas. *Rough Surfaces.* Imperial College Press, 1982.

C. Thornton. Coefficient of restitution for collinear collisions of elastic perfectly plastic spheres. *Journal of Applied Mechanincs*, 64:383–386, 1997.

F.L. Yang. *Interaction Law for a Collision Between Two Solid Particles in a Viscous Liquid.* PhD thesis, California Institute of Technology, 2006.

J. Yang and K. Komvopoulos. Impact of a rigid sphere on an elastic homogeneous half-space. *Journal of Tribology*, 127:325–330, 2005.

C. Zener. The intrinsic inelasticity of large plates. *Physical Review*, 59:669–673, 1941.

R. Zenit. *Collisional Mechanics in Solid-Liquid Flows.* PhD thesis, California Institute of Technology, 1997.

R. Zenit and M.L. Hunt. The impulsive motion of a liquid resulting from a particle collision. *Journal of Fluid Mechanics*, 375:345–361, 1998.

R. Zenit and M.L. Hunt. Mechanics of immersed particle collisions. *Journal of Fluid Mechanics*, 121(1):179–184, 1999.

R. Zenit, M.L. Hunt, and C.E. Brennen. Collisional particle pressure measurements in solid-liquid flows. *Journal of Fluid Mechanics*, 353:261–283, 1997.

Y. Zhong and K. Minemura. Measurement of erosion due to particle impingement and numerical prediction of wear in pump casing. *Wear*, 199:36–44, 1996.